

Radical-source molecular beam epitaxy of ZnO-based heterostructures

D I S S E R T A T I O N

zur Erlangung des akademischen Grades

doctor rerum naturalium (Dr. rer. nat.)
im Fach Physik

eingereicht an der
Mathematisch-Naturwissenschaftlichen Fakultät I
Humboldt-Universität zu Berlin

von
Herr Physikingenieur Sergey Sadofiev
31.03.1977, Rjasan, UdSSR

Präsident der Humboldt-Universität zu Berlin:
Prof. Dr. Christoph Marksches

Dekan der Mathematisch-Naturwissenschaftlichen Fakultät I:
Prof. Dr. Lutz-Helmut Schön

Gutachter:

1. Prof. Dr. Fritz Henneberger
2. Prof. Dr. W. Ted Masselink
3. Prof. Dr. Andreas Waag

eingereicht am: 15.06.2009

Tag der mündlichen Prüfung: 27.10.2009

Abstract

This work focuses on the development of the novel growth approaches for the fabrication of Group II-oxide materials in the form of epitaxial films and heterostructures. It is shown that molecular-beam epitaxial growth far from thermal equilibrium allows one to overcome the standard solubility limit and to alloy ZnO with MgO or CdO in strict wurtzite phase up to mole fractions of several 10 %. In this way, a band-gap range from 2.2 to 4.4 eV can be covered. A clear layer-by-layer growth mode controlled by oscillations in reflection high-energy electron diffraction makes it possible to fabricate atomically smooth heterointerfaces and well-defined quantum well structures exhibiting prominent band-gap related light emission in the whole composition range. On appropriately designed structures, laser action from the ultraviolet down to green wavelengths and up to room temperature is achieved. The properties and potential of the "state-of-the-art" materials are discussed in relation to the advantages for their applications in various optoelectronic devices.

Zusammenfassung

Im Rahmen der Dissertation wurden molekularstrahlepitaktische Verfahren zur Züchtung von Hetero- und Quantenstrukturen auf der Basis der Gruppe II-Oxide entwickelt. Insbesondere wurde ein Wachstumsregime weit entfernt vom thermischen Gleichgewicht etabliert, welches die Mischung von CdO und MgO mit ZnO in phasenreiner Wurtzitstruktur ermöglicht, wobei die Gleichgewichtslöslichkeitsgrenzen dramatisch überschritten werden. In den Mischkristallen kann die Bandlücke kontinuierlich von 2.2 bis 4.4 eV eingestellt werden. Das Wachstum verläuft in einem zweidimensionalen Modus und resultiert in atomar glatten Ober- und Grenzflächen. Ausgeprägte RHEED- Intensitätsoszillationen erlauben die atomlagengenaue Kontrolle der Schichtdicken und somit die Realisierung wohldefinierter Einzel- und Mehrfachquantengrabenstrukturen. Diese zeichnen sich durch eine hohe Photolumineszenzquantenausbeute im gesamten sichtbaren Spektralbereich aus. Laseraktivität kann vom UV bis zum grünen Wellenlängenbereich bei Raumtemperatur erzielt werden. Das Potenzial dieser Quantenstrukturen in Hinblick auf ihre Anwendung in opto-elektronischen Bauelementen wird diskutiert.

Inhaltsverzeichnis

1	Introduction	1
2	Literature Review	3
2.1	Introduction	3
2.2	ZnO: Basic properties and specific features	3
2.3	Fabrication of ZnO and ZnO-based hetero-structures	5
2.3.1	Different growth techniques	5
2.3.2	Typical approaches to radical-source MBE of ZnO	7
2.3.3	Substrates	8
2.3.4	ZnO-based alloys and their heterostructures	17
2.4	Conclusion	22
3	Experiment	25
3.1	DCA-450 MBE apparatus for Group II-oxide epitaxy	25
3.1.1	General	25
3.1.2	Deposition Chamber	25
3.2	Specific features of oxide MBE	27
3.3	Substrate preparation	28
3.4	Characterization tools	29
3.4.1	<i>In-situ</i> diagnostic	29
3.4.2	<i>Ex-situ</i> diagnostics	34
4	Growth of ZnMgO alloys and ZnO/ZnMgO quantum well structures	39
4.1	Introduction	39
4.2	ZnMgO ternary alloy films	39
4.2.1	Two-step growth procedure: ZnMgO nucleation layer	39
4.2.2	Influence of the growth temperature	41
4.2.3	ZnMgO alloys: Band gap and lattice constant vs. Mg content	41
4.2.4	Structural properties	42
4.3	ZnO/ZnMgO quantum well structures	45
4.4	ZnO/ZnMgO MQWs: Structural and optical properties	46
4.5	Conclusion	48
5	Growth of ZnCdO alloys and ZnCdO/ZnO heterostructures	53
5.1	Introduction	53
5.2	Radical-source MBE of ZnCdO alloys	53
5.2.1	Fabrication of ZnCdO alloys	53

Inhaltsverzeichnis

5.2.2	Structural properties	60
5.2.3	Optical properties	60
5.3	Quantum well structures	62
5.3.1	Growth	62
5.3.2	Postgrowth annealing: A way to increase the radiative efficiency	63
5.3.3	Polarization fields in ZnCdO/ZnO SQW structures	67
5.4	Visible wavelength lasing of ZnCdO/ZnO multiple quantum well structures	68
5.5	Conclusion	69
6	Growth of ZnO-based heterostructures on ZnO wafers	75
7	Outlook	81
8	Summary	85

1 Introduction

Zinc oxide (ZnO) is a well-known material that possesses applications in very diverse fields as described already in the 1957 monograph, *Zinc Oxide Rediscovered*, by H. E. Brown [Bro57]. Interestingly, ZnO has been "rediscovered-at least twice since then, in the late 1970s and late 1990s. However, the present rediscovery is the most dramatic one, and has generated journal publication rates of well over 1000/yr [Loo06]. One reason for the present resurgence is the recent availability of higher-quality bulk and epitaxial materials, which has enabled the development of ultraviolet (UV) light-emitting diodes (LEDs), transparent thin-film transistor, and nanodevices of many designs and functions. Along with the device development, the materials themselves have been studied by a wider variety of sophisticated techniques, and many of the fundamental properties are now more clearly understood. The renewed interest in ZnO has been mainly initiated by the demonstration of stimulated emission under optical pumping from thin epitaxial films grown by pulsed laser deposition (PLD) [ZTW⁺97, OKS⁺98b] and radical-source molecular beam epitaxy (MBE) [BCZ⁺97]. The rapid development of these growth techniques, as well as metal-organic chemical vapor deposition (MOCVD), made it possible to consider oxides as conventional compound semiconductors which could be reproducibly prepared in a growth reactor despite the highly unfriendly environment. Intensive research efforts performed in the years 1999 - 2001 have resulted in the fabrication of first metastable Zn(Cd,Mg)O alloys and Zn(Cd,Mg)O/ZnO heterostructures [OKK⁺98, MMJ⁺99, SNM⁺99, MSK⁺01], that strongly stimulated a worldwide interest in ZnO as a material for optoelectronic applications. On the other hand, this interest has immediately generated various fundamental and practical questions including, e.g., the solid solubility limits of the ternaries, possibility to grow high-quality hetero- and quantum well structures on available substrates with extremely large lattice mismatch, ability to overcome the doping asymmetry typical for all wide-gap materials, etc. All these issues remained largely unexplored and had to be investigated at levels of increasing scientific depth.

This thesis is an attempt to summarize my recent efforts in radical-source MBE of ZnO and ZnO-based heterostructures, especially ZnMgO and ZnCdO ternary alloy films, and to discuss their growth related optical and structural properties. Band gap engineering and fabrication of ZnO-based heterostructures is a novel, rapidly developing and highly competitive field of the worldwide research activity aiming at commercial realization of LEDs operating in the visible and UV spectral range and competing with GaN-based devices. In order to keep pace in this activity, one often has to walk with long strides, sometimes leaving behind some important and interesting details unresolved to be analyzed in the future. Unfortunately, such moments can be recognized in

1 Introduction

some places of this work. The author, however, is aware of the arising physical questions, but no intentional attempt is made to obligatory answer all of them. The thesis is organized as follows: First, a brief literature review is given in Chapter 2, which clearly distinguishes between the state-of-the-art in ZnO activity at the date when the present work was initiated (November, 2004), and results appearing later. The most important results from these later findings are discussed in the following Chapters. Chapter 3 contains a brief description of the MBE apparatus assembled and employed for the growth experiments, as well as various analytical tools used for characterization of the grown structures. Chapter 4 is dedicated to the fabrication of ZnMgO alloys and ZnO/ZnMgO single (SQW) and multiple (MQW) quantum well structures on *a*-plane sapphire substrates, where a specific procedure based on low-temperature (LT) growth ($T_g = 350\text{ }^{\circ}\text{C}$) and short time annealing steps ($T_a \simeq 560\text{ }^{\circ}\text{C}$) performed at each interface is introduced. The concept of the LT growth is fundamental in the current work. In the case of ZnMgO it allows for the incorporation of up to 40% of Mg in a ZnO host lattice without indication of a separation between wurtzite (ZnO) and rocksalt (MgO) phases and significant interface roughening. Incorporation of Mg enables one to widen the UV band gap of ZnO from 3.37 eV to 4.4 eV and ensures strong carrier confinement in the case of ZnO/ZnMgO QW structures. As a result, the fabricated single and multiple QWs show narrow emission lines, quantum size effects (QSE) and lasing under optical pumping. Chapter 5 is devoted to the growth and growth related properties of ZnCdO alloys, where a novel strategy based on the extremely low deposition temperature ($T_g \simeq 150\text{ }^{\circ}\text{C}$) and oxygen-rich conditions is presented. The growth scheme¹ makes it possible to reproducibly incorporate of at least up to 32% of Cd in the wurtzite ZnO lattice, and to shift the optical gap from 3.37 eV to 2.2 eV. Despite the very low temperature, a single crystalline layer-by-layer growth is accomplished. ZnCdO/ZnO QWs fabricated under optimized conditions demonstrate lasing under optical pumping reaching the green wavelength range also at room temperature (RT). Chapter 6 demonstrates that the growth recipes developed for ZnMgO and ZnCdO on sapphire can be naturally adapted to ZnO wafers. The resultant improvement of the crystal quality is striking and only limited by the perfection of the substrate. Chapter 7 describes results of the current experiments on nitrogen doping, identifies still open issues and obstacles and discusses possible ways to overcome them. Finally, the main results of this work are summarized in Chapter 8.

As any material research work, this thesis is a product of collaboration. The personal contribution of the author is the MBE growth including developing, testing and optimizing novel growth schemes and strategies. Necessary characterization of the grown structures by various *ex situ* analytical tools (high-resolution X-ray diffraction (HRXRD), energy-dispersive X-ray analysis (EDX), transmission electron microscopy (TEM), study of optical properties) is done in collaboration with different people. The results are included in the thesis as they demonstrate the value of the developed growth concepts.

¹Patent application: 10 2006 045 834.6 (22.09.06), PCT/DE 2007/001482 (17.08.07).

2 Literature Review

2.1 Introduction

The present Chapter summarizes necessary information about basic physical properties and specific features of ZnO, as well as gives an overview of the most important findings in the epitaxial growth of ZnO and ZnO-related materials.

2.2 ZnO: Basic properties and specific features

ZnO is a transparent oxide semiconductor with a wide band-gap of $E_g = 3.37$ eV. This material is currently attracting a lot of attention because of the high exciton binding energy (~ 60 meV), high radiation hardness, capability of bulk growth and wet chemical etching, as well as comparatively low material cost.

ZnO crystallizes in the hexagonal wurtzite-type structure shown in Fig. 2.1. It has a polar hexagonal axis (due to a lack of inversion symmetry), the c -axis, chosen to be parallel to z . The primitive translation vectors \mathbf{a} and \mathbf{b} lay in the x - y plane, are of equal length, and form an angle of 120° . The point group is, depending on notation, $6mm$ or C_{6v} , the space group $P6_3mc$. One zinc ion is surrounded tetrahedrally by four oxygen ions and vice versa. The primitive unit cell contains two formula units of ZnO. The lengths of the primitive translation vectors at room temperature are $a = b \approx 3.252$ Å and $c \approx 5.213$ Å. In contrast to other II-VI semiconductors, which exist both in the cubic zincblende and the hexagonal wurtzite-type structure ZnO crystallizes with great preference in the wurtzite-type structure. The cubic zincblende-type structure can be stabilized to some extent by epitaxial growth of ZnO on suitable cubic substrates, while the rocksalt structure is stable only under pressure [Kli07].

The most common growth direction of hexagonal ZnO is normal to the (0001) basal plane, where the atoms are arranged in bilayers consisting of two closely spaced hexagonal layers, one containing cations and the other anions, so that the bilayers have polar faces. The convention is that the [0001] axis points from the face of the O-plane to the Zn-plane, i.e. in the positive z direction. In other words, when the bonds along the c -direction are from cation to anion, the polarity is referred to as Zn polarity. By the same argument, when the bonds along the c -direction are from anion to cation, the polarity is referred to as O polarity [Fig. 2.2]. It is important to note that the (0001) and (000 $\bar{1}$) surfaces of ZnO are inequivalent and the crystal polarity has very marked effects both on growth kinetics and bulk properties of Group II-oxide materials. In what follows, only O-polar ZnO or ZnO-based ternary alloy films will be considered.

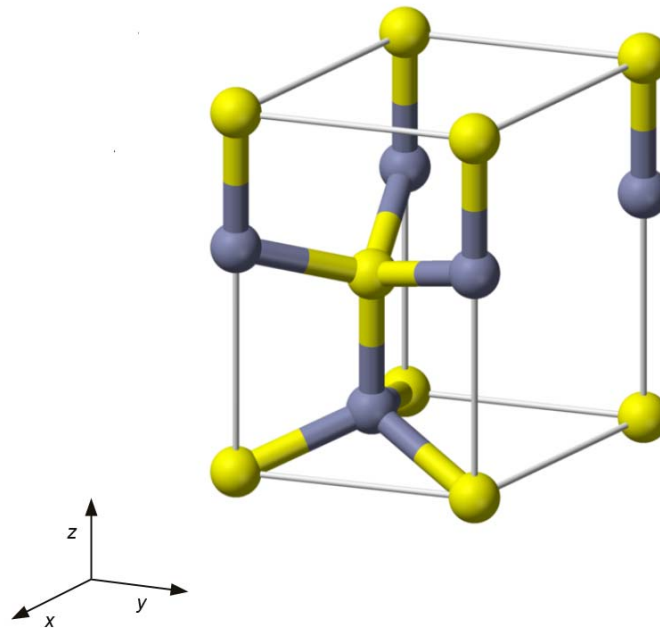


Abbildung 2.1: Unit cell of the crystal structure of ZnO. Light colour - O; dark colour - Zn. (From [Kli07]).

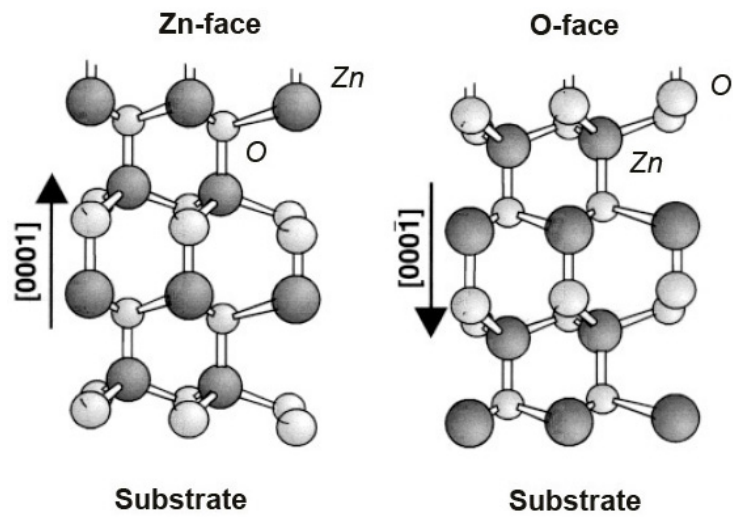


Abbildung 2.2: Different polarities of wurtzite ZnO. (Adapted from [Amb98]).

2.3 Fabrication of ZnO and ZnO-based hetero-structures

ZnO has the unique feature to grow with a strong (0001) preferential orientation on various kinds of substrates, as well as to form easily a large variety of specific nanostructures like nanorods, nanopillars, nanopropellers, etc. [Wan04]. Various growth techniques have been used to produce ZnO thin films and bulk crystals. The current review, however, focuses only on thin epitaxial films and only on preparation techniques allowing for a precise control over the deposition procedure, such as MOCVD, PLD and MBE.

2.3.1 Different growth techniques

MOCVD

MOCVD, also known as metalorganic vapor phase epitaxy (MOVPE), is a growth method especially suited for compound semiconductors that relies on the surface reaction of organic or metalorganic compounds and metal hydrides containing the required chemical elements. Formation of the epitaxial layer occurs by final pyrolysis of the constituent chemicals at the substrate surface, i.e. requires relatively high growth temperatures. In contrast to PLD or MBE processes, MOCVD growth is driven by chemical reactions (not physical deposition) and takes place in the gas phase at moderate pressures (2 to 100 kPa) under near-equilibrium conditions. This powerful and inexpensive technique has been developed mainly for the production of highly stoichiometric materials of virtually all III/V semiconductor compounds. It has also been successfully used for the growth of other semiconductor materials such as the II/VI compounds and alloys as well as for a number of complex oxides, including high-temperature (HT) semiconductors [Hur94]. The semiconductor materials produced by MOCVD are generally comparable in quality to the best produced by other techniques, with few deep-level defects and extremely high purity levels. In addition, the MOCVD process can be used to produce atomically abrupt interfaces between layers varying either in the solid composition or the doping level. This has resulted in the production of materials and designs for high-quality QWs, superlattices, and two-dimensional (2D) electron gas structures. The evident disadvantage of MOCVD compared to MBE or PLD is that mostly knowledge about the actual processes at the surface can be obtained only from indirect analysis of the results of the growth process.

Pulsed laser deposition

PLD is a deposition (specifically physical vapor deposition) technique where a high-power pulsed laser beam is focused inside a vacuum chamber to strike a sintered target of the desired composition. The material is then vaporized from the target and deposited as a thin film on a heated substrate. This process can occur in ultrahigh vacuum (UHV) or in the presence of a background gas. PLD is now widely used for epitaxial growth of metal oxide films and known as a suitable laboratory research technique for fabrication of high-quality epitaxial layers [OT05]. This technique provides many advantages for oxide epitaxy, some of which can be hardly achieved using other growth

2 Literature Review

techniques such as MBE, sputtering or MOCVD. A fast pulsed laser can condense the energy of emitted photons in a very short time, giving rise to very high peak energy. Thus, ablated materials can be evaporated without any change in the composition¹. This is a prominent advantage especially for making complex oxide films whose elements have a high melting point. The other significant advantages of PLD are the ability to change background pressure easily during the deposition from UHV to a some-mbar range enabling control of crystalline phase stability and growth stoichiometry, as well as the relatively simple growth of complex multilayer structures. While the basic setup is simple in comparison to many other deposition techniques, the detailed mechanisms of PLD are very complex. They include the ablation of the target material by the laser irradiation, the development of a plasma plume with high energetic ions, electrons and neutral particles, the propagation of the plume in direction normal to the target surface and the crystal growth of the epitaxial film itself. The processes, and as a consequence the properties of the deposited films, are strongly dependent on many parameters (e.g. the laser fluency and wavelength, the structural and chemical composition of the target, the ambient gas pressure, the substrate temperature and the distance between the target and the substrates etc.) which have to be found and optimized experimentally.

Despite the mentioned advantages of PLD, some shortcomings have been identified in use of this deposition technique. One of the major problems is the splashing or the deposition of particulates on the film. The physical mechanisms leading to splashing include the surface boiling, expulsion of the liquid layer by shock wave recoil pressure and exfoliation. The size of particulates may be as large as a few microns. Another problem is the narrow angular distribution of the ablated species, which is generated by the adiabatic expansion of laser produced plasma plume and the pitting of the target surface. These features usually limit the use of PLD for production of a large area uniform thin films. So far PLD has not been fully deployed in industry.

Molecular beam epitaxy

MBE (or solid-source MBE) is normally defined as the deposition of epitaxial films onto heated single crystalline substrates using atomic and molecular beams of the required elements produced from Knudsen cells under UHV conditions [JJ04]. According to the definition, MBE is basically a sophisticated version of vacuum deposition. The degree of sophistication solely depends on requirements of individual research in achieving its specific objectives [CP85]. In contrast to MOCVD, which proceeds near thermodynamic equilibrium, MBE growth is governed mainly by kinetics of the molecular beams reacting with crystalline surfaces. The growth process far from thermal equilibrium makes MBE (similar to PLD) very attractive for fabrication of novel and metastable compound materials which do not exist in nature. Unlike very complicated plasma physics underlying the PLD processes, thermal evaporation in vacuum is comparably simple, well understood and allows for fine adjustment of the proper parameters. MBE possesses

¹It does not necessary mean that the composition of the epitaxial film remains exactly the same like the composition of the ablated target.

thus essential advantages over PLD such as higher versatility and more degrees of freedom, which especially important in fabrication of complex compound materials and multilayered systems, at least for constituting elements with moderate temperatures of vaporization. Recent availability of radio-frequency (rf) plasma sources extended the number of standard MBE applications to the successful growth of nitride and oxide thin films. Furthermore, because of the UHV environment, MBE process is compatible with a number of powerful techniques for *in-situ* growth control and analysis, such as RHEED, LEED, AES, secondary ion mass spectroscopy (SIMS), X-ray induced photoelectron spectroscopy (XPS), etc., which certainly give substantial advantages to MBE over other material preparation techniques.

2.3.2 Typical approaches to radical-source MBE of ZnO

An enormous number of studies has been devoted to different aspects of MBE of ZnO (see Review [ÖAL⁺05] and references therein). Briefly summarizing these extensive research efforts, one can note that the optimal conditions for the deposition of ZnO films resulting in a 2D growth and relatively high crystal perfection are found to be either slightly O-rich or stoichiometric with growth temperatures varying in the range of $T_g = (520 - 560) ^\circ\text{C}$ or even higher [CKHY00, KSMY03, ESBM⁺06]. The desire to work under excess of O originates from the aspiration to reduce the number of O vacancies having been considered for quite long time as possible native donors. Independently on the substrate material, determination of the true stoichiometry in the case of ZnO epitaxial growth is a rather difficult task. Unlike other II-VI compounds, ZnO does not have any distinct feature allowing for a precise determination of the stoichiometry (like, changing the (2×1) and $c(2 \times 2)$ surface reconstructions during growth of ZnSe, e.g. [SBH04]). Indirect information can be obtained from the variation of the average growth rate with systematic change of O-gas flow or Zn-flux intensity [KSMY03]. This procedure, based on the *ex-situ* determination of the layer thickness, is time consuming and needs to be repeated from time to time because of gradual degradation of plasma sources due to the high reactivity of O radicals (see Chapter 3). RHEED oscillations give an alternative tool to determine the growth rate *in-situ*, if growth fashion and surface quality allow it [CKH⁺02]. In addition to the careful choice of the substrate material, growth temperature and stoichiometry, a buffer or nucleation layer (NL) is another important factor strongly affecting the growth mode. The concept of LT nucleation is now widely used for MBE of ZnO on substrates with a large lattice mismatch, defined as $\Delta a/a = (a_{\text{film}} - a_{\text{sub}})/a_{\text{sub}}$, where a_{film} and a_{sub} are the a -lattice constants of the film and the substrate, respectively, or even different crystal symmetry [NTT⁺01, CKHY00]. This layer is typically grown at $T_g = (300-350) ^\circ\text{C}$ and then annealed at higher temperatures to improve the surface morphology and to enhance the interaction between threading dislocations (TDs), generated in the layer due to the large lattice mismatch. It must be noted, that formation of the NL and its subsequent recrystallization are key steps in the whole growth process mainly defining the crystal perfection of the fabricated films.

2.3.3 Substrates

Epitaxy (literally "places-(epi) and arrangement-(taxy) from Greek) is essentially a recrystallization process in which gaseous atoms condense on a template created by a substrate to form a single crystal film. Thus, the crystallographic properties of the substrate are of obvious importance. In the ideal case, the deposited film is perfectly matched to the substrate, e.g. it has a crystal symmetry, in-plane lattice constants and thermal expansion coefficients identical with the substrate. Therefore, if possible one uses a substrate of the same material as the epitaxial film, i.e. one works in a homoepitaxial regime. Otherwise, the process is called heteroepitaxy with its intrinsic drawbacks as lattice and thermal mismatches, strain, and resultant misfit dislocations.

Recent advances in the bulk growth already made ZnO wafers available and have reduced their price significantly over the last several years. However, the crystal quality, surface polishing and pregrowth preparation of these crystals are still issues for current research. For this reason, most ZnO structures have been so far fabricated on sapphire (Al_2O_3). Sapphire is commonly used for ZnO growth due to its low cost, high crystal perfection and availability of large area wafers. The main disadvantage of sapphire substrates is very poor structural and thermal match to ZnO. Heteroepitaxial ZnO layers have been also grown on several other substrates, such as $\text{CaF}_2(111)[\text{KCZ}^+00]$, $\text{MgAl}_2\text{O}_4(111)[\text{CHK}^+00]$, Si, SiC [ASSY05, ASSY06], GaAs, ScAlMgO_4 , as well as on GaN/ Al_2O_3 templates. Lattice parameters and thermal expansion coefficients of these substrate materials are listed in Table 2.1.

Growth of ZnO epilayers on different planes of sapphire

Although sapphire or $\alpha\text{-Al}_2\text{O}_3$ has a rhombohedral structure, Pearson's Handbook and other references use the equivalent hexagonal cell that is three times larger than the basic rhombohedral unit [VC91]. Sapphire has the space group of $R\bar{3}c$ and is mainly composed of ionic bonds. The unit cell described in terms of hexagonal Miller-Bravais indices consists of six close packed (0001) planes of O^{2-} ions, sandwiching 12 planes of Al^{3+} ions that occupy two thirds of the available octahedral voids created by the O^{2-} ions. Such construction contains 30 ions in total, i.e. 12 Al^{3+} ions and 18 ions of O^{2-} . The rhombohedral and hexagonal unit cells of sapphire, as well as unreconstructed basal c -plane perspective views for both unit cells are shown in Fig. 2.3 [LE02]. The faceting of the sapphire crystal is shown in Fig. 2.4.

Historically, the basal plane of sapphire [(0001) or c -plane, Fig. 2.4] is one of the first substrates employed for ZnO growth. For the films grown on c -plane sapphire, the orientational relationship along the direction normal to the surface is $\text{ZnO } [0001] \parallel \text{sapphire } [0001]$, but two types of in-plane rotational domains are observed as a result of the following alignments: $\text{ZnO } [1\bar{2}10] \parallel \text{sapphire } [1\bar{1}00]$ and $\text{ZnO } [10\bar{1}0] \parallel \text{sapphire } [11\bar{2}0]$ [FIY⁺00], respectively. The alignment $\text{ZnO } [10\bar{1}0] \parallel \text{sapphire } [11\bar{2}0]$ corresponds to a 30° rotation between ZnO and sapphire a -axes, presumably due to preferential Zn bonding with oxygen atoms of sapphire (Fig. 2.5). Because of the large lattice mismatch

2.3 Fabrication of ZnO and ZnO-based hetero-structures

Material	Space group symmetry	Crystal structure	Lattice constants $a(\text{\AA})$ $c(\text{\AA})$	Thermal expansion coefficient, $\alpha(\text{K}^{-1})$ $\alpha_a(10^{-6})$ $\alpha_c(10^{-6})$
ZnO	P ₆ mc	Hexagonal	3.252 5.213	2.9 4.75
GaN	P ₆ mc	Hexagonal	3.189 5.185	5.17 4.55
AlN	P ₆ mc	Hexagonal	3.112 4.980	5.3 4.2
α -Al ₂ O ₃	R $\bar{3}$ c	Hexagonal	4.757 12.983	7.3 8.1
6H-SiC	P ₆ mc	Hexagonal	3.080 15.117	4.2 4.68
ScAlMgO ₄	R $\bar{3}$ m	Hexagonal	3.246 25.195	
MgAl ₂ O ₄	Fd $\bar{3}$ m	Spinel	8.083	7.45
		Cubic	5.431	11.9
Si	Fd $\bar{3}$ m	Cubic	5.430	3.59
GaAs	F $\bar{4}$ 3m	Cubic	5.652	6.0

Tabelle 2.1: Lattice parameters of a number of the prospective substrate materials for ZnO. (From [ÖAL⁺05, Amb98]).

2 Literature Review

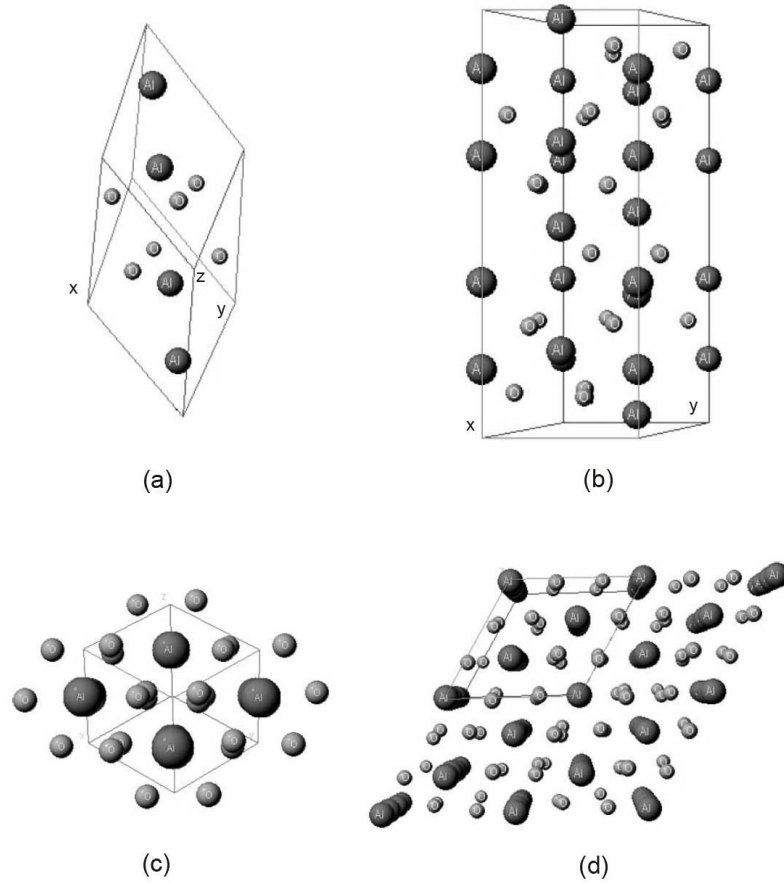


Abbildung 2.3: The unit cell of sapphire: (a) rhombohedral unit cell; (b) hexagonal unit cell. Perspective views in $(2 \times 2 \times 1)$ unit cells: (c) along the $[0001]$ direction in a rhombohedral unit cell; (d) along the (0001) direction in hexagonal unit cell. (From [LE02]).

even after the 30° in-plane rotation (18% vs. 32%) and existence of rotational domains, as-grown ZnO films as a rule show large mosaicity, high residual carrier concentrations, and low mobilities making their use for optoelectronic applications a challenge [FIY⁺00].

A breakthrough towards utilization of (0001) sapphire substrates has been made by Y. Chen *et al.* [CKHY00] in the year 2000, who suggested to insert a very thin MgO buffer layer at the ZnO/sapphire interface². It was shown that the MgO buffer leads to complete elimination of the rotational domains, suppression of the columnar growth, improvement of crystal quality as well as optical and electrical properties. Moreover, as it was uncovered several years later, by varying the buffer layer thickness, ZnO polarity

²Compare with initial nitridation of sapphire substrate in the case of GaN growth [LE02].

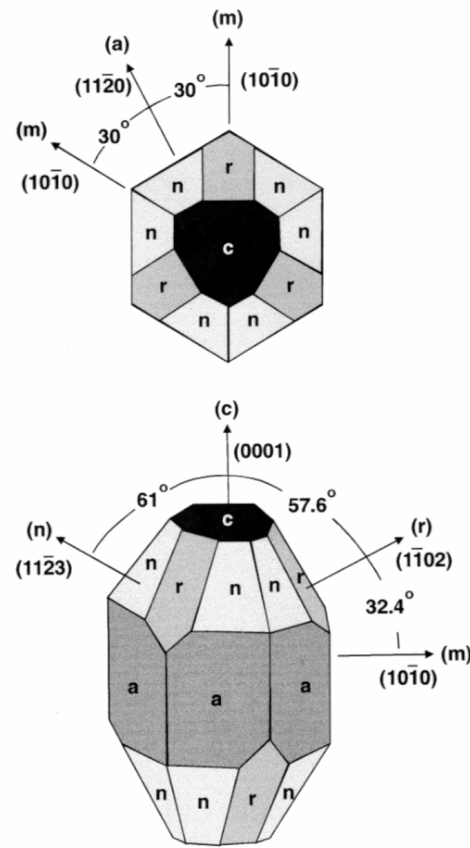


Abbildung 2.4: Rhombohedral structure and surface planes of sapphire. (From [Amb98]).

control can be achieved [KMSY04]. The physical mechanisms related to the influence of the buffer are still not well understood. Possible explanations are: (a) lowering the surface energy through a wetting process, creating nucleation sites through a 2D to three dimensional (3D) growth mode transition (for cubic (111)-oriented MgO), and reducing defect density by introducing dislocation interactions [CHK⁺01]; (b) formation of a wurtzite MgO wetting layer at the interface and polarity conversion after formation of the 3D rocksalt islands [KMSY04]; or (c) formation of a spinel MgAl₂O₄ structure forced by high temperature annealing [PESB⁺06]. Anyhow, this experimental finding works well when the growth process is carefully optimized. The effect of polarity conversion can, however, induce deterioration of the film quality. The change of the crystal polarity occurs at the MgO buffer thicknesses of (1-3) nm, where the true layer thickness can be hardly controlled because of a 3D growth mode. In this range fluctuations of the MgO coverage result in a local polarity conversion and appearance of the inversion domains, strongly affecting optical properties [STL⁺07].

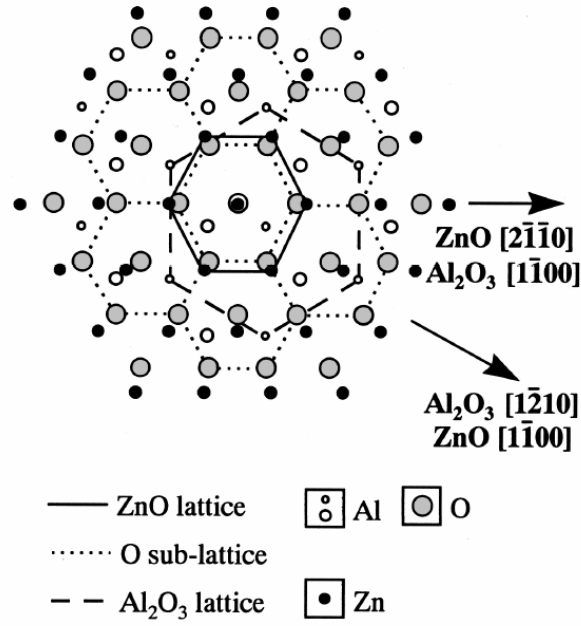


Abbildung 2.5: Schematic diagram showing the epitaxial relationship of ZnO grown on *c*- plane sapphire. (From [CBK⁺98]).

As an alternative to *c*-plane sapphire, $(11\bar{2}0)$ Al₂O₃ substrates (or *a*- plane) have been proposed for the epitaxy of ZnO [FIY⁺00]. One of the major advantages of *a*-plane sapphire, known already from the earliest stages of the III-nitride epitaxy [LE02], is the existence of the cleavage plane perpendicular to the surface, which is potentially advantageous for forming edge-emitting lasers. In addition, since the lattice mismatch between GaN and *a*-plane sapphire is less than 2% (less than 1% for ZnO), it is expected that better quality films may be achieved, despite the difference in the planar symmetry. Figures 2.6 and 2.7 present an original crystallographic model, developed by *D. Doppalapudi et al.* for the $(11\bar{2}0)$ Al₂O₃/GaN interface [DIBM99], which can be easily adapted to the ZnO growth. Figure 2.6(a) shows $20 \times 20 \text{ \AA}$ crystallographic projections of $(11\bar{2}0)$ and (0001) planes of sapphire and GaN, respectively. The projections of the cleavage planes in the two lattices are marked in Fig. 2.6(a). The line in sapphire is the projection of $(10\bar{1}2)$ plane (*r*- plane), which is shown to be approximately parallel to the projection of $(11\bar{2}0)$ plane in GaN. However, it should be noted that there is a 2.4° rotation in between these two cleavage axes across the interface. The supercell of epitaxial overlap is outlined by the dotted rectangles ($\sim 13 \times 16.5 \text{ \AA}$) in the two projections. Figure 2.6 (b) shows superposition of the two projections. The thickness in the *z* direction is restricted to a monolayer in each lattice, to include only the atoms closest to the interface that participate in the chemical bond. Figure 2.7 depicts the cross-section of the sapphire/GaN interface showing the bonding across the interface. In Fig. 2.7(a) the cross-section at

the $[1\bar{1}00]$ zone-axis in GaN (which is equivalent to the $[1\bar{1}00]$ zone-axis in sapphire), and in Fig. 2.7 (b) the cross-section at the $[11\bar{2}0]$ zone-axis in GaN ($[0001]$ zone-axis of sapphire) are presented. The cross section is taken from the line of best match, i.e., the edges of the supercell marked by a rectangle in Fig. 2.6. In these two models, the z range is limited to 2 Å to simplify the picture, and the same kind of lattice matching is assumed as in Fig. 2.6(b). The supercell of epitaxial overlap is marked by the rectangles in the two projections in Fig. 2.6(a). With this supercell, the lattice match is as follows: six $(10\bar{1}0)$ planes of GaN match with four planes of $(10\bar{1}0)$ of sapphire, resulting in a lattice mismatch of 0.56%. In the perpendicular direction, eight planes of $(11\bar{2}0)$ GaN match with one (0001) plane of sapphire, resulting in a mismatch of -1.75%. In the case of ZnO these lattice mismatches are 0.254% and 0.192%, respectively³.

Based on this specific lattice matching and coining the term "uniaxial locked epitaxy", *Fons et al.* [FIY⁺00] performed a study of the ZnO MBE on a -plane $(11\bar{2}0)$ sapphire, including a detailed analysis of the initial growth stages. The out-of-plane and in-plane orientational relationships were found to be ZnO $[0001] \parallel$ sapphire $[11\bar{2}0]$ and ZnO $[11\bar{2}0] \parallel$ sapphire $[0001]$, respectively. According to *Fons et al.*, use of a -plane sapphire for ZnO growth has resulted in remarkable improvements in electrical properties and surface smoothness in comparison to c -plane substrates. Specifically, the residual carrier concentration was decreased to $6 \cdot 10^{16} \text{ cm}^{-3}$ with electron mobility higher than $120 \text{ cm}^2 \text{ V}^{-1} \text{ s}^{-1}$ in contrast to $30 \text{ cm}^2 \text{ V}^{-1} \text{ s}^{-1}$ for films grown on c -plane sapphire, while the surface morphology was kept smooth with root mean square (rms) roughness of less than 0.3 nm as revealed by atomic-force microscopy (AFM). The Hall data were presented for 1.2 μm -thick films grown at 350 °C and most likely measured at RT. As it became obvious several years later, the Hall-effect measurements of ZnO grown on sapphire require very critical evaluation due to a complex inherent substructure of the films and nonuniform carrier distribution induced by a degenerate interface layer and possible Al upwards diffusion from the substrate. In the year 2001, *K. Nakahara et al.* [NTT⁺01] introduced the concept of a LT ZnO nucleation layer ($T_g = 350 \text{ °C}$) with its subsequent annealing ($T_a = 600 \text{ °C}$), and deposition of the main ZnO layer at higher growth temperature ($T_g = 600 \text{ °C}$). Similar to GaN, low-temperature nucleation is often used when growing on sapphire, regardless of its orientation. One has to note, however, that despite the elimination of the rotational domains and seemingly improved electrical properties [FIY⁺00, NTT⁺01], so far reported XRD data for ZnO epitaxial films grown on a -plane sapphire were always worse than the best results achieved for ZnO grown on the c -plane with MgO buffer. Obviously, this is the main reason limiting a number of reliable communications for direct comparison of ZnO films grown on these substrates.

Very recently, r -plane sapphire was used as a wafer for preparation of non-polar a -plane $(11\bar{2}0)$ ZnMgO epilayers and ZnO quantum wells embedded in ZnMgO barriers [CBL⁺07].

³The lattice constants used in calculations: $a = 4.757 \text{ Å}$, $c = 12.983 \text{ Å}$ for Al_2O_3 ; $a = 3.189 \text{ Å}$ and $a = 3.252 \text{ Å}$ for GaN and ZnO, respectively [ÖAL⁺05].

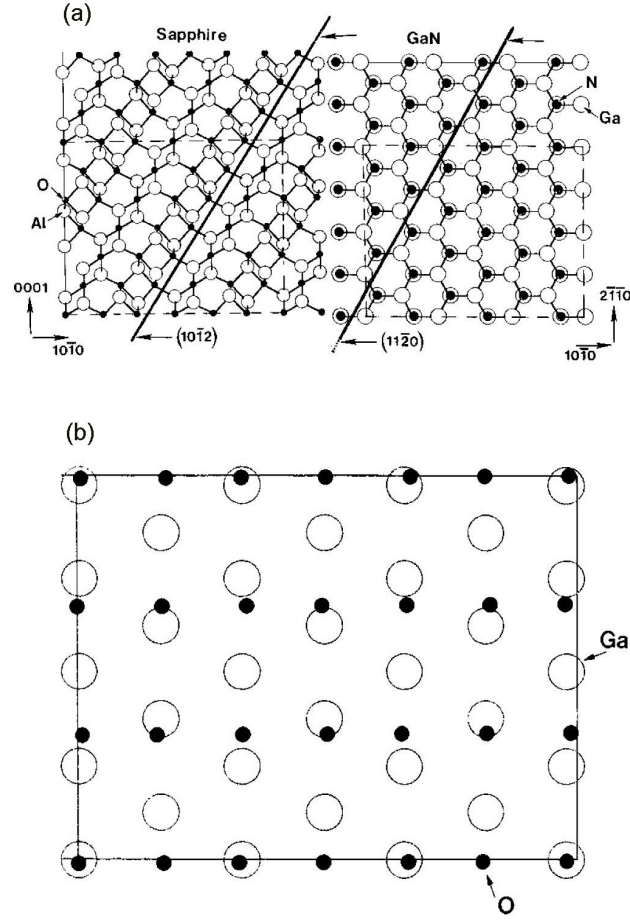


Abbildung 2.6: Projections of sapphire and GaN lattices (a) $(11\bar{2}0)$ and (0001) planes of sapphire and GaN respectively, showing the cleavage planes. The rectangles depict the supercells of overlap. (b) A supercell of GaN (0001) epitaxy on sapphire $(11\bar{2}0)$. (From [DIBM99]).

ScAlMgO₄ substrates

Up to now the most impressive results in the fabrication of ZnO and ZnO-based heterostructures have been achieved on practically lattice matched ScAlMgO₄ (SCAM) substrates, introduced by A. Ohtomo *et al.* [OTS⁺99]. SCAM is considered to be a natural superlattice composed of alternating stacked layers of the wurtzite (0001) -face $(\text{Mg,Al})\text{O}_x$ and the rocksalt (111) -face of ScO_y (Fig. 2.8). The lattice constants of hexagonal ScAlMgO₄ are $a = 3.246 \text{ \AA}$ and $c = 25.195 \text{ \AA}$, giving rise to an in-plane lattice mismatch as small as 0.09%. Data for thermal expansion coefficient are not available in literature. The wide band gap and an insulative nature permit neglecting the contribution of the wafer to the electrical conductivity (which is not the case for ZnO homoepitaxy) and make SCAM substrates very attractive for studying electrical as well

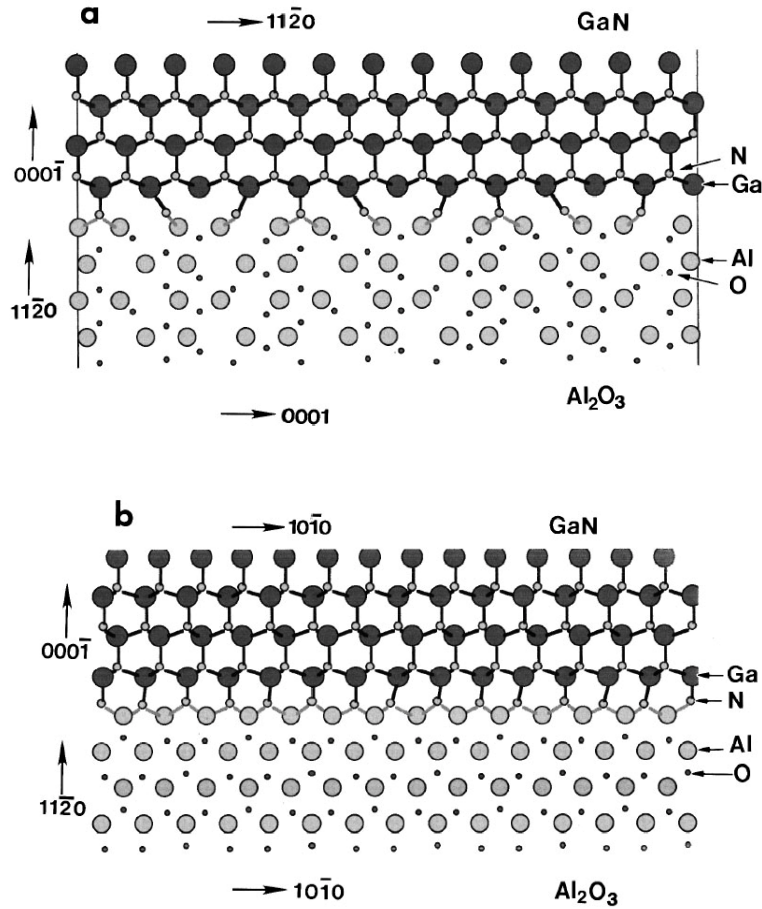


Abbildung 2.7: Crystallographic model of cross-sectional view of the interface, seen at (a) $[1\bar{1}00]_{\text{GaN}}$ zone-axis and at (b) $[11\bar{2}0]_{\text{GaN}}$ zone-axis. (From [DIBM99]).

as optical (e.g., optical transmittance, photoluminescence (PL)) properties of the deposited epitaxial films. However, several disadvantages currently hinder worldwide use of these crystals. Among them are the high cost (much higher than even for ZnO bulk crystals) and limited availability on the market, as well as known instability against cleavage along the basal plane [WSM02].

ZnO substrates

As it was already briefly mentioned, the fabrication of ZnO substrates suitable for epitaxial overgrowth is an issue in itself. Growth of bulk ZnO is mainly carried out by three methods: hydrothermal, vapor phase, and melt growth [ÖAL⁺05]. The mostly widespread and powerful technique is hydrothermal growth. However, the hydrothermal crystals inevitably incorporate alkali metals (K and Li) and small amounts of metallic impurities from the solution. Growth of ZnO from the melt is very complicated

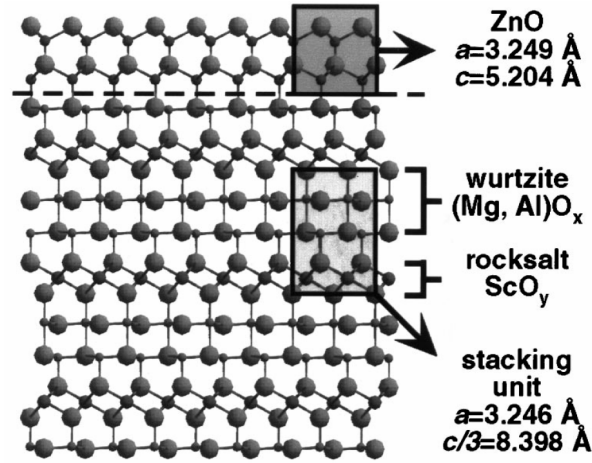


Abbildung 2.8: Schematic illustration of ScAlMgO₄ crystal structure composed of alternating stack of wurtzite (Mg,Al)O_x(0001) and rocksalt ScO_y(111) layers. Epitaxially grown ZnO is attached by assuming that the wurtzite layer of ScAlMgO₄ coherently continues with that of ZnO. (From [OTS⁺99]).

because of its high melting point ($T_f = 1975 \text{ }^\circ\text{C}$) and extremely high vapor pressure. Growth by vapor-phase deposition is difficult to control. Despite the high commercial interest in bulk ZnO single crystals as substrates for GaN growth, as well as for ZnO homoepitaxy, and inspite of the essential progress achieved over the last several years (2000 - 2007), available ZnO wafers are still quite expensive, small in size and show very low reproducibility of their crystal perfection, background carrier concentration and often have poor surface morphology.

Si substrates

Although sapphire is frequently used as a substrate for the growth of ZnO, significant effort has been focused on the growth of epitaxial ZnO films on Si wafers. Such work is motivated by the availability of inexpensive large diameter substrates with higher thermal conductivity, easier device fabrication, and the potential of multifunctional device integration with Si electronics. The direct growth of ZnO on Si usually results, however, in amorphous or polycrystalline films due to the oxidation of the Si surface with formation of an amorphous silica layer, as well as the large lattice (15.4% for Si(111) plane) and thermal expansion coefficient (60%) mismatches [GAC⁺08]. The oxidation can be understood in view of the fact that the formation enthalpy of SiO₂ is much larger in magnitude than that of ZnO (i.e., $\Delta H(\text{SiO}_2) = -910.7 \text{ kJ/mol}$ vs $\Delta H(\text{ZnO}) = -350.5 \text{ kJ/mol}$ [Lid94]), and therefore the formation of amorphous oxide is favored over the ZnO formation on Si surface. In order to improve the crystallinity of ZnO grown on Si, intermediate layers including Si₃N₄ [IFN⁺00b], GaN [NKB01], CaF₂ [KKO⁺04], Al₂O₃, ZnS, Al, AlN, MgO, Lu₂O₃ and low-temperature grown ZnO have been used as buf-

fer layers [GAC⁺08]. So far, single-crystalline ZnO films have only been achieved in a few cases in which other issues such as crack formation upon postgrowth cooling and complicated multistep buffer layer processing also exist. Despite all these efforts, the importance of Si as a substrate for ZnO epitaxy is still underestimated.

2.3.4 ZnO-based alloys and their heterostructures

A crucial step in designing modern optoelectronic devices is the realization of band-gap engineering. The modulation of the band gap in the case of ZnO has been suggested by using ZnMgO and ZnCdO mixed crystals [MSK⁺01]. A fundamental problem in fabrication of the alloys is a difference in the crystal structure of the binaries: ZnO is hexagonal (wurtzite), while MgO and CdO are cubic (rocksalt) materials. Despite a similar tetrahedral ionic radius ($\text{Zn}^{2+} = 0.74 \text{ \AA}$, $\text{Mg}^{2+} = 0.72 \text{ \AA}$, $\text{Cd}^{2+} = 0.95 \text{ \AA}$), the different crystal symmetry leads to the low solubility of Mg (Cd) in wurtzite ZnO lattice and forces phase separation. Figure 2.9 shows a typical diagram in which the band gap energies of ZnO (3.37 eV), MgO (5.4 eV) and CdO (2.2 eV) are plotted versus their lattice constants (red circles, from Makino *et al.* [MSKK05]). Note that the band gap of MgO is often given as $\sim 7.8 \text{ eV}$ [ÖAL⁺05, JSdW06], and that the *a*-lattice constant corresponds to wurtzite for ZnO and to rocksalt for MgO and CdO. The available theoretical data for hypothetical wurtzite MgO (CdO) are shown in the same diagram by the blue circles [JSdW06]. As one can easily see, various combinations of these isoelectronic materials (ZnO, MgO and CdO) can cover in principle a wide spectral range from the near infrared to UV, though with the complication of different crystal symmetry and the lattice mismatch. An attempt to overcome these obstacles is the main task of the current work.

ZnMgO alloys

Ternary ZnMgO has been considered as a suitable material for the barrier layers in ZnO/ZnMgO heterostructures. According to the phase diagram for the ZnO-MgO binary system, the thermodynamic solubility limit of MgO in ZnO is less than 4 mol % [SKH59]. However, in the year 1998, A. Ohtomo *et al.* have succeeded in the preparation of metastable wurtzite $\text{Zn}_{1-x}\text{Mg}_x\text{O}$ alloys with a Mg content as high as $x = 0.33$ [OKK⁺98]. The *a*- and *c*- lattice constants of the fabricated alloys changed orderly (*a*-increased, while *c*- decreased) with Mg content. The maximal change of the lattice constants was, however, much smaller than 1% within the solid solubility range (Fig. 2.10). The RT band gap E_g , extracted from transmittance spectra employing α^2 vs E_g plot and assuming an $\alpha^2 \propto (h\nu - E_g)$ relationship, where α is the absorption coefficient and $h\nu$ is the photon energy, linearly increased with x up to 4.15 eV (3.9 eV for single phase films at $x = 0.33$) for $0 \leq x \leq 0.36$ and saturated at higher Mg concentrations due to MgO segregation, as it is shown in Fig. 2.10 (inset). The upper solubility limit of $x = 0.33$ was overcome in the year 1999 by A. Sharma *et al.* [SNM⁺99]. The observation of intense near band edge PL and excitonic features in transmission spectra at room temperature from wurtzite alloys up to $x = 0.36$ was reported.

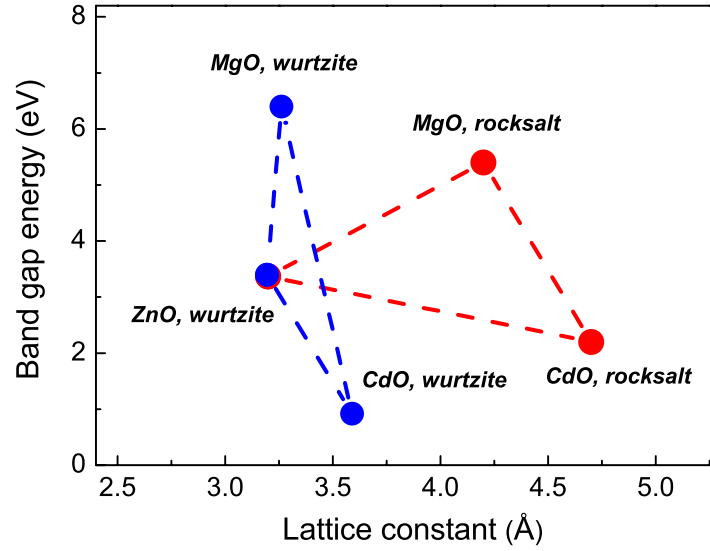


Abbildung 2.9: The energy gap versus the a -lattice constant for wurtzite ZnO and rocksalt MgO (CdO) (red circles, from [MSKK05]). The theoretical data for hypothetical wurtzite MgO and CdO are plotted by the blue circles [JSdW06].

While the PLD technique was widely used for fabrication of ZnMgO alloys and ZnO/ZnMgO QWs, a first very short communication about growth of ZnMgO/ZnO heterostructures by radical-source MBE appeared only in the year 2000 [CKH⁺00]. The authors reported about ZnMgO layers with Mg content of $x = 0.168$ deposited on ZnO/MgO/sapphire (0001) templates at $T_g = (550-650)^\circ\text{C}$. K. Ogata *et al.* [OKT⁺03] have used a -plane sapphire for growing ZnMgO. The growth experiments were performed at $T_g = 500^\circ\text{C}$ under metal-rich conditions and led to the phase separation at $x = 0.22$, as well as to dramatic surface roughening. Very recently, K. Koike *et al.* [KHN⁺05] succeeded in fabrication of single-phase wurtzite $\text{Zn}_{1-x}\text{Mg}_x\text{O}$ alloy films with $0 \leq x \leq 0.43$ and maximal optical gap $E_g = 4.45$ eV on Si(111) substrates with a 10 nm-thin ZnO/CaF₂ buffer layer. The Mg solubility limit was found to be affected by the growth temperature shifting from $x = 0.30$ at $T_g = 600^\circ\text{C}$ to $x = 0.45$ at $T_g = 350^\circ\text{C}$.

ZnO/ZnMgO heterostructures

Probably the first report on ZnO/ZnMgO heterostructures can be found in [OKS⁺98a], where samples containing 10 periods of (1.7-12) nm-thick ZnO QWs separated by 6.2 nm-thick $\text{Zn}_{0.8}\text{Mg}_{0.2}\text{O}$ barriers have been presented. These structures were grown by PLD at $T_g = 650^\circ\text{C}$ on (0001) sapphire substrates with an introduced 100 nm-thick ZnO buffer and showed hexagonally shaped grains and steps with a height of 0.52 nm on the surface indicating a spiral growth mode typically induced by screw dislocations.

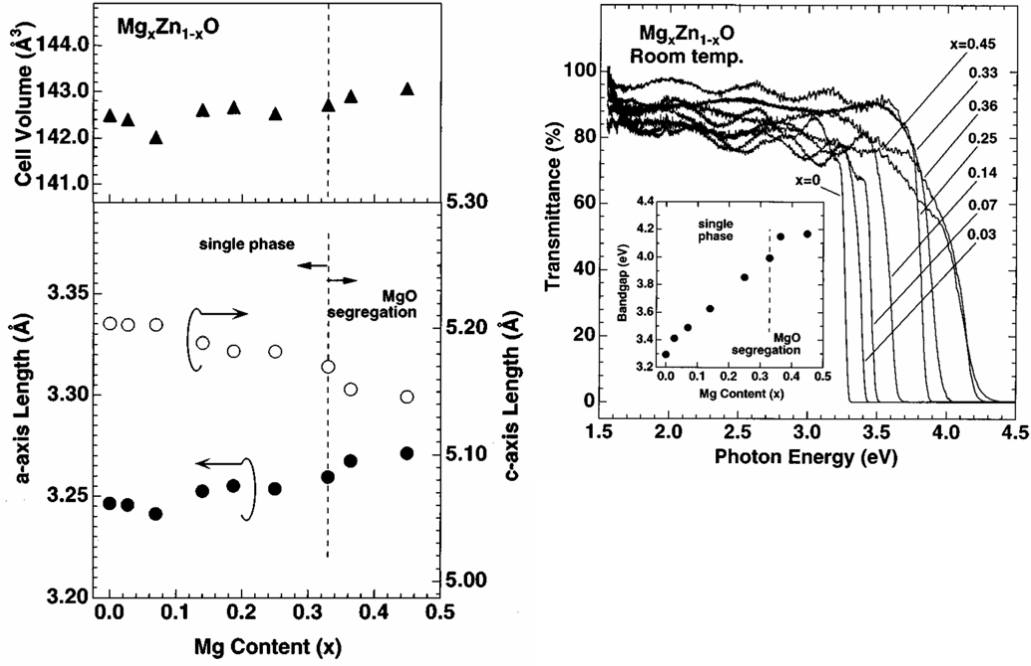


Abbildung 2.10: (Left) Mg content dependences of the a - and c -axis lattice parameters and the cell volume of $\text{Mg}_x\text{Zn}_{1-x}\text{O}$ films. Segregation of the MgO impurity phase was observed for $x \geq 0.33$ of Mg content. (Right) Transmittance spectra of $\text{Mg}_x\text{Zn}_{1-x}\text{O}$ films measured at room temperature. The inset shows the band gap (E_g) determined from the spectra assuming an $\alpha^2 \propto (h\nu - E_g)$ dependence, where α and $h\nu$ are the absorption coefficient and the photon energy, respectively. (From [OKK⁺98]).

For well layer thicknesses smaller than 5 nm, the PL peak and absorption edge in the photoluminescence excitation (PLE) spectra showed a blue shift, ascribed as an indication of a QSE. Moreover, the PL peaks demonstrated considerable broadening and Stokes shift by about 50 meV, which was related to the QW layer thickness fluctuations induced by the spirally growth mode, and to Mg content fluctuations in the barriers, correspondingly [OKO⁺99]. Despite the obvious progress achieved in material preparation, the structures possessed certain drawbacks attributed to the relatively rough interfaces due to epitaxy on lattice-mismatched substrates. Using SCAM substrates resulted in significantly improved crystal quality and surface morphology and made it possible to observe in ZnO/ZnMgO MQWs many interesting optical phenomena culminating in optically pumped lasing with a threshold of 11 kW/cm² at RT (see for review [OTK⁺00, MSKK05]).

The progress in preparation of ZnO/ZnMgO QWs by other growth techniques was for quite a long time not very exciting. After a first and cautious communication of Y.

2 Literature Review

Chen et al. about a cathodeluminescence (CL) study of a 25 nm-thick ZnO layer embedded in 200 nm-thick $\text{Mg}_{0.15}\text{Zn}_{0.85}\text{O}$ barriers prepared by radical-source MBE [CKH⁺00] in the year 2000, there was a gap for more than four (!) years. The main reasons for such an unusual situation were, obviously, the phase separation problem in ZnMgO alloys discussed previously, and the very poor quality of the interfaces which did not permit to fabricate QWs in view of the very small exciton Bohr radius of ZnO (1.8 nm). In 2004 *K. Koike et al.* [KHN⁺04] have presented a $\text{Zn}_{0.6}\text{Mg}_{0.4}\text{O}/\text{ZnO}/\text{Zn}_{0.6}\text{Mg}_{0.4}\text{O}$ heterostructure grown by MBE, where the thickness of the ZnO layer was about 50 nm. Later, the same group has presented a simple field-effect transistor based on a $\text{Zn}_{0.7}\text{Mg}_{0.3}\text{O}/20$ nm-thick ZnO/ $\text{Zn}_{0.7}\text{Mg}_{0.3}\text{O}$ heterostructure [KNH⁺05]. At the end of the year 2005 *C. Morhain et al.* [MBL⁺05] reported about existence of a large (0.9 MV/cm) polarization fields in ZnO/ $\text{Zn}_{0.78}\text{Mg}_{0.22}\text{O}$ single and double QW structures grown by MBE on 1 μm -thick ZnO/sapphire (0001) templates. One has to note, that ZnMgO layers of that study have been fabricated at $T_g = (400-480)^\circ\text{C}$ and had rather poor surface morphology as can be seen from the presented RHEED patterns (Fig. 2.11) and reported AFM rms values of the surface roughness of (4-22) nm depending on the growth temperature [MTTD⁺05].

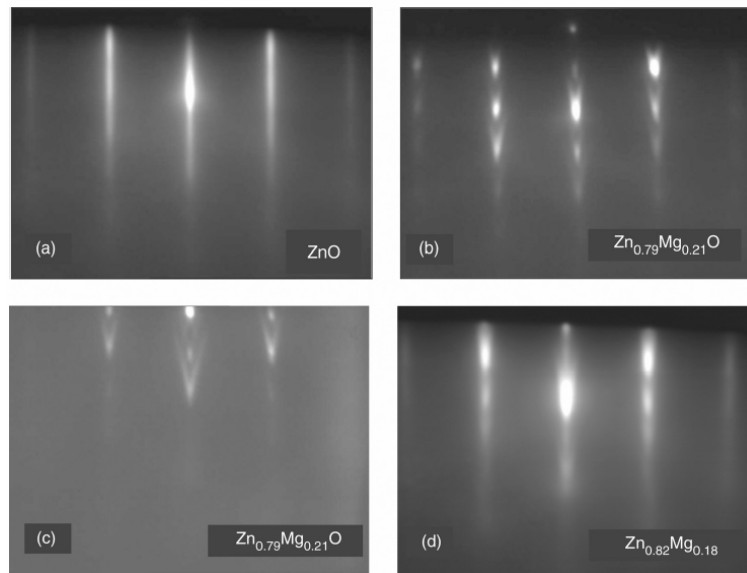


Abbildung 2.11: RHEED patterns along the $[1\bar{2}10]$ direction of (a) ZnO (1 μm) template grown at 520°C , (b) ZnMgO (30 nm) grown at 480°C , (c) ZnMgO (0.4 μm) grown at 480°C and (d) ZnMgO (0.4 μm) grown at 400°C . (From [MTTD⁺05]).

There were also some attempts to fabricate ZnO/ZnMgO QWs by MOCVD and metalorganic vapor-phase epitaxy (MOVPE). *Th. Gruber et al.* [GKK⁺04] reported about a well-controlled incorporation of magnesium in ZnMgO alloys up to $x = 0.1$, as well as

preparation of ZnO/ZnMgO single QWs on 1 μm -thick ZnO/GaN/sapphire templates. MOCVD growth of ZnO/ZnMgO QW structures with a variable QW width and Mg content of about $x = 0.1$ on (1120) sapphire has been also reported by *Zhang et al.* [ZBW⁺05].

ZnCdO

ZnCdO is a potential candidate for devices operating in the visible spectral range. Cubic CdO has a direct band-gap of 2.38 eV and two indirect gaps of about 1.11 eV and 0.95 eV [Tew73, Kof76]; however, its rocksalt structure limits the equilibrium solubility in wurtzite ZnO to a mole fraction of $y = 0.02$ [MSK⁺01]. Previous work on the epitaxy of ZnCdO has not provided a consistent picture on the phase separation limit in nonequilibrium growth. In the year 2001, *Makino et al.* reported about the fabrication of ZnCdO wurtzite alloy films (~ 200 nm-thick) with maximal Cd concentration of $y = 0.07$ by PLD [MSK⁺01]. Figure 2.12 (left panel) shows the Cd content dependence of the FWHMs x-ray diffraction peaks obtained by ω and $\omega - 2\theta$ scans, as well as a - and c - lattice constant dependencies for those films. Both lattice constants were found to be monotonically increasing functions of y and could be fitted by $a = 3.252 + 0.143y - 0.147y^2$ and $c = 5.204 + 0.956y - 5.42y^2$. The right panel of Fig. 2.12 shows respective RT absorption spectra. The bump in the curve for $y = 0.073$ sample was assigned to the formation of a Cd-rich phase. The polynomial fit of the ZnCdO band gap energies given as $E_g = 3.29 - 4.40y + 5.93y^2$ is depicted in the inset to Fig. 2.12. Because the a -lattice lengths of ZnMgO and ZnCdO ternaries were found to be monotonically increasing functions of the alloy compositions, the authors have noted a principal possibility to fabricate perfectly in-plane lattice matched ZnMgO/ZnCdO heterostructures, which is an essential advantage compared to the InGaN/AlGaN system. The perfect lattice match of different layers grown along the polar c -axis of the wurtzite lattice gives the chance to avoid strain and consequently piezoelectric fields strongly affecting optical properties. Figure 2.13 shows the a -axis lengths as a function of the RT band gap energy values for Zn(Cd,Mg)O and Ga(In,Al)N alloys [MSK⁺01].

For quite some time the Cd solubility of $y = 0.07$ with the respective band gap of roughly 2.99 eV has been considered as an upper boundary [MSK⁺01]. Attempts relying on MOCVD [GKK⁺03, BGF⁺06] stayed also below this value, until recently (in the year 2004) the realization of ZnCdO alloys with concentrations as high as $y = 0.697$ in a plasma-enhanced mode has been demonstrated [SNI⁺04]. The authors reported about single-phase wurtzite structures and showed RT PL in the range of (1.85-3.28) eV rising the hope that ternary ZnCdO is a good light emitter. MBE distinguished by its high versatility and the capability of *in situ* growth control has merely yielded limited results. In a first study by *K. Sakurai et al.* [SKK⁺00] performed on a -plane sapphire substrates, an abrupt transition between either wurtzite ZnO or cubic CdO phases has been observed when increasing the Cd/Zn beam pressure ratio (BPR) and only textured films grown at the critical BPR showed blue, strongly Stokes-shifted luminescence (Fig. 2.14). Later work by *J. Chen et al.* [CRL⁺05] has claimed an incorporation of Cd of 0.048 without

2 Literature Review

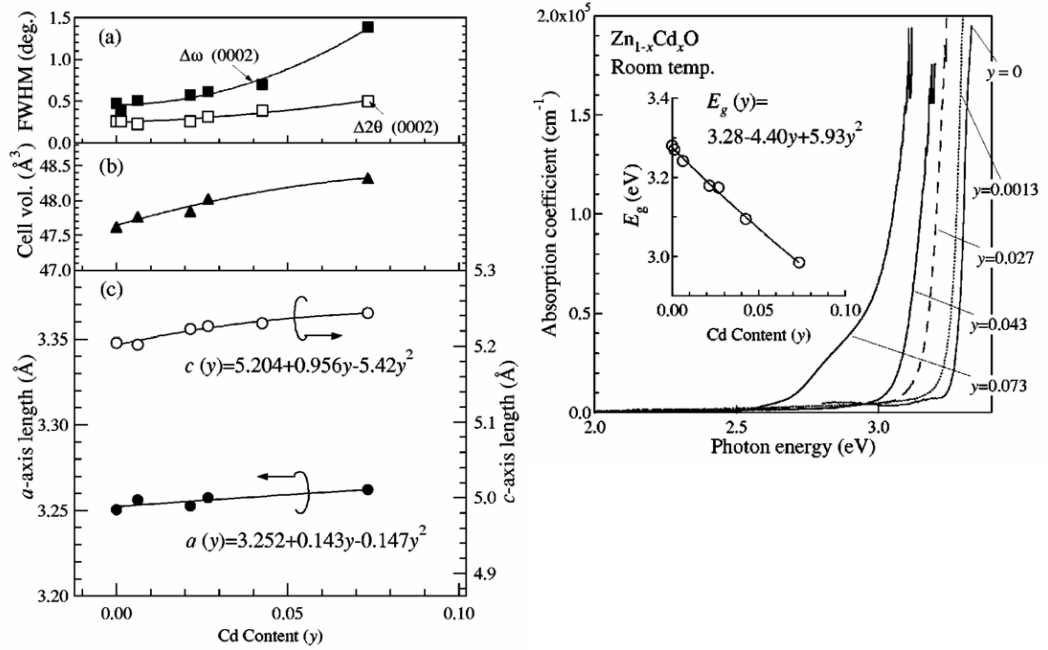


Abbildung 2.12: Left panel: Cadmium content dependence of (a) FWHM values of the (0002) peak in XRD ω and $\omega - 2\theta$ scanned curves, (b) dependence of the cell volume, and (c) dependence of the a - and c -axis lattice lengths of the $\text{Cd}_y\text{Zn}_{1-y}\text{O}$ films grown on sapphire substrates. The solid lines in (c) are fitted lines obtained by using $a = 3.252 + 0.143y - 0.147y^2$ and $c = 5.204 + 0.956y - 5.42y^2$. Right panel: Concentration dependence of absorption spectra of $\text{Cd}_y\text{Zn}_{1-y}\text{O}$ epilayers obtained at room temperature. The curves, from right to left- correspond to those of the samples with $y = 0, 0.0013, 0.027, 0.043$, and 0.073 . (From [MSK⁺01]).

indication of phase separation, however the growth details were practically not specified. The authors mentioned about c - plane sapphire or GaN/sapphire templates as a substrate, Zn- polarity of the as grown films, as well as a growth temperature of $T_g = (400-600)^\circ\text{C}$.

2.4 Conclusion

Since the late 1990s, there is a worldwide resurgence of research interest to ZnO documented by numerous conferences, workshops, symposia and an enormous number of ZnO-related papers [Kli07]. This renaissance is based on the possibility to grow high-quality epitaxial layers, hetero- and QW structures with the main aspiration to obtain a material for blue/UV optoelectronics, including LEDs as an alternative to the GaN-based structures. At the time when this Ph.D. work was initiated there were still many

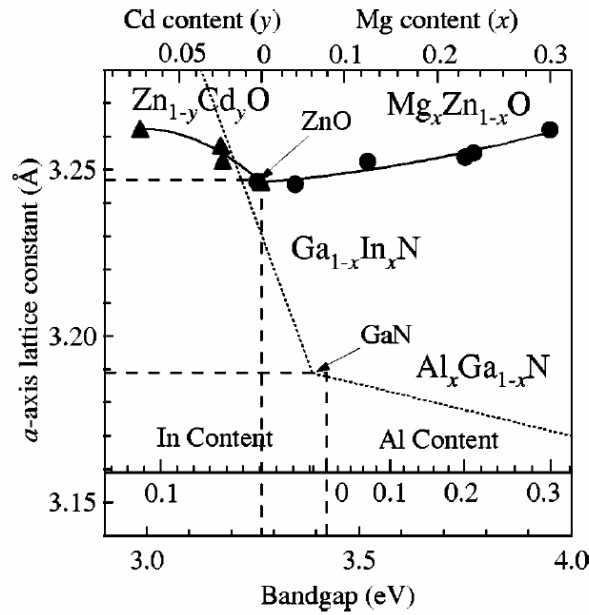


Abbildung 2.13: Optical and structural properties of $\text{Cd}_y\text{Zn}_{1-y}\text{O}$ and $\text{Mg}_x\text{Zn}_{1-x}\text{O}$ alloy films mapped out in a plane of a -axis length and room-temperature band gap energy. The same curves for $(\text{In,Ga})\text{N}$ and $(\text{Al,Ga})\text{N}$ alloys are also shown. Alloy compositions are shown at the top axis. (From [MSK⁺01]).

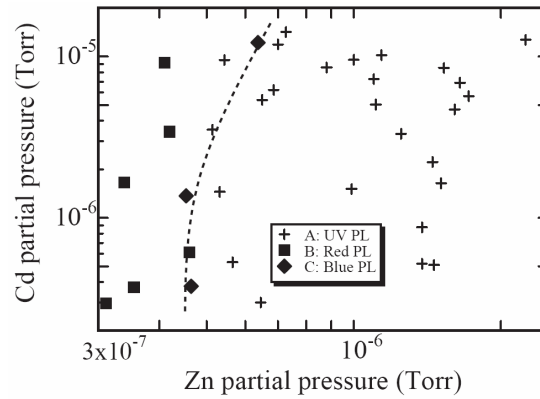


Abbildung 2.14: Obtained films, either type A (transparent), B (red), or C (slightly yellow), against partial pressures of Zn and Cd. Growth temperature was 600 °C for these films. (From [SKK⁺00]).

relatively unexplored critical issues. Despite very fast progress in the material preparation accelerated by the experience obtained from Group III-nitride growth, the field of ZnO-based alloys and heterostructures was just in the initial stage of its development.

2 Literature Review

The first Group II-oxide heterostructures have been mainly prepared by PLD, generally known as a very powerful laboratory technique, which can be, however, hardly adapted for production on the industrial scale. On the other hand, MBE distinguished by its high versatility has been used mainly for the fabrication of ZnO epitaxial films. Summarizing the literature data, one can clearly point out several fundamental as well as technological problems which had to be intensively studied. These are: (1) technological aspects of the MBE growth of ZnO-related materials including design of the effusion cells and pumping system, operating with rf plasma sources, substrate heating etc.; (2) fabrication of high-quality epitaxial films on easily available substrates, e.g. sapphire, instead of SCAM; (3) the solid solubility limits of Mg and especially Cd in Zn(Mg,Cd)O ternaries under nonequilibrium growth. Possibility to use this material system for the effective band-gap engineering; (4) MBE growth of well-defined hetero- and quantum well structures demonstrating high structural and optical quality; (5) *p*-type doping of ZnO-related materials. The problem of a doping asymmetry.

In this work I try to experimentally examine most of these issues and present one of the first growth approaches to the preparation of Group II-oxide alloys, hetero- and QW structures by radical-source MBE.

3 Experiment

This Chapter briefly describes the MBE apparatus assembled and used for the fabrication of Group II-oxide epitaxial films, as well as experimental techniques employed for their characterization. Among them are RHEED, low-energy electron diffraction (LEED), HRXRD (Dr. P. Schäfer), STM/AFM, Auger electron spectroscopy (AES), energy dispersive X-ray analysis (EDX, Dr. S. Rogaschewski), transmission electron microscopy (TEM, groups of Prof. D. Gerthsen (Universität Karlsruhe) and Prof. W. Neumann (Humboldt Universität)), electrochemical capacitance-voltage (ECV) profiling, Hall-effect measurements, as well as different optical methods including time-resolved and time integrated PL, PLE and absorption spectroscopy (J. Cui, S. Kalusniak, Y.-H. Fan, and Dr. J. Puls). The basic concepts of these techniques can be found in many textbooks. In what follows only some specific experimental features will be mentioned.

3.1 DCA-450 MBE apparatus for Group II-oxide epitaxy

3.1.1 General

The structures of this study are grown in a commercial DCA-450 MBE apparatus. The DCA-450 system consists of a load-lock module, a buffer-/preparation module and a deposition chamber for molecular beam epitaxy of Group II-oxide materials. Another buffer-/analysis module is added to connect an additional growth chamber (DCA-350) intended for the deposition of organic films in a tandem system. This module is equipped with a combined analyzer for AES and LEED, as well as STM/AFM chamber. The buffer-/preparation module is a multi-purpose UHV chamber equipped with a HT pre-heating stage. The chamber provides facilities for sample preparation and storage and acts as an UHV interface between the load lock and the process chambers (MBE and analysis). A structural scheme of the experimental set up and an overview photograph of the MBE laboratory are presented in Fig. 3.1 and Fig. 3.2, respectively.

3.1.2 Deposition Chamber

The deposition chamber designed for Group II-oxide MBE is an inclined 450 mm internal diameter chamber with wire sealed removable base and top flanges. The chamber has eight ports for effusion cells or other sources. All source ports are symmetrically mounted on a radial array with respect to the chamber axis. Each effusion cell position is provided with a separate port for a linear shutter positioned to interrupt the beam between the source and the substrate. The deposition chamber is equipped with a main shutter, which allows all beams to be interrupted at once. The whole growth area is

3 Experiment

DCA MBE-450

Deposition chamber:

Effusion cells: Zn, Cd, Mg

Plasma cells: O₂ and N₂

RHEED, RGA, infrared pyrometer

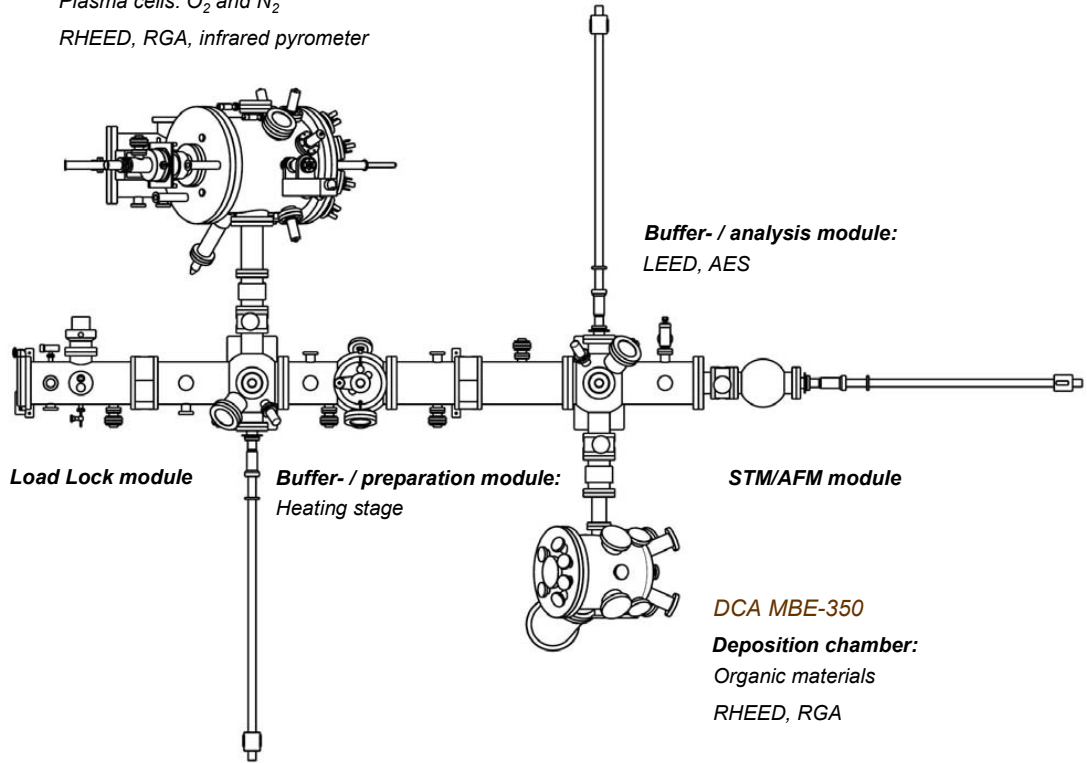


Abbildung 3.1: The structural scheme of the MBE tandem system based on DCA-450 and DCA-350 deposition chambers.

surrounded by two independent cryopanels utilizing a large liquid nitrogen (LN) capacity. At the lower end of the cryopanel the source positions are separated from each other with double wall Mo beam separator plates preventing any thermal and chemical cross-talk between different sources. The deposition chamber pumping system consist of GENESIS ICP 150 cryo-pump with a pumping speed of 1500 ls^{-1} , a VARIAN 500 ls^{-1} ion pump and a Ti sublimation pump with LN-cooled cryopanel of a pumping speed of 3000 ls^{-1} providing a typical residual gas background (BG) pressure in the 10^{-10} Torr range. The growth chamber is equipped with DCA hot-lip effusion cells for evaporation of elemental Zn (6N), Mg (5N), and Cd (6N), as well as rf plasma sources for O₂ and N₂ gases (ADDON). The gas flow rates were normally controlled by a high-precision leak valves. Later it has been switched to a system with mass-flow controllers. The effusion cells and the gas radical sources have an integral water cooling shrouds. Each effusion cell is provided with a linear magnetically coupled electro-pneumatic shutter. The shutter blades are made of Ta and moved outside the vacuum with a pneumatic

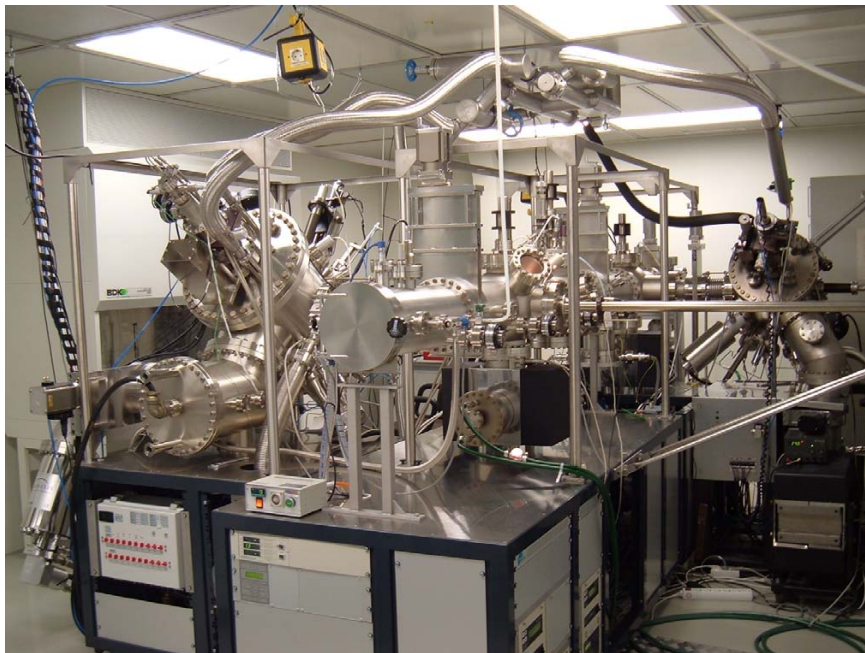


Abbildung 3.2: Overview photograph of the MBE laboratory.

actuator. The substrates are carried on Mo blocks (either In-free or In mounting). DCA MBE systems of the 450 series are basically designed for the 2- or even 3- substrates. In order to couple two deposition chambers in the tandem system and to adapt already existing sample transportation system, the maximal substrate size is reduced to the 1". The substrate temperature is controlled by the thermocouple placed behind the Mo holder and by the infrared pyrometer (IMPAC) sensitive in the temperature range (250-2000) °C. The growth chamber is additionally equipped with a movable nude ionization gauge mounted on a linear bellows assembly and used for measuring the molecular flux intensities¹, RHEED system with a 35 keV differentially pumped RHEED gun (STAIB), and quadrupole residual gas analyzer (RGA) for control of residual gases and leak checking (built by MKS). The growth chamber view-ports, RHEED screen and the pyrometer port are provided with manual view-port shutters. The computer control is LabViewTM based with Windows XP Professional operating system.

3.2 Specific features of oxide MBE

The presence of oxygen and, especially, highly reactive atomic oxygen in the deposition chamber results in the appearance of new specific phenomena intrinsic for oxide MBE in addition to the well known features characteristic for the growth of II-VI materials.

¹Beam equivalent pressure (BEP).

3 Experiment

These include:

- Oxidation of vaporized materials resulting in a gradual change of their flux intensities, especially noticeable when renewed materials are loaded into the crucibles. The substance oxidation is often accompanied by clogging the crucible orifices, particularly essential in the case of Zn effusion cell [see Fig 3.3]. This leads to rather often (compared to the standard MBE) venting the chamber and replacing the vaporized materials. The new generation of effusion cells designed for oxide MBE usually contains a special insert to the crucible reducing the risk of oxidation as well as an additional heating unit with a separate thermocouple installed in the orifice area to prevent material condensation (dual-filament effusion cells).
- Material condensation on the shutter blades and subsequent flake falling (substantial for Zn and Cd) [Fig. 3.4]. This obstacle is partly eliminated by mechanical roughening the Ta shutter blade surfaces or replacing them by the blades made from pyrolytical boron nitride.
- Gradual degradation of the O-plasma cell due to high reactivity of O-radicals. Typical operating time of commercially available rf plasma sources is about one year. After this period the source requires a service where normally a quartz cavity has to be replaced. Such short lifetime leads to a gradual change of the cell parameters resulting in its low stability and a need of frequent calibrations. The characteristics of the rf plasma cell strongly depend on the quality of the cavity and slightly change each time after its replacement.
- The risk of oxidation restricts also a possible range of O-gas flow rates². For this reason the required growth stoichiometry has to be adjusted by changing metal-BEPs, rather than by variation of O₂ flows.

3.3 Substrate preparation

The present work mainly focuses on *a*-plane sapphire substrates³ with typical dimensions of $8 \times 8 \times 1 \text{ mm}^3$ and $10 \times 10 \times 1 \text{ mm}^3$. The choice of the wafer size is caused by convenience to place the sample into the optical cryostat without additional cutting, which is a quite serious problem in the case of sapphire. For some special applications larger wafers are also used. Prior to loading to the deposition chamber, the wafers are degreased consecutively in ultrasonic bath with trichlorethylene, acetone and ethanol for several minutes, rinsed in deionized water and then degassed on the heating stage at 560°C . Finally, the substrates are exposed to the O-plasma for several minutes just before the growth. Usually, the substrates are attached with In or InGa eutectic to Mo

²Depends on pumping system and design of the plasma cell. In our case the maximal gas flow rate was limited by 0.5 sccm, which gave background pressure of pure oxygen of $1.2 \cdot 10^{-5}$ Torr.

³Provided by Crystec GmbH, Germany.



Abbildung 3.3: Oxidized Zn rods taken from the crucibles after being for about 4 months in the deposition chamber.

blank holder, which is the most convenient way for the substrate attachment allowing for the uniform sample heating as well as reliable temperature measurement. The presence of In, however, leads to the unintentional In doping and restricts the maximal growth and annealing temperatures to about 600 °C because the risk of In diffusion into the Mo holder and resultant sample falling. Figure 3.5 illustrates a problem of the unintentional In doping occurring when the substrate is mounted with In. Here, the carrier distribution profile of a typical ZnO epilayer grown with several growth interruptions and annealed at the interfaces is shown. The increase of background electron concentration in the interface regions is clearly seen. The data are taken by ECV profiling at Ferdinand-Braun-Institut für Höchstfrequenztechnik (Berlin).

For the applications where higher temperatures (or layers with lower background carrier concentration) are required, the samples are radiatively heated via a hole in an In-free Mo holder. In order to increase the heat absorption, a 0.8 μm -thick Ti layer is electron-beam deposited on the back side of the substrate. The disadvantage of this technique is that Ti does not stick well on the epipolished sapphire surface. Moreover, the film oxidizes gradually during the growth becoming partly transparent for the infrared pyrometer and making stability of the temperature control very difficult.

3.4 Characterization tools

3.4.1 *In-situ* diagnostic

RHEED

In situ characterization tools that shed light on structural and compositional properties of films in real time during growth are invaluable. These aid the researcher in knowing

3 Experiment

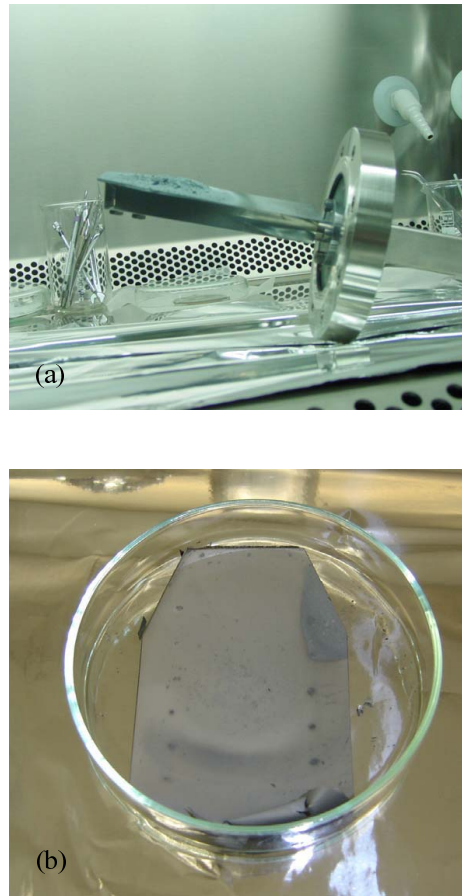


Abbildung 3.4: Zn condensation on a shutter blade: (a) The shutter surface; (b) Material, released from the shutter.

to first-order whether the desired film properties are being achieved without having to depend on post-growth analysis. In MBE, reflection high-energy electron diffraction has been widely used to monitor surface crystallographic and morphological properties. In RHEED, a beam of high-energy electrons (≥ 10 keV) is incident on the substrate/film surface at a small angle ($\leq 3^\circ$). The diffracted intensity pattern can be easily converted to visible light by a phosphor screen. Since the probe electrons enter and exit the surface region at a glancing angle, the surface symmetry and morphology can be monitored dynamically during growth.

Compared to other diffraction methods, the glancing incidence angle geometry of RHEED offers many advantages, such as high surface sensitivity and *in-situ* compatibility with crystal growth. At the same time, however, glancing incidence requires special adaptations of experimental methods and theoretical models to take into account the symmetry breaking introduced by the reflection geometry. Two types of diffraction

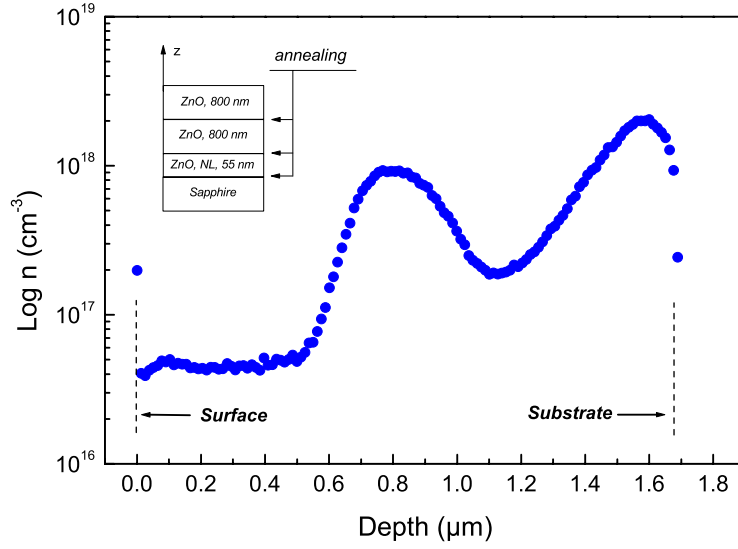


Abbildung 3.5: Carrier concentration profile of a typical ZnO film grown with several growth interruptions and annealing steps at each interface ($T_a = 560^\circ\text{C}$). The sapphire substrate is mounted with In.

contribute to a RHEED pattern. The main contribution is given by incident electrons which underwent single, elastic scattering events at the crystal surface. This is so called kinematic scattering. Dynamic scattering occurs when electrons undergo multiple diffraction events in the crystal and lose some of their energy due to interactions with the sample. In the kinematical scattering theory, the possible reflections are determined by the condition that the wavevectors \mathbf{k}_0 and \mathbf{k}' of the incident and diffracted beams differ by a reciprocal lattice vector \mathbf{G} :

$$\mathbf{k}' - \mathbf{k}_0 = \mathbf{G}. \quad (3.1)$$

When considering only elastic scattering events, which means that $|\mathbf{k}'| = |\mathbf{k}_0|$, this diffraction condition can be cast into the geometrical construction of the Ewald sphere in reciprocal space. In this construction, the tip of \mathbf{k}_0 is attached to a reciprocal-lattice point. The sphere around the origin of \mathbf{k}_0 with radius $|\mathbf{k}_0|$ then defines the Ewald sphere [Fig. 3.6(a)]. Reflections can occur for all \mathbf{k}' connecting the origin of the sphere and a reciprocal-lattice point on the sphere. The magnitude of the wavevector for high-energy electrons is given by:

$$k_0 = \frac{1}{\hbar} \sqrt{2m_0E + (E/c)^2}. \quad (3.2)$$

The relativistic correction amounts to about 3 % for 20 keV electrons. For a qualitative analysis, it is therefore often sufficient to use the nonrelativistic approximation.

3 Experiment

In RHEED the radius of the Ewald sphere is much larger than the spacing between reciprocal lattice rods. This means that it produces an almost planar cut through the first few Brillouin zones of the reciprocal lattice. This large radius of the Ewald sphere combined with the small scattering angles facilitates the geometrical interpretation of RHEED patterns, since for many purposes angular distortions can be neglected and the usual small-angle approximations for the trigonometric functions are valid.

The high surface sensitivity of RHEED implies that the periodic part of the crystal beneath the surface can usually be neglected. In the construction of the reciprocal lattice one can therefore often approximate the sampled volume by a 2D layer. The reciprocal lattice then degenerates into a set of one-dimensional rods along the z direction perpendicular to the surface. Using this reciprocal lattice, one gets the Ewald sphere construction used in RHEED that is shown in Fig. 3.6 [Bra99]. Since the reciprocal lattice consists of continuous rods, every rod produces a reflection in the diffraction pattern. The reflections occur on so-called Laue circles of radius L_n centered at H , the projection of the component parallel to the surface of \mathbf{k}_0 onto the screen. The specular reflection or specular spot S is located at the intersection of the zeroth-order Laue circle with the (00) rod. The origin of the reciprocal lattice is projected onto I , also labelled (000), where for some sample geometries the part of the incident beam that misses the sample becomes visible. Owing to the simple geometry of RHEED, the reciprocal lattice rod separations g_{\parallel} and g_{\perp} parallel and perpendicular to the beam direction can be easily determined:

$$ng_{\parallel} = k_0 \left[\cos\theta - \frac{1}{\sqrt{(L_n/L)^2 + 1}} \right], \quad (3.3)$$

where ng_{\parallel} is measured from the row containing the (00) rod, and

$$ng_{\perp} = \frac{k_0}{\sqrt{(L/nl)^2 + 1}}, \quad (3.4)$$

which for small angles ($nl \ll L$) can be approximated by

$$ng_{\perp} = \frac{nl}{L} k_0. \quad (3.5)$$

Again, ng_{\perp} is measured from the central rod. The reciprocal-lattice rods are indexed in a way similar to the bulk reflections. The nomenclature is based on the 2D surface lattice, using two indices similarly to the 3D case. The surface lattice vectors generally differ from the bulk lattice vectors so that there is no direct correspondence to the Miller indices of the bulk material. If a surface reconstruction is present that produces a superperiod, fractional indices are used to label the superlattice reflections. The center of the reciprocal lattice I , which lies on the zeroth Laue circle by definition, is labeled (000). All angles, however, are measured from the symmetry axis of the zeroth Laue cone $O-H$ [Bra99].

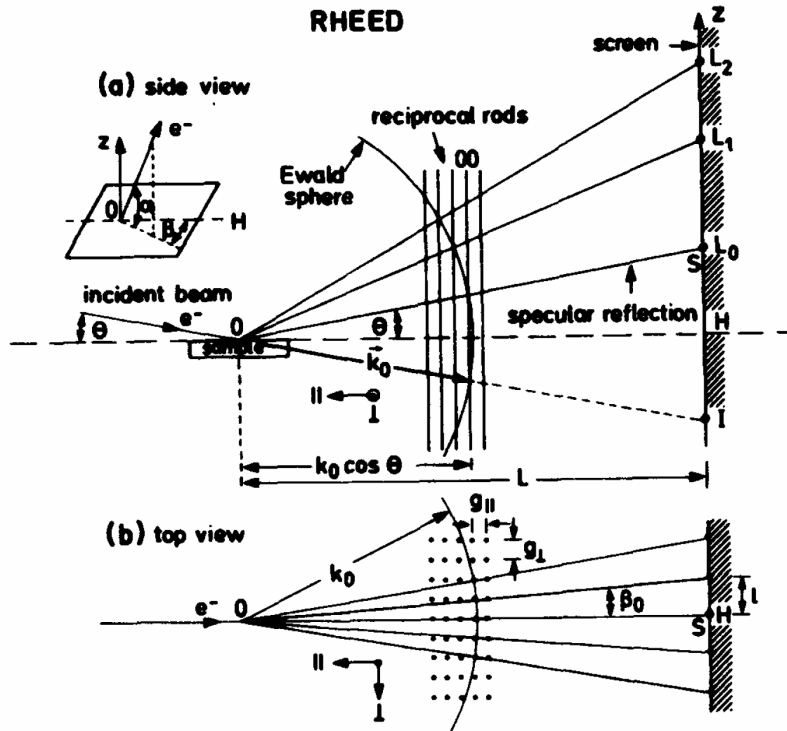


Abbildung 3.6: Ewald sphere construction and diffraction geometry of RHEED. Intensity maxima on the screen correspond to projected intersections of the Ewald sphere with the reciprocal lattice. (From [Bra99]).

Typical RHEED patterns of ideal and real surfaces

In ideal case, coherent diffraction from the surface over a length scale comparable to the electron coherence length, which is typically $\sim 1000 \text{ \AA}$ for a well-collimated beam, gives rise to semicircular zones of scattered beams that are easily seen on a phosphor screen. These beams consist of spots for a crystalline surface with terrace widths greater than or equal to the electron coherence length, as shown in Fig. 3.7(a) [Cha00]. What is seen here are diffracted beams within the zeroth-order Laue zone of $\alpha\text{-Al}_2\text{O}_3(0001)$. The spacing between spots is inversely proportional to $|\mathbf{b}|$, the in-plane lattice parameter perpendicular to the beam. Also seen, but not shown in Fig. 3.7(a), are other semicircular spot patterns at higher radii. These are the higher-order Laue zones, and the spacings between beams of comparable Miller indices in, for instance, the zeroth- and first-order Laue zones are inversely proportional to $|\mathbf{a}|$, the in-plane lattice parameter parallel to the beam.

If, due to growth dynamics or the condition of the substrate surface, the mean terrace width is somewhat smaller than the electron coherence length, the spots within a given Laue zone become streaks, as seen in Fig. 3.7(b) for epitaxial Fe_3O_4 grown

3 Experiment

on MgO (001). The RHEED pattern is still dominated by reflection. However, the reduction in terrace width results in spreading out of beams along the incident direction resulting in the evolution of streaks. Such "streaky" pattern is typical for smooth surfaces of real crystals. Finally, if the surface consists of islands of such an aspect ratio that the primary electron beam is readily transmitted through the islands without excessive inelastic attenuation, the diffraction pattern is dominated by transmission through the islands, rather than reflection from the island surfaces. An example of this phenomenon is shown in Fig. 3.7(c) for a polished MgO (001) substrate covered by MgO islands [Cha00].

RHEED oscillations

Lets us consider an atomically smooth surface containing a system of elementary steps. The periodic nucleation and growth phenomena provide a periodic change in the surface roughness, as shown in Fig. 3.8(e) [Hur94]. Therefore, the glancing incidence electron beams reflected and diffracted from the growing interface also change in intensity periodically. The higher the surface roughness is, the more electrons are scattered incoherently, and the lower are the intensities of the registered coherently scattered beams. This corresponds to the lower curve in Fig. 3.8(e). The described RHEED oscillations were first discovered on MBE-grown GaAs (100). After several oscillations of gradually decreasing amplitude [see Fig. 3.8(e)] reflected beam intensities remaining constant in time have been observed [Hur94]. The oscillation damping can be easily explained by desynchronization of nucleation events that are random in time and within the area of observation. As a matter of fact, the nuclei of the next layers may appear before the previous layer is completed [Fig. 3.8(c)]. This delay is also different in various places of the growing surface. Finally, the surface "forgets- its initial regular structure and the roughness averaged over the observed surface does not vary in time any more. After growth interruption or annealing of the surface by keeping it under equilibrium conditions, the roughness disappears and the oscillations may be observed again [Hur94]. It is important to note that the beam interruption does not increase the surface mobilities, but excludes the creation of new nuclei, thus supporting synchronization. The RHEED oscillations are very important technologically because they permit one to count directly the number of deposited monolayers and to complete heterointerface at the stage when the surface roughness is minimal (i.e. the RHEED intensity is maximal), thus producing the smoothest interfaces in the heterostructure. In the growth of complex structures, like MQWs, the shutter control is usually automated by using the phase of the RHEED oscillations [SFO⁺84, HGH⁺95].

3.4.2 *Ex-situ* diagnostics

HRXRD

High-resolution X-ray diffraction measurements providing direct information about crystal quality, symmetry and lattice constants are systematically used for characteri-

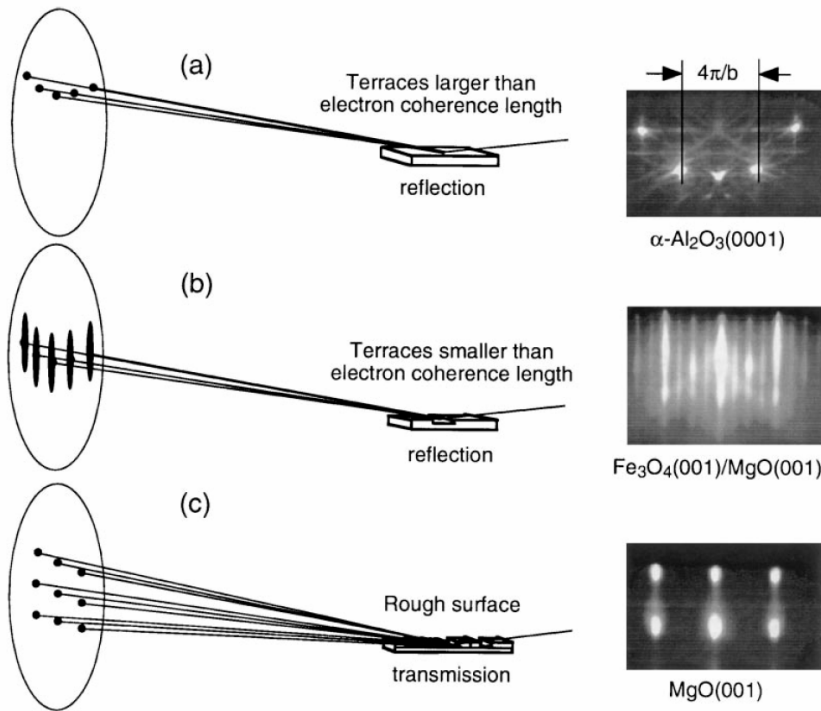


Abbildung 3.7: Schematic diagram of RHEED for surfaces with: (a) terrace widths that are larger than the electron beam coherence length; (b) terrace widths that are comparable to the electron beam coherence length; (c) islands of such an aspect ratio that significant transmission occurs through the islands. (From [Cha00]).

zation of the grown structures. The measurements are performed with $\text{Cu } K\alpha_1$ radiation using a Philips X'Pert MRD diffractometer equipped with a four-crystal Ge (220) monochromator and a channelling Ge (220) three-reflection analyzer as detection unit. Normally, the epitaxial films are characterized by taking ω and $\omega-2\theta$ scans of the symmetrical (0002) reflection. In some special cases, also more complicated XRD measurements including reciprocal space mapping for the symmetrical (0002) and asymmetrical ($11\bar{2}4$) reflections are carried out.

EDX

The composition of the ZnCdO and ZnMgO alloy films is determined by energy-dispersive X-ray analysis. The measurements are performed on Leica Cambridge Ltd S360 scanning electron microscope equipped with a EDX unit from Röntec GmbH. Characteristic X-ray radiation is excited by the primary electron beam with energy of 20 keV. The signal is integrated over the scanning area of $10 \times 10 \mu\text{m}^2$.

3 Experiment

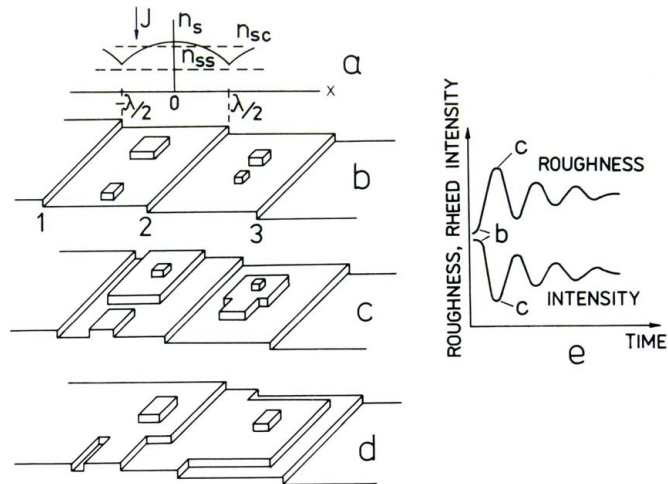


Abbildung 3.8: Subsequent temporal stages (b-d) of a periodic nucleation and growth process on a vicinal surface formed by the steps 1, 2, 3. (a) The concentration n_s of the adsorbed species on a terrace; (e) the upper curve presents the surface roughness (the total step perimeter per unit area), the lower curve gives the electron beam intensity coherently scattered from the interface. (From [Hur94]).

AES

AES is a widely used analytical tool for obtaining the qualitative and quantitative information about chemical composition of solid surfaces. The AES data presented in this work are collected by combined OMICRON LEED/AES system connected via UHV buffer line with the growth chamber. The AES unit consists of a semispherical energy analyzer and an electron gun with maximal primary electron energy of 3 keV. While the AES systems for quantitative analysis are normally equipped with a cylindrical mirror analyzer providing better sensitivity and require external standards, the described system is successfully used for qualitative estimate the surface chemical composition during pregrowth substrate preparation and the fabrication of ternary alloy films.

AFM

The surface morphology images were recorded by Nanoscope Digital (Digital Instruments) AFM operating in tapping mode. Several pictures have been also taken by a UHV version of OMICRON AFM without any exposure of the sample to air.

TEM

Cross-section TEM measurements are performed at 200 kV accelerating voltage using field-emission gun microscopes of the type Philips CM 200 FEG/ST and CM 20 FEG

where the latter is equipped with a unit for scanning transmission electron microscopy (STEM) operation. Cross-section TEM specimens are prepared by cutting thin slices, gluing them face to face, grinding, polishing, dimpling down to a thickness of about 10 μm , and finally ion thinning until electron transparency.

Hall-effect measurements

The Hall-effect is a powerful and simple tool for electrical characterization of semiconductors allowing for the simultaneous measurements of carrier concentration and their mobility. In this study, room-temperature and temperature-dependent Hall-effect measurements are performed using the van der Pauw geometry in a magnetic field of 0.5 T (Prof. W. Ted Masselink group). Data are compiled employing both positive and negative currents and magnetic fields, and the results are averaged in order to compensate for various electromagnetic effects.

The van der Pauw configuration is originally developed for uniform samples. Epitaxial ZnO films, however, are often nonuniform. In the case of ZnO grown on sapphire, a highly conductive usually degenerate layer exists at the ZnO/sapphire interface. This layer causes a channel of the parallel conductance, which strongly affects the results of the measurements especially at low temperatures, where the classical carrier freezing is expected [TYF⁺04]. In order to recalculate the carrier concentration (n_{H1}) and the Hall mobility (μ_{H1}) of the bulk layer from the measured "device-values" (n_H) and (μ_H) a two-layer model has been introduced by D. Look *et al.* for similar GaN/sapphire system [LM97]. According to this model, the carrier concentration and the Hall mobility of the bulk layer can be found from the equations:

$$\mu_H = \frac{\mu_{H1}^2 n_{H1} + \mu_{H2}^2 n_{Hs2} / d_1}{\mu_{H1} n_{H1} + \mu_{H2} n_{Hs2} / d_1}, \quad (3.6)$$

$$n_H = \frac{(\mu_{H1} n_{H1} + \mu_{H2} n_{Hs2} / d_1)^2}{\mu_{H1}^2 n_{H1} + \mu_{H2}^2 n_{Hs2} / d_1}, \quad (3.7)$$

where n_{Hs2} , μ_{H2} are the Hall carrier concentration and the Hall mobility of the interface layer, respectively, d_1 is the thickness of the bulk layer.

These expressions show that the interpretation of the Hall data for ZnO/sapphire system is a rather complicated task requiring at least precise knowledge of electrical properties of the interface layer. The applicability of the two-layer model obviously requires an abrupt interface between two layers which is not always the case for ZnO films.

Besides the multilayer problem discussed previously, ZnO films grown on sapphire

3 Experiment

often show an additional conductive channel along the substrate edges. This parallel conductivity is found both, for In and In-free mounted crystals. In order to avoid this effect, the ZnO epitaxial films are processed before Hall-effect measurements. The processing includes photolithography, wet chemical etching, metallization (In or Ni/Au) and lift-off processes. Typical ZnO structures prepared for Hall-effect measurements are shown in Fig. 3.9.

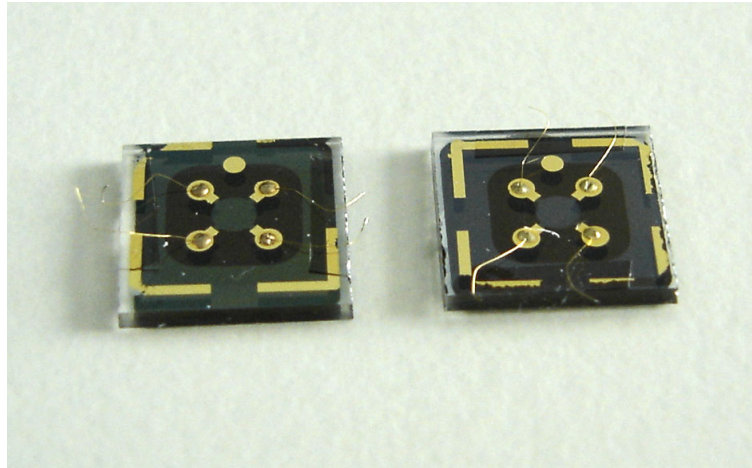


Abbildung 3.9: Specific example of ZnO epilayers prepared for Hall-effect measurements.

Electrochemical C-V profiling

Electrical characterization of ZnO films is normally carried out by Hall-effect measurements. ECV profiling is an alternative characterization technique that has been used extensively on III-V semiconductors such as GaAs and InP and II-VI materials such as ZnSe. It has the advantage over Hall measurements in that it can determine the uniformity of doping over the thickness of the layer and characterize multilayers with multiple doping levels, including p-n junctions. ECV profiling employs electrochemical etching to determine the electrical carrier concentration as a function of depth in compound semiconductors. By making use of a well-defined electrochemical dissolution reaction, the semiconductor can be profiled to any depth at a controlled rate. The semiconductor/electrolyte interface behaves as a Schottky diode across which C-V measurements are performed. By using the electrolyte to both etch and form a Schottky contact with the semiconductor, one can obtain the depth profile of the carrier concentration in the semiconductor. The ECV profiling of this study is carried out on PN 4400 BioRad (Accent Optical Technologies)/ECV profiler for wide-gap materials. 0.1 M ZnCl_2 water solution is used as an electrolyte [TCC⁺04].

4 Growth of ZnMgO alloys and ZnO/ZnMgO quantum well structures

4.1 Introduction

When this work had been initiated, radical-source MBE was already widely employed for the growth of ZnO thin films (see Chapter 2). At that time, however, ZnMgO alloys and ZnO/ZnMgO heterostructures had been mainly prepared by PLD and metal-organic epitaxial methods. In this Chapter, one of the first growth recipes for the fabrication of ZnMgO by MBE is demonstrated. The presented results confirm that this growth technique represents indeed a systematic approach to the preparation of the high-quality ternary alloys and ZnO/ZnMgO quantum well structures using easily available sapphire substrates.

4.2 ZnMgO ternary alloy films

4.2.1 Two-step growth procedure: ZnMgO nucleation layer

By analogy with a recipe suggested for the deposition of ZnO films [NTT⁺01], a two-step growth procedure is utilized for the fabrication of ZnMgO alloys. First, an about 35 nm-thick ZnMgO nucleation layer is deposited at $T_g = 300^\circ\text{C}$ directly on *a*-plane sapphire substrate after it is degassed and exposed to O-plasma. Unlike previous MBE studies [CKH⁺00, KHN⁺04], no buffer layer is introduced. It is found that the use of a ZnO buffer is not essential for the fabrication of wurtzite ZnMgO alloys and the buffer can be waived. Additional spectral features appearing in PL spectra of ZnO/ZnMgO QW structures can thus be avoided and optical transmittance measurements becomes possible. Only in the case of alloys with very high Mg contents ($x \geq 0.35$) about 1 nm-thick ZnO layer is introduced to prevent a direct crosstalk between Mg and sapphire and to force ZnMgO to grow in a strict wurtzite phase. A sequence of the RHEED patterns taken during deposition of a ZnMgO NL is shown on Fig. 4.1. When the deposition starts, a sharp streaky pattern of the substrate [Fig. 4.1(a)] practically disappears in the diffuse background indicating formation of a very thin ZnMgO amorphous layer [Fig. 4.1(b)]. Continuing deposition leads to the appearance of ZnMgO wurtzite reflexes, which are initially rather weak and broad signifying strong crystalline disorder expected from the different planar symmetry of the film and the substrate [Fig. 4.1(c, d)]. With increasing the layer thickness, the reflexes gradually become brighter and sharper. The RHEED pattern is still streaky, however, one can already see the formation of V-notch features signifying surface faceting [Fig. 4.1(e)]. Substantial narrowing of

4 Growth of ZnMgO alloys and ZnO/ZnMgO quantum well structures

the reflexes occurs when the film thickness reaches a value of about 20 nm. After that, only a slight narrowing of the diffraction features can be observed, indicating that the main film reorganization processes have already happened. The RHEED pattern of a typical ZnMgO NL with a thickness of about 35 nm is shown in Fig. 4.1(f). Annealing at $T_a = 560$ °C for several minutes improves the surface morphology and completes the formation of the NL.

The influence of annealing on extremely thin epitaxial films nucleated at very LT is threefold. Annealing induces recrystallization of the film reducing the spread of its mosaic structure. It enforces also interaction between TDs leading to their partial annihilation. Finally, it improves the surface smoothness by reducing the step meandering and increasing the average distance between neighboring 2D nuclei as a result of their coalescence due to enhanced surface mobility at elevated temperatures and synchronization of the nucleation events forced by the growth interruption. Through the above described nucleation step, perturbations from the sapphire-ZnMgO interface are partially healed and the deposition of a "bulk"(typically 500-700 nm-thick) ZnMgO layer can be initiated. The bulk ZnMgO layer is typically grown on such template at slightly higher temperature. Both deposition processes are carried out under metal-rich conditions. Change of the growth stoichiometry in this temperature range normally leads to a fast and irreversible surface roughening most likely due to the considerably lower mobility of Zn and Mg adatoms on the O-polar surfaces under excess of oxygen [CKH⁺02].

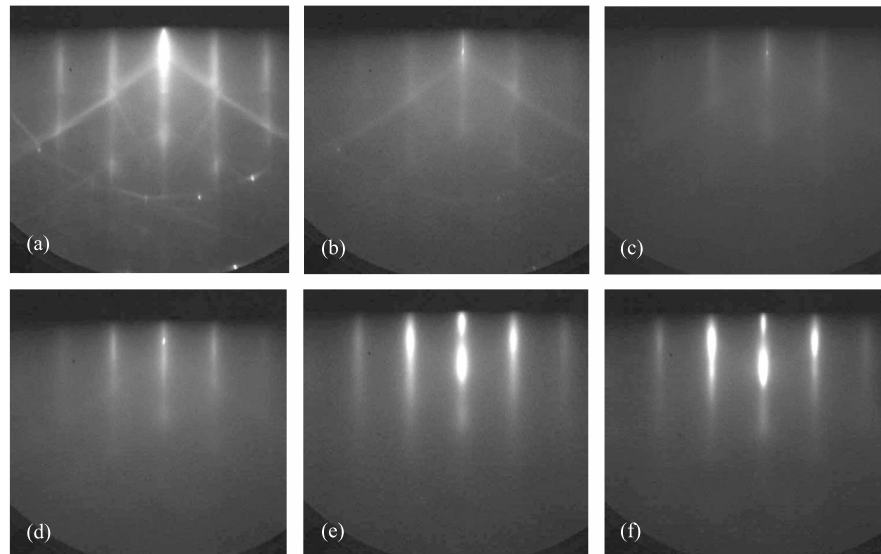


Abbildung 4.1: Evolution of RHEED patterns along the $\langle 11\bar{2}0 \rangle$ azimuth taken during the growth of a LT ZnMgO nucleation layer. (a) $(11\bar{2}0)$ sapphire substrate; (b) ZnMgO - 1 nm-thick; (c) ZnMgO - 2 nm-thick; (d) ZnMgO - 5 nm-thick; (e) ZnMgO - 20 nm-thick; (f) ZnMgO - 35 nm-thick.

4.2.2 Influence of the growth temperature

The fabrication of ZnMgO alloys is very sensitive to the growth temperature [SBC⁺05]. At $T_g > 500$ °C, even for low Mg contents, a strong tendency to polycrystallization is observed. This is manifested by the immediate appearance of Debye rings in the RHEED pattern. Fig. 4.2(a) shows this for a 60 nm-thick ZnMgO layer grown on top of a ZnO buffer at 520 °C. While the rings are initially superimposed to a streaky background, the pattern becomes fully polycrystalline with increasing growth time. At intermediate temperature¹, the polycrystalline rings are absent. Instead, V-notch features in the RHEED pattern signify the formation of surface facets. Continuing growth, the overall brightness of the RHEED pattern decays strongly, indicating poor crystal perfection and development of a rough surface morphology. Similar RHEED patterns have been also reported by C. Morhain *et al.* [MTTD⁺05] for the ZnMgO films, grown on (0001) sapphire substrates (Fig. 2.11). Much better results are obtained in the temperature range $T_g = (310 - 370)$ °C. Here, the RHEED pattern consists also of facet features as well as a streaky background. However, the pattern stays entirely stable during the whole growth, as it is shown in Fig. 4.2(b) for a 700 nm-thick layer. A striking finding is that the surface morphology of the as-grown ZnMgO layer can be dramatically improved by short-time annealing at intermediate temperatures. Annealing for about 5 min at $T_a = (540 - 600)$ °C is sufficient to remove the V-notches completely and to obtain a streaky RHEED pattern with very sharp and narrow reflexes [Fig. 4.2(c)]. Moreover, during cooling down to the growth temperature, bright (3×3) reconstruction features together with Kikuchi lines reproducibly appear, indicating a well-defined structure of the sample surface. This is very important for the fabrication of ZnO/ZnMgO QW structures, where any uncontrollable fluctuations of the surface roughness at the interface region are expected to introduce additional exciton localization in view of a very small exciton Bohr radius of ZnO. The influence of annealing on the surface morphology is further investigated by AFM. The data show that the surface of the as grown ZnMgO layer is covered by small islands with lateral dimensions in the few 10-nm range and a height of (1-2) nm [Fig. 4.3(a, b)], whose side facets cause the V-notch features detected by RHEED [Fig. 4.2(b)]. On the other hand, the annealed surface is atomically smooth with steps corresponding to the *c*-axis length of ZnMgO [Fig. 4.3(c, d)]. The typical surface roughness estimated from the AFM images for annealed samples over a size of 1 μm^2 is below 0.3 nm, which is one of the best values reported so far for the ZnMgO epitaxial films.

4.2.3 ZnMgO alloys: Band gap and lattice constant vs. Mg content

Figure 4.4 summarizes data for roughly 600-nm thick ZnMgO epilayers grown at $T_g = 360$ °C. As it is seen in Fig. 4.4(a), the Mg content of the layers can be systematically tuned by changing the Mg/Zn BPR. In the whole composition range covered by Fig. 4.4(a), XRD exhibits only wurtzite reflexes from ZnMgO. The *c*-lattice constant [Fig. 4.4(b)] is in good approximation a linear function of the Mg content with a minimum

¹ $T_g = (400 - 460)$ °C

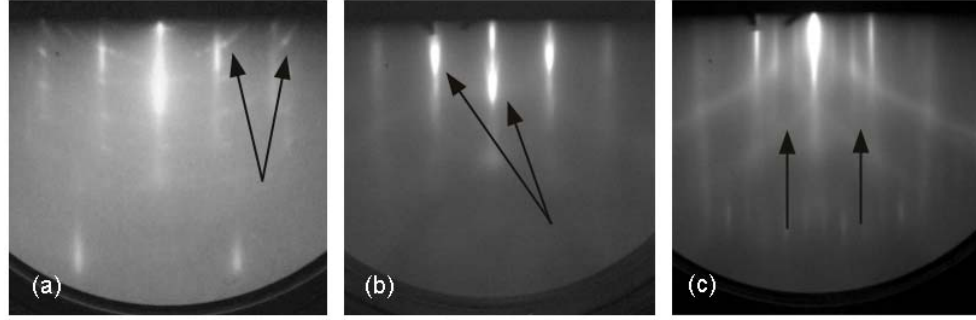


Abbildung 4.2: RHEED patterns taken along $\langle 11\bar{2}0 \rangle$ azimuth for ZnMgO epilayers ($x = 0.08 - 0.12$) grown at different temperatures: (a) $T_g = 520$ °C, 60 nm-thick, arrows indicate polycrystalline rings; (b) $T_g = 360$ °C, 700 nm-thick, arrows indicate facet features; (c) same as (b), but after annealing at 600 °C, arrows indicate (3×3) reconstruction.

value of $c = 5.136$ Å reached at $x = 0.40$. The full widths at half maximum of the rocking curves taken from ω - 2θ scan of (0002) reflection is 977 arc sec at $x = 0.40$, indicating still satisfactory crystal quality. Note, that the FWHM of 977 arc sec is only by factor of 1.6 larger than the same value of ZnO epilayers with comparable thickness grown on a -plane sapphire, where the main contribution to the width of the XRD rocking curves comes from the highly disturbed nucleation layer. The FWHM of (0002) reflection decreases orderly with increasing layer thickness and reaches a value of about 300 arc sec for 1 μ m-thick films. At higher Mg contents $x > 0.40$, phase separation signified by the emergence of MgO reflexes in XRD sets on. The RT band edge of the epilayers undergoes a prominent high-energy shift arriving at $E_g = 4.4$ eV for $x = 0.40$. The values in Fig. 4.4(c) were extracted from transmittance spectra by using $\alpha(\omega) = \alpha_0 \text{sech}[(E_g - \hbar\omega)/\Gamma]$ for the absorption coefficient. This expression produces the low-energy Urbach tail as well as a maximum at E_g . The accuracy of the band-gap determined in this way is in the order of the exciton binding energy. The alloy broadening increases from $\Gamma = 35$ meV ($x = 0.085$) to $\Gamma = 86$ meV ($x = 0.40$). For $x > 0.40$, the band-gap shift stops, verifying again onset of phase separation.

4.2.4 Structural properties

Figure 4.5 shows TEM cross-section overview images of a typical ZnMgO epilayer grown by this technique, where the same sample region is imaged under different conditions. Figure 4.5(a) is a bright-field image taken with imaging vector $\mathbf{g}_{\text{ZnMgO}} = [0002]$. Figure 4.5(b) is recorded under $(g, 3g)$ weak-beam conditions with $\mathbf{g}_{\text{ZnMgO}} = [1\bar{1}00]$. The speckle contrast which is visible in Fig. 4.5(a) can be attributed to preparation-induced defects close to the surface of the TEM sample. The dark contrast at the substrate/film interface [Fig. 4.5(a)] results from a particularly high density of planar defects in the thin NL which is in a good agreement with the RHEED data. The threading dislocations in

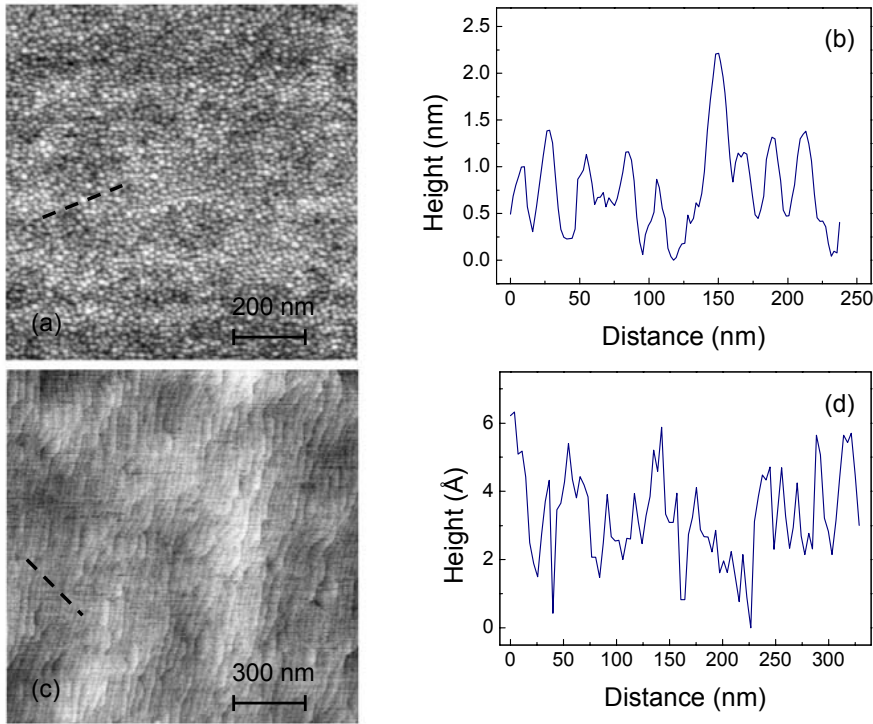


Abbildung 4.3: AFM topography images of a $\text{Zn}_{0.88}\text{Mg}_{0.12}\text{O}$ epilayers grown at $T_g = 360^\circ\text{C}$: (a) As-grown, the scan size is $1.0 \times 1.0 \mu\text{m}^2$; (b) AFM height profile taken along the dashed line in (a); (c) Annealed at 560°C , the scan size is $1.5 \times 1.5 \mu\text{m}^2$; (d) AFM height profile taken along the dashed line in (c).

Fig. 4.5(a) are screw and mixed dislocations, whereas contrast extinction occurs for edge dislocations with a Burgers vector perpendicular to $\mathbf{g}_{\text{ZnMgO}} = [0002]$. Fig. 4.5(b) shows mixed and edge dislocations in the same sample region. All TDs are preferentially aligned along the $[0001]$ direction. According to Fig. 4.5, the majority of long TDs are edge dislocations. The significantly lower density of screw and mixed TDs can be attributed to the preferential annihilation of these dislocations in the lower part of the ZnMgO layer. Several dislocation loops are marked by arrows in Fig. 4.5(a). Single dislocation segments which appear to end inside the layer result from the penetration of these dislocations through the TEM sample surface. The observed relation between the densities of screw, mixed, and edge dislocations is different compared to TEM data reported for ZnO grown on a -plane sapphire where most of the TDs found are of screw or mixed type [LSKN01]. It is, however, similar to ZnO grown on c -plane sapphire where mostly edge dislocations occur [VVV⁺01, SVC⁺04]. The TDs are mainly threading segments of misfit dislocations located at the ZnMgO/ Al_2O_3 interface. Some dislocations appear to be generated in the NL as also observed for GaN grown on sapphire [NPC⁺06].

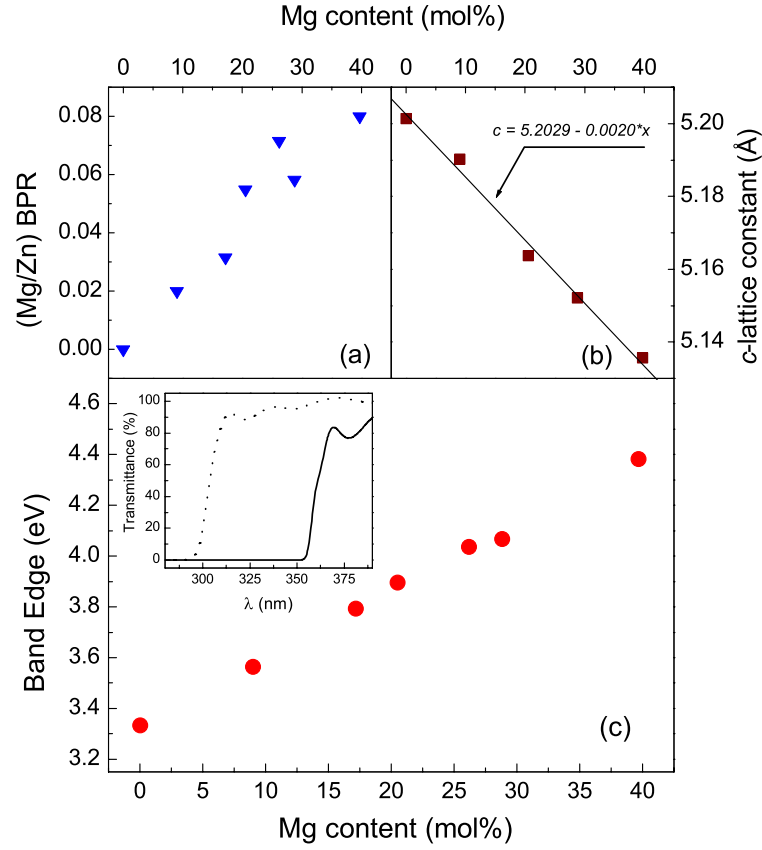


Abbildung 4.4: ZnMgO epilayers grown at $T_g = 360^\circ\text{C}$. The layer thickness is about 700 nm. (a) BPR, (b) c -lattice constant, and (c) room temperature band-gap versus Mg content. Inset: optical transmittance spectra for $x = 0.10$ (full) and 0.40 (dashed).

Selected-area electron diffraction shows that the (0001) plane of ZnMgO is oriented parallel to the $\text{Al}_2\text{O}_3(11\bar{2}0)$ substrate surface with an azimuthal alignment $[0001]_{\text{sapphire}} \parallel [11\bar{2}0]_{\text{ZnMgO}}$. This quasi-epitaxial relationship is in agreement with previous results [FIY⁺00, OKT⁺03]. The estimated total density of TDs close to the surface is $2.5 \times 10^{10} \text{ cm}^{-2}$ as compared to $1.9 \times 10^{10} \text{ cm}^{-2}$ and $2.7 \times 10^9 \text{ cm}^{-2}$ - $4 \times 10^{10} \text{ cm}^{-2}$ found in ZnO grown on a -plane and c -plane sapphire, respectively [LSKN01, VVV⁺01, SVC⁺04]. For GaN grown on sapphire it was reported that the dislocation density does not critically depend on the orientation of the sapphire substrate (0001) versus (11 $\bar{2}0$) [LE02] but rather on the quality of the low-temperature nucleation layer. The situation appears to be quite similar for ZnO, therefore attention has to be paid to the improvement of the NL. According to the TEM data, the minimal thickness of the ZnMgO buffer required to minimize the total dislocation density in the top part of the structure is about 400 nm.

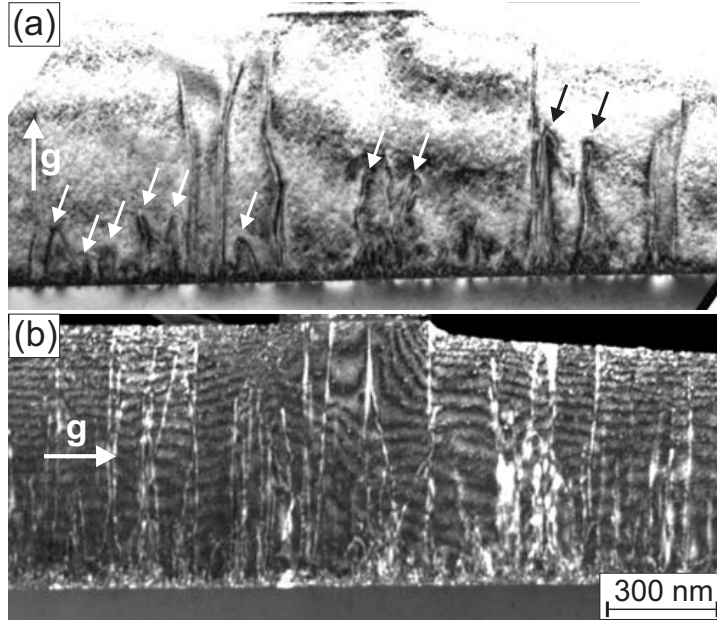


Abbildung 4.5: TEM of ZnMgO films grown on sapphire. Cross-section images from the same sample region taken (a) under bright-field conditions with an imaging vector $\mathbf{g} = [0002]$, and (b) taken under $(\mathbf{g}, 3\mathbf{g})$ weak-beam conditions with $\mathbf{g} = [1\bar{1}00]$. (R. Schneider, D. Litvinov and D. Gerthsen, Universität Karlsruhe).

4.3 ZnO/ZnMgO quantum well structures

The annealing step described above can be successfully carried out at any stage of the ZnMgO deposition. Subsequently, layer-by-layer growth occurs as documented by the observation of distinct RHEED specular beam intensity oscillations, facilitating the fabrication of ZnO/ZnMgO QW structures in a well-controlled growth mode. The standard growth scheme applied for the fabrication of single QW structures is shown in Fig. 4.6(a). According to this scheme, a ZnO QW layer is sandwiched between a 600 nm-thick ZnMgO buffer and typically a 30 nm-thick ZnMgO cap layer, having the same Mg content. The deposition temperature of the ZnO layer can be varied in the range of $T_g = (300 - 470)^\circ\text{C}$ maintaining the layer-by-layer growth. Within this range, lower temperatures lead to larger oscillation amplitude due to the smaller size and higher density of 2D nuclei, making control of the well width more accurate. At $T_g > 470^\circ\text{C}$, the growth is mainly governed by a step-flow mode and RHEED oscillations disappear. Figure 4.6(b) shows a specific example of RHEED oscillations recorded at each interface during the preparation of a 4 nm-thick ZnO QW structure embedded in $\text{Zn}_{0.69}\text{Mg}_{0.21}\text{O}$ barriers. More than 15 oscillations are observed before the amplitude is damped below 1/5 level, probably caused by the renewed formation of facets on the growing surface and desynchronization of nucleation events. However, the oscillations are immediately

recovered performing the annealing step. In the case of typically (2 - 6) nm-thick ZnO QW layers annealing for 3 min at $T_a = 520^\circ\text{C}$ is sufficient to recover the surface smoothness. The presence of RHEED oscillations at both stages of the QW growth is indicative of high-quality, atomically smooth interfaces. This is indeed confirmed by the TEM data presented in Fig 4.7.

PL spectra of the SQW structures fabricated by using this procedure are summarized in Fig. 4.8. For wider wells and lower Mg content [Fig. 4.8(a)], the low-temperature width of the QW emission is as small as 7 meV. High-energy shifts of the PL features occurring for smaller well widths [Fig. 4.8(b)] signify clear quantum-size effects. The line broadening results from the stronger influence of the interfaces. Similarly prominent QW emission is also observed for structures with Mg contents up to $x = 0.40$ [Fig. 4.8(c)], but the bandwidth is here in the some-10 meV range. The line-shape of both QW and barrier PL exhibits a marked low-energy tail revealing exciton localization. The broader bandwidth of the barrier emission, suggesting larger localization energies, is consistent with its ternary character. Distinct QW emission is also found at room temperature [Fig. 4.8(d)]. The yield is more than one order of magnitude larger than for ZnO epilayers under comparable excitation conditions.

4.4 ZnO/ZnMgO MQWs: Structural and optical properties

The similar growth recipe can be adapted for fabrication of the MQW structures. Figure 4.9 shows a scanning TEM bright-field image of the ZnO/ZnMgO five period MQW structure recorded by means of an electron probe of approximately 1 nm in diameter. Due to the convergence of the incident beam diffraction-contrast contributions are minimized. Thus, the MQW layers can be clearly recognized, whereas dislocations show only weak contrast. The inset to Fig. 4.9 gives a higher-magnified view of the active region where the ZnO layers appear dark in contrast to the adjacent ZnMgO regions. The ZnO layers are continuous and form abrupt, atomically flat interfaces with the ZnMgO barriers. The well width as determined by the RHEED oscillations is $d_W = 2.8$ nm. The width deduced from TEM agrees well with that value ruling out intermixing at the ZnO/ZnMgO interfaces due to the introduction of the annealing steps.

Figure 4.10 summarizes the PL data of the MQW structures. The spectra given in the upper part are dominated by prominent peaks from MQW excitons. The contribution from the barriers is more than two orders of magnitudes weaker, demonstrating that carrier capture into the wells is dramatically enhanced in comparison to SQW structures. A decrease from $d_W = 4.8$ nm to 2.8 nm shifts the PL peak by 40 meV to higher energies, signifying stronger confinement in the thinner well. It should be emphasized that the low-temperature spectral widths of the MQW PL bands are only slightly increased in comparison to single quantum well structures. This demonstrates, in agreement with the TEM data, that the layers composing the heterostructure are indeed of excellent uniformity. With respect to the absorption, the PL peak position is low-energy shifted as shown in Fig. 4.10(a). The absorption maximum at 3.4 eV is due to the ground-state exciton of the MQW, while the steep rise above 3.57 eV is caused by the onset of bar-

4.4 ZnO/ZnMgO MQWs: Structural and optical properties

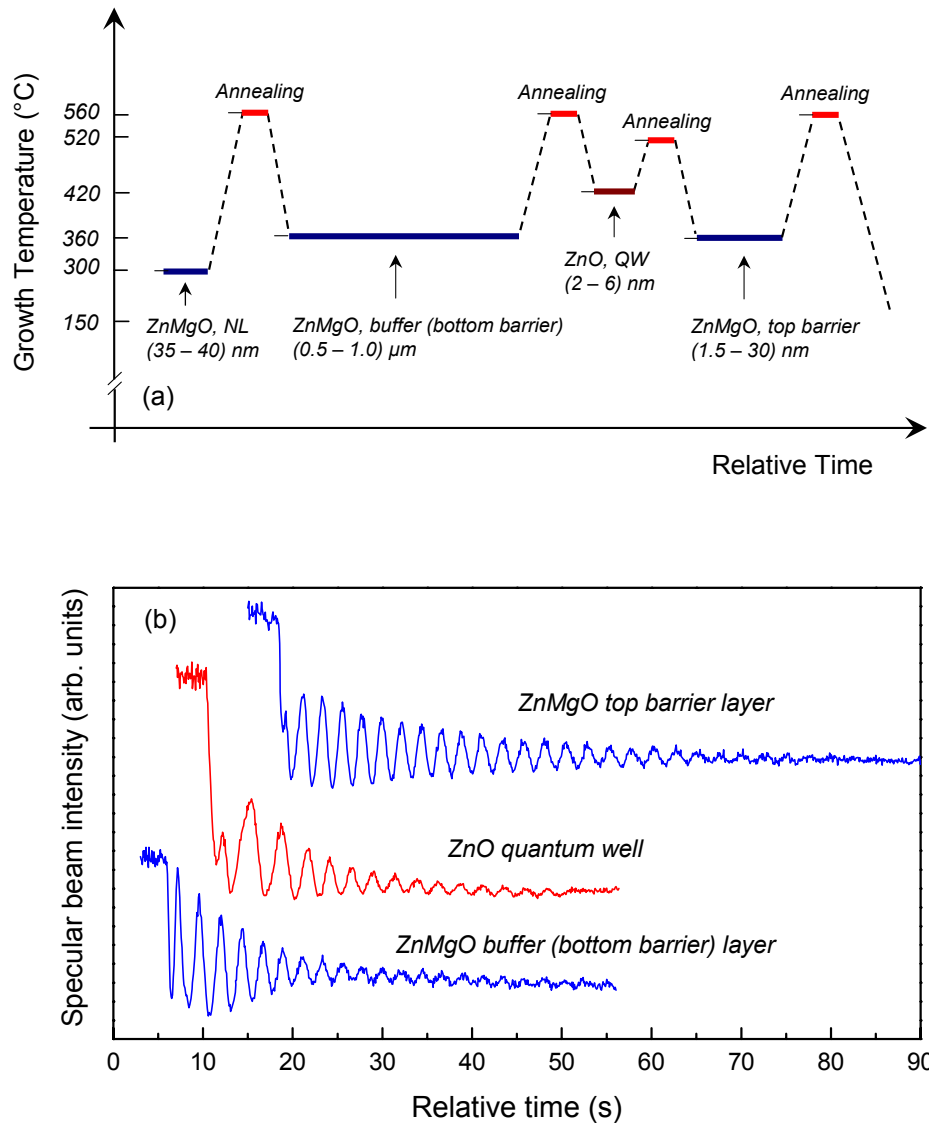


Abbildung 4.6: (a) Typical growth scheme for the fabrication of ZnO/ZnMgO SQWs. (b) RHEED specular-beam intensity oscillations recorded during growth of a ZnO/ZnMgO QW structure ($x = 0.21$, bottom epilayer thickness: 490 nm, $d_w = 4.0$ nm).

rier transitions. The Stokes shift of 30 meV is indicative of quite strong localization. In view of the small exciton Bohr radius (1.8 nm) in ZnO, composition fluctuations play probably a leading role. The PL decay depicted in Fig. 4.10(b) is in good approximation single exponential. The low-temperature life-time of 210 ps is in the range expected for

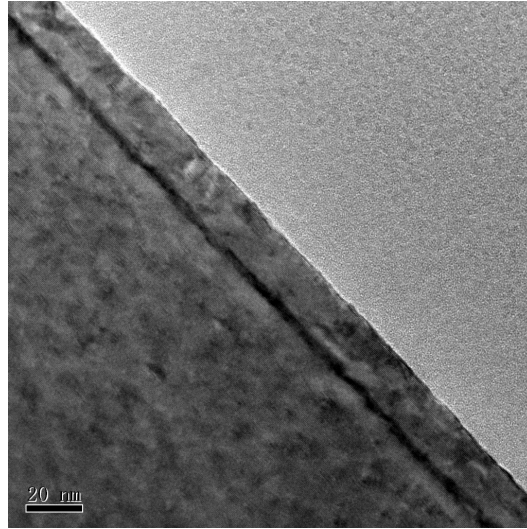


Abbildung 4.7: TEM image of ZnO/ZnMgO single QW structure. ZnO layer is dark in colour. (Ch. Zheng, H. Kirmse, and W. Neumann, Humboldt Universität zu Berlin).

the radiative decay of localized excitons. One can conclude that similar to GaN-based structures nonradiative recombination plays nonessential role in the present MQWs, despite of the $\sim 10^{10} \text{ cm}^{-2}$ dislocation density. This remains also true at room temperature where the life-time becomes only twice shorter. Localization prevents that the excitons reach the dislocations which act as quenching sites. A detailed inspection of the PL transients reveals a short rise time of about 10 ps that is related to the capture of the excitons by wells. Such fast capture is consistent with the very small barrier contributions in the steady state PL spectra.

On appropriately designed MQW structures laser action up to RT is achieved. This is demonstrated in Fig. 4.11 for a five period ZnO/Zn_{0.80}Mg_{0.20}O MQW structure with a separate optical confinement, where the first part of the ZnMgO buffer layer is grown with an increased Mg concentration of 30% to act as a cladding that improves the optical overlap [Fig. 4.11(a)]. Distinct laser action in edge emission geometry emerges above a threshold of about 150 kW/cm^2 at 300 K. The energy position, comb of modes and the temperature dependence of the threshold signify that localized states are crucially involved in the laser action [CSB⁺06].

4.5 Conclusion

It is shown that radical-source MBE is a very suitable technique to fabricate high-quality ZnO/ZnMgO heterostructures. LT growth of ZnMgO circumvents phase separation, formation of polycrystalline phases and fast surface roughening up to a Mg mole fraction of 0.40. Annealing at higher temperatures improves the surface morphology and

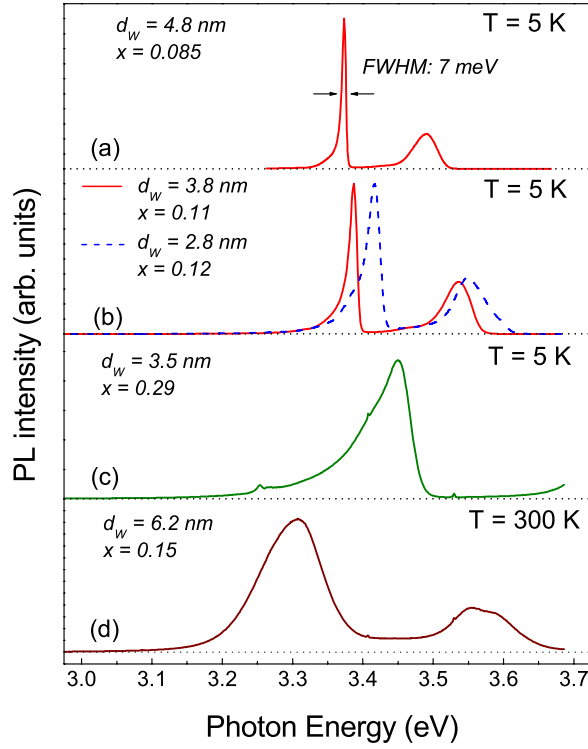


Abbildung 4.8: PL spectra of ZnO/ZnMgO QW structures measured at liquid helium (a-c) and room (d) temperature excited with the 334-nm line of Ar⁺-laser. The high-energy bands represent barrier emission, not observed for the $x = 0.29$ structure, as the excitation is below the ternary band-edge.

allows one to achieve a layer-by-layer growth mode, as indicated by distinct RHEED intensity oscillations. This approach yields single and multiple QW structures with abrupt interfaces. Bright excitonic emission is observed in a wide range of structural designs. Moreover, appropriately designed ZnO/ZnMgO MQW structures are capable of efficient lasing up to room temperature.

To the best of my knowledge, the substantive scientific results demonstrated for the first time include the following: (1) specific growth procedure combining LT deposition and annealing at each interface, (2) RHEED intensity oscillations recorded during growth of ZnMgO ternaries, (3) QW structures with abrupt interfaces grown on sapphire substrates, and (4) capable of lasing ZnO/ZnMgO MQWs grown by MBE.

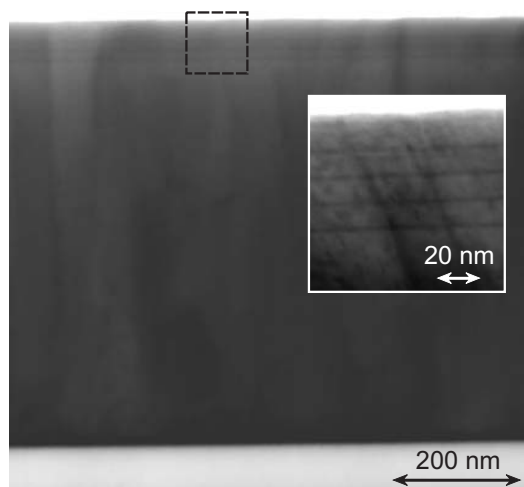


Abbildung 4.9: Cross-section STEM image of the five-fold stacked ZnO/ZnMgO QW structure grown on $\text{Al}_2\text{O}_3(11\bar{2}0)$. The inset shows a magnified view of the QW region marked by the square. (R. Schneider, D. Litvinov and D. Gerthsen, Universität Karlsruhe).

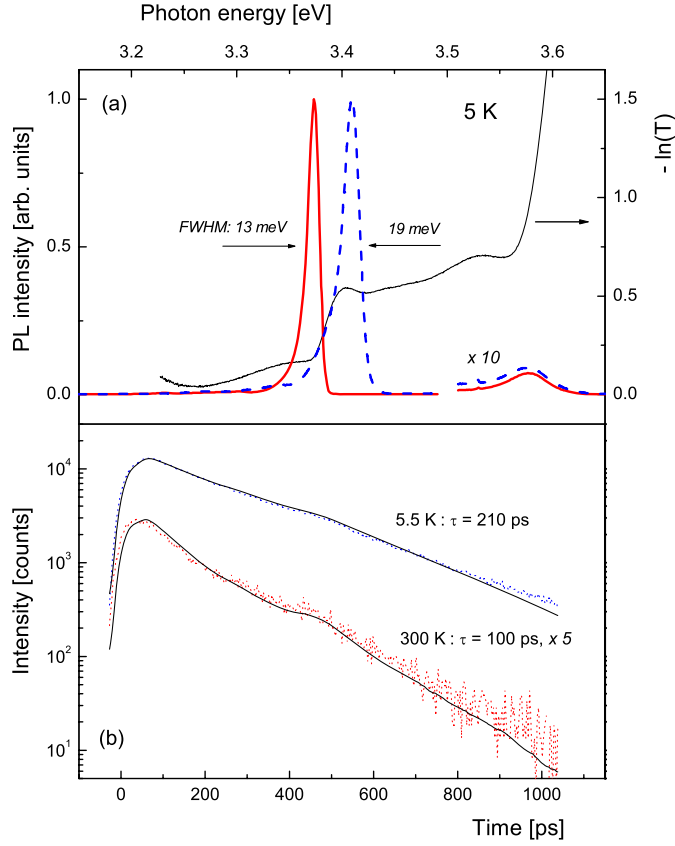


Abbildung 4.10: PL spectra of five-period ZnO/Zn_{0.86}Mg_{0.14}O MQW structures: (a) surface PL, excited by the 334-nm line of an Ar⁺-laser, 5 K. The well widths are 4.8 nm (solid curve) and 2.8 nm (dashed curve), respectively. The optical absorption spectrum for $d_W = 4.8$ nm is shown by the solid line where interference effects in the transparent region below 3.35 eV are not corrected for; (b) PL decay traces (dots) taken at the PL maximum of the 4.8 nm MQW under ps excitation above the barrier absorption edge, upper curve: 5 K, lower curve: 300 K. The solid line is a single exponential fit to the data points by convolution with the response of the time-correlated single-photon counting system used for detection.

4 Growth of ZnMgO alloys and ZnO/ZnMgO quantum well structures

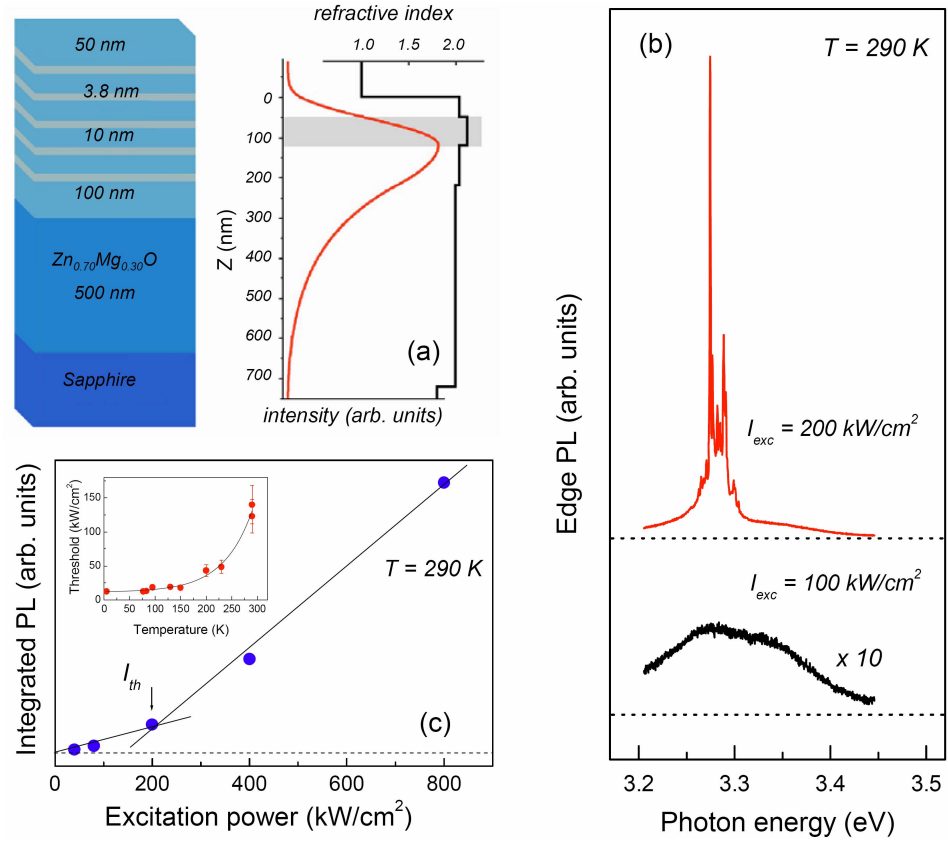


Abbildung 4.11: (a) Design of the MQW structure with a separate optical confinement; (b) Refractive index and intensity of guided wave relevant for MQW emission along growth direction; (c) Edge PL spectra below and above lasing threshold; (d) Integrated edge PL yield vs. excitation intensity at 290 K. Inset: Temperature dependence of the lasing threshold.

5 Growth of ZnCdO alloys and ZnCdO/ZnO heterostructures

5.1 Introduction

Ternary ZnCdO is a material with considerable potential for optoelectronic applications as it can cover in principle band-gaps extending from the UV to the near infrared spectral range. However, a serious obstacle that has to be overcome is phase separation forced by the different crystal structures of the binaries, wurtzite for ZnO and rocksalt for CdO. Unlike ZnMgO, which can be already quite routinely prepared by PLD or MBE [OKK⁺98, KNH⁺05, SBC⁺05], the fabrication of ZnCdO is much more complicated. This Chapter summarizes the very recent efforts to grow this ternary far beyond the equilibrium solubility limit by MBE, to fabricate hetero- and QW structures, and to elaborate their electronic and optical properties, culminating in the demonstration of optically pumped laser action up to the green spectral range.

5.2 Radical-source MBE of ZnCdO alloys

5.2.1 Fabrication of ZnCdO alloys

HT deposition of binary CdO on ZnO(000 $\bar{1}$) buffer

High temperatures enabling a system to reach the minimum of its free energy are favorable in any growth process because such conditions normally result in better material quality. However, in the case of metastable alloys and low-dimensional systems (e.g. GaNAs, GaMnAs, Ge/Si(001), CdSe/ZnSe or even ZnMgO) one often has to go to the low-temperature limit in order to kinetically freeze the surface migration processes and to fight against thermodynamics. Previous epitaxial work on ZnCdO has exploited a temperature range of (325 - 600) °C (see Chapter 2). These temperatures, however, seem to be too high in a view of the Cd volatility¹ and the typical growth temperatures of CdSe layers ($T_g = 230$ °C) employed in the ZnSe/CdSe MBE [RLH98, SBH04]. At such elevated temperatures, desorption of Cd from the growing surface is strongly enhanced, preventing its incorporation into the lattice. On the other hand, binary CdO can be grown even at $T_g = 560$ °C. Insertion of a buffer layer (ZnO or ZnMgO) separating the highly disturbed interface region from the relevant film allows one to start the deposition with an atomically-flat surface of the wurtzite-type crystal. This, in turn, enables one to accurately monitor the initial stages of the CdO or (Zn,Cd)O

¹Vapor pressure of Cd at 320 °C is 10^{-1} Torr [Mar67].

growth, which is not possible in the case of the bare sapphire substrate [SKK⁺00]. According to XRD, CdO layers deposited at this temperature have rocksalt structure with two distinct orientational domains appearing as result of different symmetries of the cubic (threefold) and hexagonal (sixfold) lattices and showing the azimuthal orientation of $[1\bar{1}0]_{\text{CdO}} \parallel [0001]_{\text{ZnO}}$ and $[\bar{1}10]_{\text{CdO}} \parallel [0001]_{\text{ZnO}}$. Figure 5.1 demonstrates a sequence of the RHEED patterns taken during initial stages of the CdO growth. When the deposition starts, a specific superstructure (SS) very similar to a (3×3) reconstruction of the ZnO buffer appears on the surface. The SS becomes much stronger with the deposition time until the contrast of the additional reflexes is comparable to that of the main features [Fig. 5.1 (b)]. Such a surface SS essentially differs from the weak (3×3) reported for GaN [SFG⁺98, DIBM99] and (Zn,Mg)O epitaxial films [OKS⁺98a, CKHY00, IFN⁺00a, SBC⁺05], and is clearly related to Cd on the surface. In what follows this SS is called as a Cd-related reconstruction or Cd- (3×3) . Whether this SS hints on a thin rocksalt or wurtzite (Cd,Zn)O layer existing on the surface or it is just a specific mechanism for the saturation of the dangling bonds in the presence of Cd is not yet clear. Continuing deposition leads to a sharp transition from a streaky to a spotty RHEED pattern, typically indicating reorganization of the 2D film into 3D islands [Fig. 5.1 (c)]. Formation of the 3D islands is, indeed, confirmed by AFM measurements performed under UHV conditions without exposure of the sample in air. Figure 5.2 shows AFM images of the underlying ZnO buffer layer [Fig. 5.2(a)], and the CdO film just beyond the 2D to 3D transition [Fig. 5.2(b)]. The surface of the CdO film is covered by 3D islands. Their lateral dimensions and average height are 20 nm and 2 nm, respectively. Below the image, the height profile taken for two neighboring islands is displayed. The transition is highly reproducible and is strongly affected by the surface smoothness. When the surface roughness increases it occurs faster under nominally identical growth conditions, sometimes even missing the stage of the Cd- (3×3) reconstruction. In fact, this observation may hint at a Stranski-Krastanow (SK) type transition with a well-defined critical thickness of the wetting layer. The local accumulation of Cd on a relatively rough surface prevents the uniform formation of a wetting layer and fastens the 2D-3D transition. The lattice constant of rocksalt CdO is $a = 4.70 \text{ \AA}$, which gives a value of $a^* = a/\sqrt{2} = 3.323 \text{ \AA}$ in the (111) plane, where the matching with ZnO occurs. It results in a lattice mismatch of about -2.2%. Cubic CdO (111) layers, coherently grown on (0001) ZnO will consequently suffer from an in-plane compressive strain and a sharp SK transition accomplished by formation of 3D islands can be expected. One has to note, that below the 2D-3D transition, the Cd- (3×3) reconstruction disappears immediately after initiation of ZnO overgrowth.

The processes described above are potentially interesting for the fabrication of self assembled CdO quantum dots in ZnO matrix, and definitely require more detailed investigation. However, first PL measurements on such samples containing stacks of 20 layers with CdO islands do not show any optical response in the visible and infrared spectral range, where the emission of pure CdO is expected. The underlying reasons are still under study.

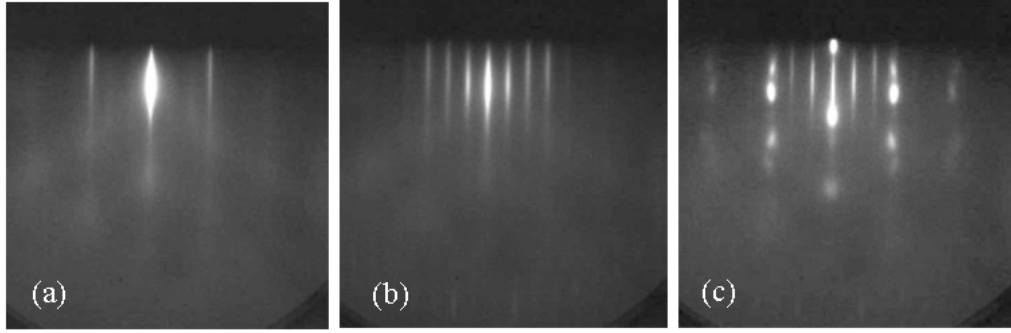


Abbildung 5.1: RHEED patterns along the $\langle 11\bar{2}0 \rangle$ azimuth, taken during initial stage of the binary CdO growth: $T_g = 560$ °C; O_2 : 400 W, 0.45 sccm; $BEP_{Cd} = 1.2 \cdot 10^{-7}$ Torr: (a) A streaky pattern from atomically smooth surface of the ZnO buffer with a sign of weak (3×3) reconstruction; (b) CdO, deposition time - 10 s; Cd-related superstructure just before a 2D-3D transition; (c) CdO, deposition time - 20 s, 2D-3D transition.

HT growth of (Zn,Cd)O films

Despite the fact that rocksalt CdO can be easily grown even at elevated temperatures, the reproducible fabrication of the ternary ZnCdO (either rocksalt, or wurtzite) in this temperature range is a very hard task. It is experimentally observed that the crystal symmetry and the composition of the grown film critically depend on the Cd/Zn BPR and the absolute Zn-flux intensity. At relatively low BPR values, Zn arriving on the surface pushes Cd atoms away from the wurtzite lattice. In this case the growth mode is practically not affected by the presence of Cd as reflected by the evolution of the RHEED pattern which is in accordance with the pure ZnO deposition scenario. The same holds true for the temperature range of (300 - 560) °C. Only at strongly reduced Zn-fluxes² and extremely high BPRs (roughly $BPR > 2.5$), a gradual transition to rocksalt (Cd,Zn)O films occurs, accompanied by appearance of the Cd- (3×3) reconstruction with a subsequent 2D-3D transition. The films grown at slightly higher Zn-fluxes ($BEP_{Zn} = 6 \cdot 10^{-8}$ Torr) often appear nonuniform in color, clearly demonstrating the existence of competing nucleation processes where the resultant crystal symmetry is defined by accidental local fluctuations of the material composition (inset to Fig. 5.3). Figure 5.3 summarizes optical transmittance spectra of (Zn,Cd)O samples fabricated in this temperature range. Note, that the layer thicknesses are strongly different, which can be seen from the position of the interference fringes. While the films grown at high Zn-fluxes and low BPRs do not show any specific features in the optical transmittance spectra related to Cd-incorporation [Fig. 5.3, curves (i, ii)], the layers grown at low BEP_{Zn} and high BPRs demonstrate very broad tails with an absorption edges extending deep to the visible spectral range [Fig. 5.3, curves (iii-v)]. Figure 5.4 shows representative AES spectra of the (Zn,Cd)O films grown under these conditions. In the case of

² $BEP_{Zn} = 4 \cdot 10^{-8}$ Torr compared to $3 \cdot 10^{-7}$ Torr for the growth of (Zn,Mg)O epilayers.

5 Growth of ZnCdO alloys and ZnCdO/ZnO heterostructures

rocksalt crystal structure, the position of the absorption edge, as well as the relative intensity of the Cd peak in AES spectra are found to be weakly sensitive to the Cd/Zn BPR, most likely indicating the incorporation of ZnO into CdO lattice. In case of AES measurements, however, one can not completely rule out the existence of different phases on a microscale, where both CdZnO rocksalt and ZnO wurtzite regions would contribute to the detected signal.

In view of the presented data, the possibility to fabricate wurtzite ZnCdO alloys at high growth temperatures seems to be rather unlikely. On the other hand, ZnO can be epitaxially grown as a single crystal practically at RT. Based on this finding we attempted MBE of ZnCdO at temperatures much low 300 °C. Owing to substantially reduced desorption rates of Zn and Cd, strongly metal-rich growth conditions are naturally favored in this case. However, (Zn,Cd)O layers grown in metal-rich mode show two systems of reflexes in the RHEED pattern already at the initial growth stage, clearly indicating phase separation. The samples are opaque in appearance and no features related to Cd are found in AES spectra. Completely different results are obtained in an O-rich regime. Under such conditions Cd is very well incorporated.

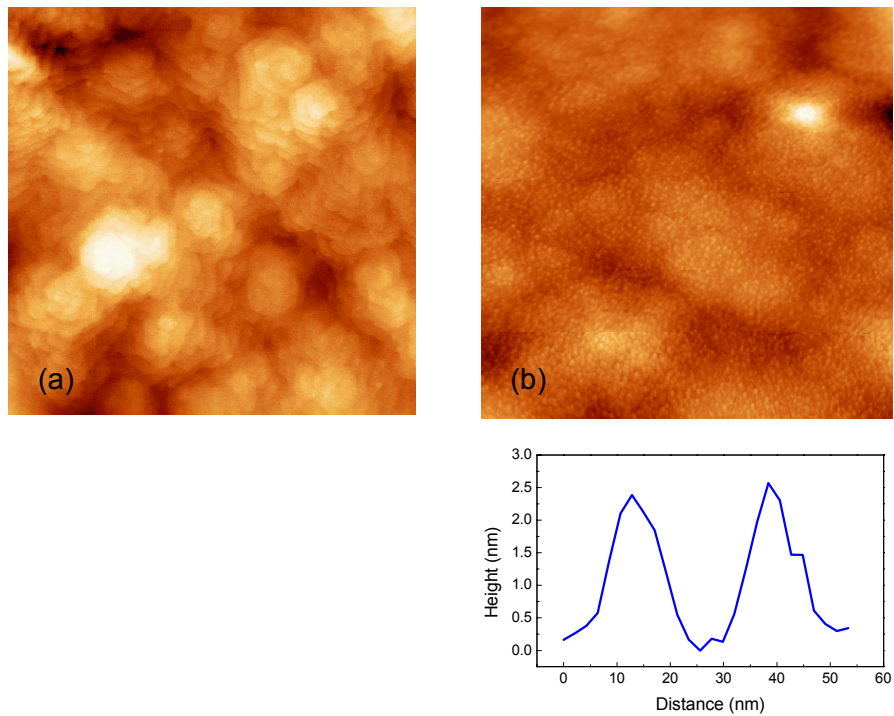


Abbildung 5.2: UHV AFM images: (a) ZnO buffer layer, the scan size is $0.8 \times 0.8 \mu\text{m}^2$; (b) CdO layer just above 2D-3D transition, the scan size is $1.0 \times 1.0 \mu\text{m}^2$. Below the image, the height profile taken for two neighboring islands is displayed. (Collected by Dr. Chenggang Xü).

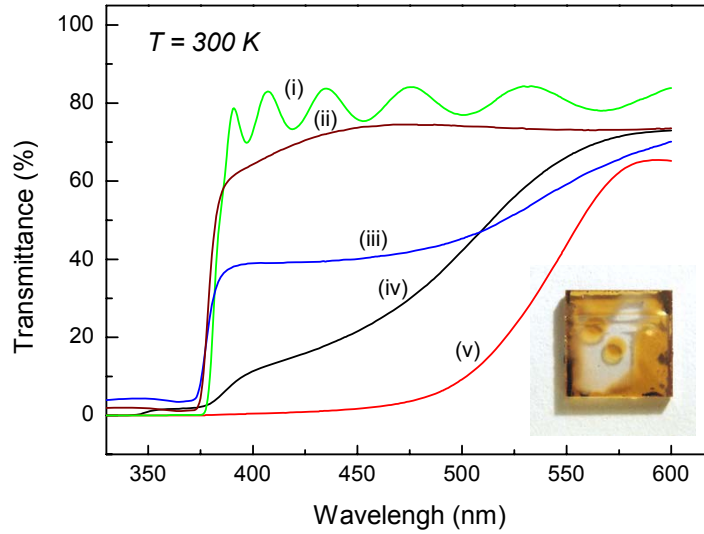


Abbildung 5.3: Room temperature optical transmittance spectra of (Zn,Cd)O films deposited on a ZnO buffer at $T_g = 560$ °C : (i) ZnO reference film; (ii) (Zn,Cd)O: $\text{BEP}_{\text{Zn}} = 3 \cdot 10^{-7}$ Torr, BPR = 0.8; (iii) CdO, several tens nm-thick: $\text{BEP}_{\text{Cd}} = 2.4 \cdot 10^{-7}$ Torr (iv) (Zn,Cd)O: $\text{BEP}_{\text{Zn}} = 4 \cdot 10^{-8}$ Torr, BPR = 2.65; (v) (Zn,Cd)O: $\text{BEP}_{\text{Zn}} = 4 \cdot 10^{-8}$ Torr, BPR = 5.3. The step in vicinity of 375 nm originates from absorption of the ZnO buffer. Inset: specific example of a (Zn,Cd)O layer grown in intermediate-regime, where both rocksalt (reddish) and wurtzite (transparent) phases coexist.

LT growth of ZnCdO alloys

The epitaxial regime required to achieve high-quality ZnCdO is quite different from that of ZnMgO or ZnO where growth temperatures between (300 - 380) °C and metal-rich conditions provide optimum results [SBC⁺05, KHN⁺04]. As outlined before, homogeneous incorporation of Cd in ZnO can not be attained in this way. On contrary, it was discovered that growth temperatures as low as $T_g = (100 - 150)$ °C in combination with strong O-excess allow for the growth of single-phase wurtzite-type ZnCdO films up to Cd concentrations of at least $y = 0.32$ [SBC⁺06b]. This is markedly beyond the equilibrium solubility limit of $y = 0.02$ as well as the upper boundary of $y = 0.07$ so far reached by other epitaxial approaches where growth temperatures between 325 °C and 600 °C have been used [MSK⁺01, GKK⁺03, BGF⁺06, SKK⁺00, CRL⁺05]. Whether the composition range can be even further extended without substantial deterioration of crystal quality is currently not clear [SNI⁺04].

Fig. 5.5 summarizes structural data of ZnCdO epilayers grown on *a*-plane sapphire. First, a 35 nm-thick LT nucleation layer followed by a 150 nm-thick buffer, both consisting of $\text{Zn}_{0.90}\text{Mg}_{0.10}\text{O}$, are deposited. O-excess is achieved by reducing the Zn BEP by

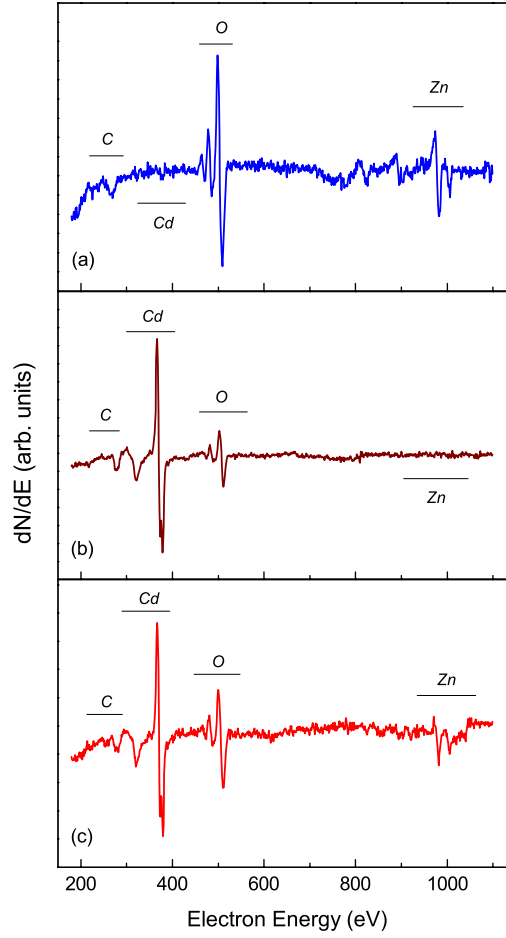


Abbildung 5.4: Representative AES spectra of (Zn,Cd)O films grown at $T_g = 560$ °C: (a) (Zn,Cd)O: $\text{BEP}_{\text{Zn}} = 3 \cdot 10^{-7}$ Torr, BPR = 0.8; (b) CdO, several tens nm-thick; (c) (Zn,Cd)O: $\text{P}_{\text{Zn}} = 4 \cdot 10^{-8}$ Torr, BPR = 2.65.

about five times in comparison to the values typically used for ZnMgO or ZnO growth. The BEP of Cd is selected as to produce the proper Cd/Zn BPR for a desired alloy composition. The Cd content deduced from EDX, as well as the relative intensity of Cd in AES spectra (not shown) increases orderly with increasing BPR [Fig. 5.5(a)]. A streaky RHEED pattern [Fig. 5.5(b)] present during the whole deposition of the typically (500 - 700) nm-thick epilayers signifies single crystalline growth in wurtzite structure. No indication of phase separation is found up to the largest Cd concentration of $y = 0.32$ so far attempted. The XRD analysis substantiates this fact quantitatively. Prominent reflexes due to wurtzite ZnCdO and ZnMgO are found [Fig. 5.5(c)]. The existence of cubic (111)-oriented ZnCdO is excluded by taking texture maps of the asymmetric (313) rocksalt reflex. The c -lattice constant systematically increases with the Cd content. The plot in Fig. 5.5(d) extends the available data range [MSK⁺01] to concentrations up

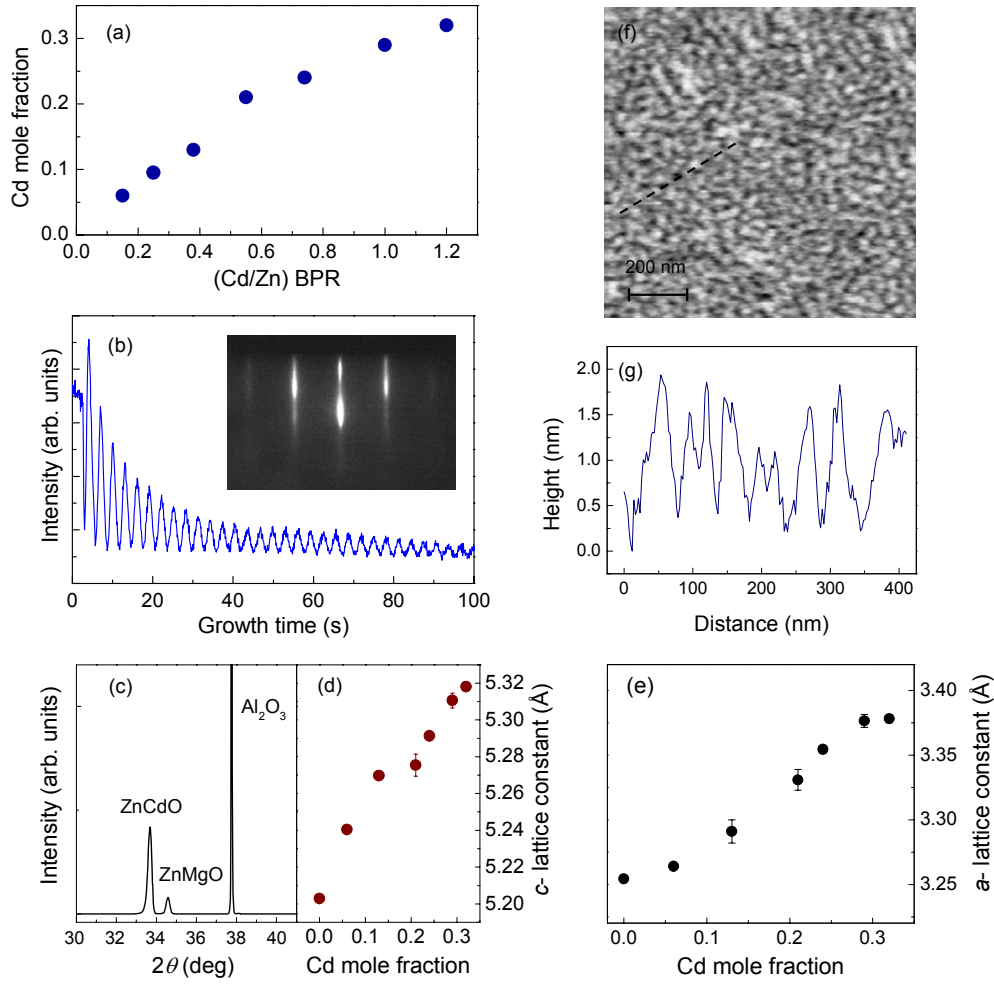


Abbildung 5.5: Low-temperature ($T_g = 150^\circ\text{C}$) MBE of ZnCdO: (a) Cd content vs Cd/Zn BPR deduced from EDX. A weak contribution from the ZnMgO buffer is not deducted. (b) RHEED oscillations after growth initiation of $\text{Zn}_{0.79}\text{Cd}_{0.21}\text{O}$, inset: RHEED pattern of a 700-nm-thick $\text{Zn}_{0.79}\text{Cd}_{0.21}\text{O}$ epilayer taken along the $\langle 11\bar{2}0 \rangle$ azimuth. (c) HRXRD scan of a ZnCdO epilayer ($y = 0.32$). Reflex features corresponding to (0002) ZnCdO and ZnMgO as well as (11 $\bar{2}$ 0) Al_2O_3 are indicated. (d, e) c - and a -lattice constant vs. Cd content, respectively. (f) AFM image of the same surface from which the RHEED pattern in the inset of (b) is recorded. (g) AFM height profile taken along the line marked in (f).

to $y = 0.32$. The same holds true for the a -lattice constant [Fig. 5.5(e)]. Unlike ZnMgO ternaries where the change of the a -lattice constant with Mg content stays well below 1% within the whole composition range [OKK⁺98], the lattice mismatch for ZnCdO

alloys reaches already the value of 2.4% for $y = 0.21$, which is in accordance with the larger tetrahedral ionic radius of Cd compared to that of Zn and Mg. A striking finding is that, despite the extremely low growth temperature, layer-by-layer growth of ZnCdO occurs as demonstrated by the observation of distinct RHEED oscillations [Fig. 5.5(b)]. Apparently, Cd favors a 2D growth mode, while ZnO has a tendency to surface roughening at such low growth temperatures. The smooth surface morphology anticipated by the RHEED data is confirmed by AFM scans [Fig. 5.5(f)]. Even after growth of 700 nm ZnCdO, atomically flat islands of several tens of nanometer lateral extension separated by 2-3 monolayer steps are observed [Fig. 5.5(g)]. The rms roughness over a scan area of $5 \times 5 \mu\text{m}^2$ is only 0.8 nm.

5.2.2 Structural properties

Figure 5.6 shows TEM microphotographs resolving the dislocation structure in a ZnCdO epilayer ($y = 0.12$) grown on top of a ZnO/sapphire template. The two images are taken from the same sample area under different diffraction conditions with $\mathbf{g} = [0004]$ and $\mathbf{g} = [11\bar{2}0]$. One can see that the predominantly extended defects are TDs parallel to the c -axis, similar as in ZnMgO films on sapphire. According to the criteria of invisibility $\mathbf{g} \cdot \mathbf{b} = 0$, Fig. 5.6(a) displays the screw component, while Fig. 5.6(b), the edge component of the TDs. Fig. 5.6 displays moreover the two interfaces (ZnO/sapphire and ZnCdO/ZnO) accommodating a high density of planar defects. While the screw dislocations rapidly annihilate beyond the thin interface regions, the density of the edge dislocations nucleated at the ZnCdO/ZnO interface remains practically unchanged and dominate the dislocation structure of the ZnCdO layer.

5.2.3 Optical properties

The incorporation of Cd is accompanied by a systematic low-energy shift of the band gap extending down to the yellow spectral range. In visual inspection, the samples appear homogeneous with a color changing from transparent to red [Fig. 5.7]. Uniform composition of the epilayers is quantitatively corroborated by EDX. In Fig. 5.8(a), optical transmittance spectra of epilayers grown on sapphire are shown for four representative alloy compositions. In the transparent range, interference fringes are seen. All epilayers exhibit band-gap-related light emission under optical excitation visible to the naked eye up to room temperature. Respective PL spectra are collected in Fig. 5.8(b). The apparent substructure of some PL bands is a result of optical interference effects as suggested by corresponding features in transmittance. The fact that the PL is markedly red-shifted with respect to the absorption edge is indicative of localized transitions (see also Ref. [BBP⁺07]).

5.2 Radical-source MBE of ZnCdO alloys

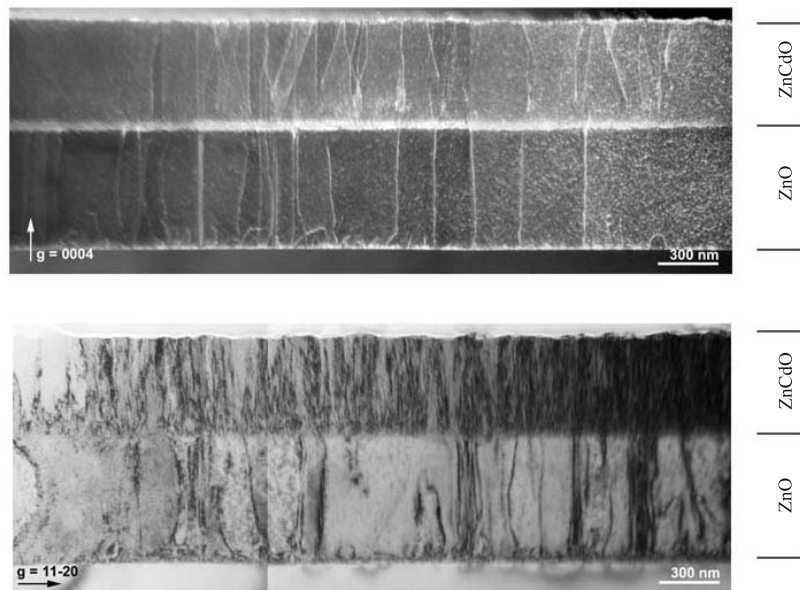


Abbildung 5.6: TEM images of a 500-nm-thick ZnCdO ($y = 0.12$) epilayer grown on ZnO(0001)/sapphire template: (a) dark-field, $\mathbf{g} = [0004]$; (b) bright-field, $\mathbf{g} = [11\bar{2}0]$. (I. Häusler, H. Kirmse, and W. Neumann, Humboldt-Universität zu Berlin).

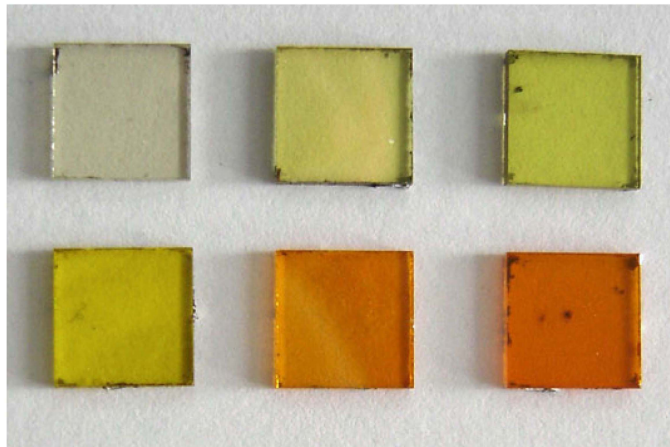


Abbildung 5.7: ZnCdO epilayers grown on a -plane sapphire substrates by LT MBE.

5.3 Quantum well structures

5.3.1 Growth

Single-crystalline layer-by-layer growth and smooth surface morphology are necessary prerequisites for the fabrication of well-defined hetero- and QW structures. Fig. 5.9 (a) describes schematically the growth procedure applied for ZnCdO/ZnO SQW structures on sapphire. The ZnCdO well is embedded between a 500 nm-thick ZnO buffer and a 30 nm-thick ZnO cap layer. Both well and ZnO cap are deposited at $T_g = 150^\circ\text{C}$ without any growth interruption introduced in between, while the ZnO buffer is grown at $T_g = 360^\circ\text{C}$ and annealed for several minutes at $T_a = 560^\circ\text{C}$ to smoothen the surface [SBC⁺05]. Distinct RHEED oscillations enable one to control precisely the nominal layer thickness. Moreover, growth under strong O-rich conditions allows for the direct determination of the ZnCdO ternary alloy composition in the QW region from the variation of the growth rate between ZnO and ZnCdO [Fig. 5.9(b)]. Using this approach one can systematically fabricate SQWs in a wide range of thicknesses (1.2 - 5.4 nm)

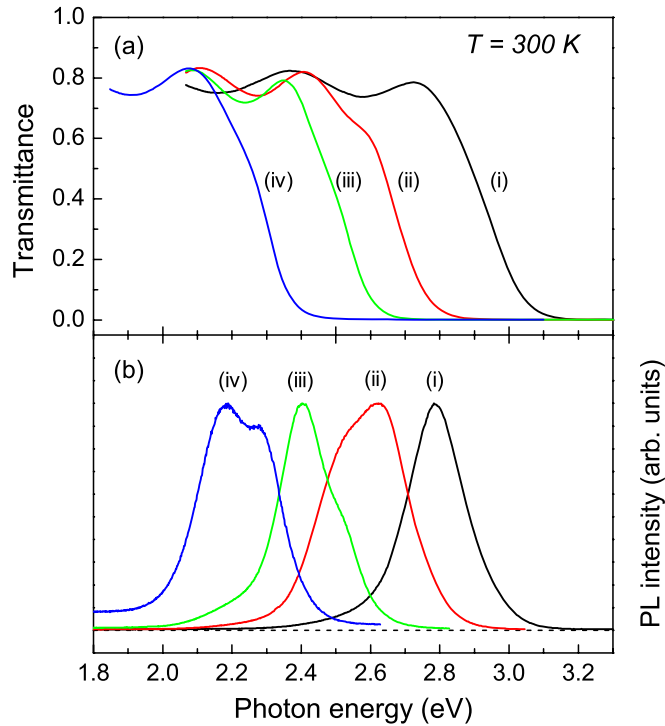


Abbildung 5.8: Optical properties of ZnCdO epilayers grown by low-temperature MBE on *a*-plane sapphire. (a) Transmittance at room temperature for the Cd content y of (i) 0.06, (ii) 0.13, (iii) 0.21, and (iv) 0.32. (b) Room temperature PL of the same epilayers as in (a) excited above the ZnMgO buffer band gap.

and compositions ($y \leq 0.30$). It can be also extended to the growth of MQW structures. Uniform stacks with up to 10 wells have been successfully grown in this way.

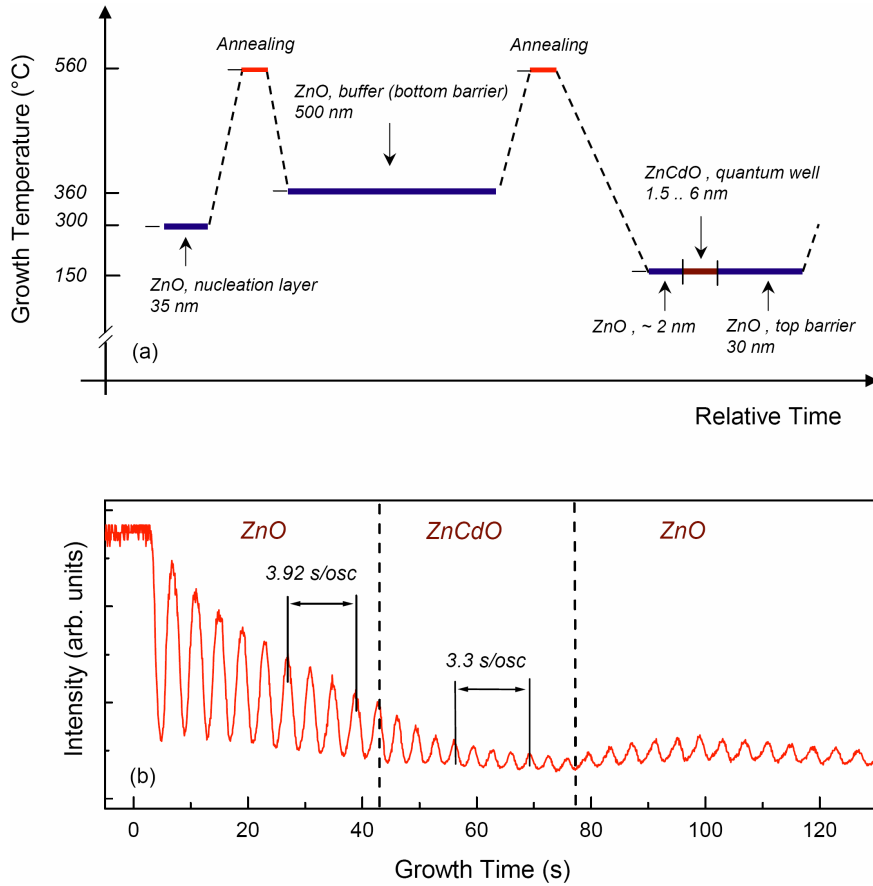


Abbildung 5.9: Typical growth scheme for the fabrication of ZnCdO/ZnO QWs on *a*-plane sapphire. (b) RHEED oscillations recorded during fabrication of a ZnCdO/ZnO SQW structure, $T_g = 150^\circ\text{C}$.

5.3.2 Postgrowth annealing: A way to increase the radiative efficiency

LT growth is a need to form well-defined hetero- and QW structures. However, restricted migration length and limited desorption of adatoms in such case are generally considered as the main sources for the generation of lattice imperfections (mainly point defects) deteriorating the radiative efficiency. Post-growth annealing, as known from other heteroepitaxial systems (e.g. GaMnAs [EBW⁺04], GaInNAs [SCH⁺01]), is a powerful tool to remove these defects by out-diffusion and/or annihilation. A critical issue, when applying such procedures to ZnCdO alloys, is thermal stability with respect to a wurtzite-cubic phase transition. In order to investigate thermal stability of fabricated films, the samples are annealed for 5 h under UHV conditions directly after

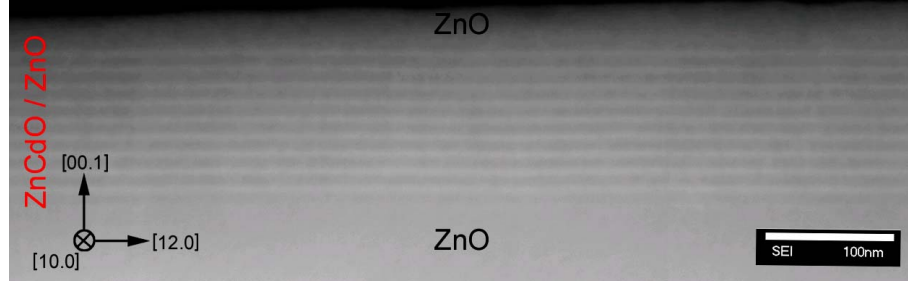


Abbildung 5.10: Composition-sensitive TEM image of the 10-period ZnCdO/ZnO MQW structure. ZnCdO well layers are clearly visible. (I. Häusler, H. Kirmse, and W. Neumann, Humboldt Universität zu Berlin).

growth. The relatively long annealing time ensures that the structural changes evolve at least close to steady state.

Fig. 5.11(a) shows a typical RHEED pattern of an as-grown ZnCdO epilayer. Post-growth annealing performed at $T_a = 520^\circ\text{C}$ improves further the surface smoothness [Fig. 5.11(b)]. This can be clearly recognized from the reduction of the diffuse background in the RHEED pattern, disappearance of the fine V-notch features and the extra modulation of the intensity along the streaks. Moreover, a specific Cd-(3×3) superstructure associated with thermally activated diffusion of Cd out of the ZnCdO bulk and its accumulation on the surface, becomes distinctly visible [Fig. 5.11(b)]. The characteristic RHEED pattern starts already to appear around $T_a = 310^\circ\text{C}$. Such a low on-set points at the breaking of weak bonds like Cd interstitials, whereas, according to HRXRD, the diffusion of Cd substitutionals seems to be still of minor importance in this temperature range. Figure 5.12 shows HRXRD reciprocal space maps of the symmetric (0002) reflection for the as-grown ZnCdO epilayer with the Cd content of $y = 0.12$, as well as the same sample annealed at 350°C and 520°C . ω and 2θ are the angles formed by the primary beam with the sample surface and the direction of detection, respectively. The reciprocal coordinate qx is given by the intersection of the diffraction plane and the surface, and qz corresponds to the surface normal, i.e.,

$$\begin{pmatrix} qx \\ qz \end{pmatrix} = \frac{2\pi}{\lambda} \left\{ \begin{pmatrix} \sin(\theta - \omega) \\ \cos(\theta - \omega) \end{pmatrix} - \begin{pmatrix} -\sin \omega \\ \cos \omega \end{pmatrix} \right\}.$$

The space maps expose two distinctly different intensity maxima corresponding to a 600 nm-thick ZnO buffer and about 500 nm-thick ZnCdO layer. The ZnCdO features have a specific elongated shape indicating the variation of the d -lattice spacing. This variation may originate from both the composition and the strain inhomogeneities. However, reciprocal space maps taken in vicinity of the asymmetric ($11\bar{2}4$) reflection indicate that just the strain inhomogeneities are most likely responsible for the observed intensity distribution (see Chapter 6). While annealing at 350°C only slightly changes a

profile of the Cd intensity maximum [Fig. 5.12(b)], at higher temperature [$T_a = 520^\circ\text{C}$, Fig. 5.12(c)] an additional tail spreading in the direction of the lower qz values appears near the ZnO feature, indicating the onset of interdiffusion. Another noticeable change of the ZnCdO relaxation state is a narrowing the ZnCdO intensity distribution. Despite a sign of intermixing observed, no change of the lattice c - constants between as grown and annealed samples is found. Also no signature of phase separation is detected, demonstrating stability of the ZnCdO films at least up to $T_a = 520^\circ\text{C}$.

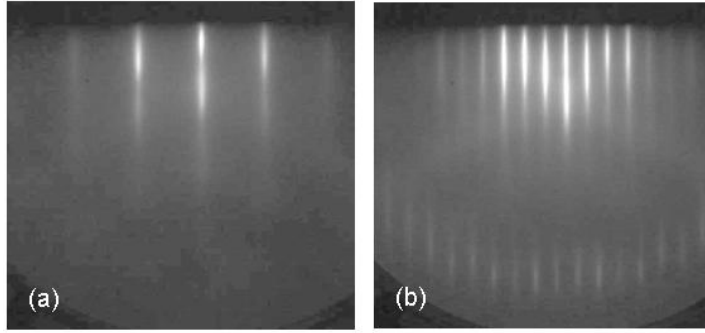


Abbildung 5.11: Annealing of ZnCdO. RHEED patterns of a 350 nm-thick $\text{Zn}_{0.88}\text{Cd}_{0.12}\text{O}$ epilayer taken along the $\langle 11\bar{2}0 \rangle$ azimuth: (a) as grown, (b) annealed for 5 h at $T_a = 520^\circ\text{C}$.

The problem of intermixing becomes even more critical for QW structures due to the higher composition gradient. When applying the annealing procedure to QWs, the removal of defects has to be compromised with the well widening. In this case the maximal Cd diffusion length can be estimated from the appearance of a Cd-(3×3) SS on the ZnO cap layer surface. Fig. 5.13(a) depicts the SS for a single $\text{Zn}_{0.81}\text{Cd}_{0.19}\text{O}/\text{ZnO}$ QW located 1.9 nm beneath the sample surface and annealed at $T_a = 350^\circ\text{C}$. However, it is no more observable when the cap is enlarged to 3.6 nm. From this data one can conclude that the possible Cd interdiffusion length in ZnCdO/ZnO in this composition and temperature range is 2-3 nm.

As can be directly seen in Fig. 5.13(b), annealing at $T_a = 350^\circ\text{C}$ strongly suppresses defect-related emission, preexisting on the as-grown SQW structures, and enhances the band-gap related signal by more than one order of magnitude. The increase of the radiative yield is accompanied by a high-energy shift of the emission maximum. At intermediate T_a , the shift is only 30 meV, while it can reach several 100 meV at high annealing temperatures. The physical processes behind the observable high-energy shift of the PL peak position still require further investigation. Most probable reasons are the Cd outdiffusion from the well layer enforced for QWs in comparison with ZnCdO epilayers, and/or the partial strain redistribution resulting in reduction of the polarization fields. This trade-off has to be optimized when aiming at QW structures emitting in the green wavelength range or at even longer wavelengths.

5 Growth of ZnCdO alloys and ZnCdO/ZnO heterostructures

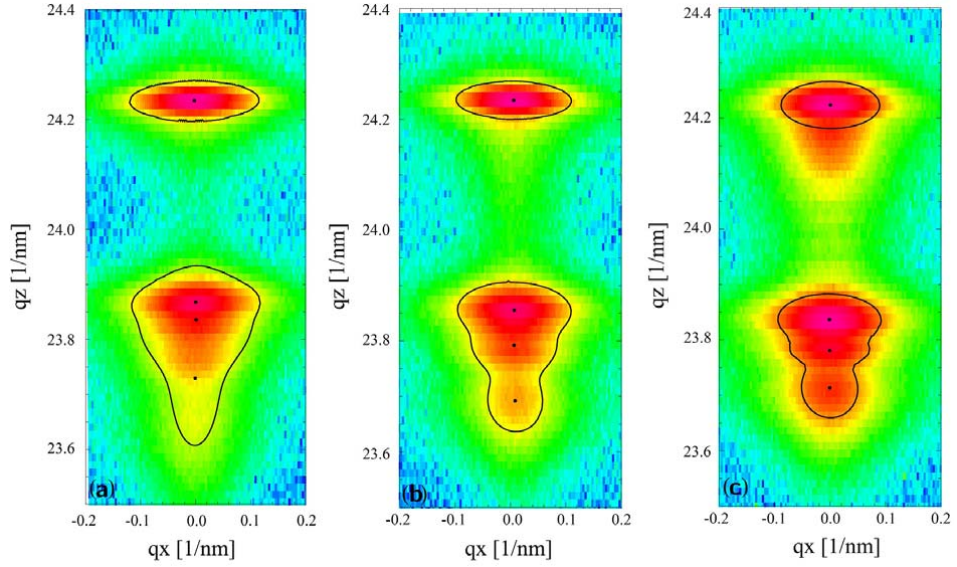


Abbildung 5.12: XRD reciprocal space maps of the symmetrical (0002) reflection of a 350 nm-thick $\text{Zn}_{0.88}\text{Cd}_{0.12}\text{O}$ epilayer grown on top of a ZnMgO buffer: (a) as grown, (b) annealed for 5 h at $T_a = 350^\circ\text{C}$; (c) annealed for 5 h at $T_a = 520^\circ\text{C}$.

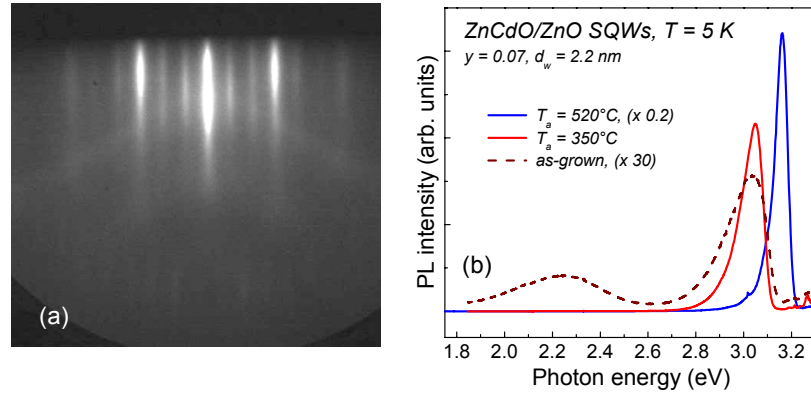


Abbildung 5.13: Annealing of ZnCdO/ZnO QW structures. (a) RHEED pattern of a ZnCdO/ZnO ($y = 0.19$) single QW structure with a well width of 3.6 nm and a 1.9 nm-thick ZnO cap after rise of the temperature from $T_g = 150^\circ\text{C}$ to $T_a = 350^\circ\text{C}$. (b) PL of a 2.2 nm-thick ZnCdO/ZnO ($y = 0.07$) single QW well structure before (dashed, brown) and after annealing at $T_a = 350^\circ\text{C}$ (red) and 520°C (blue). Excitation is with the 355 nm frequency tripled output of a Nd:YVO₄ laser.

5.3.3 Polarization fields in ZnCdO/ZnO SQW structures

The growth direction of the QW structures is along the polar c -axis of the wurtzite lattice. As a consequence, built-in electric fields originating from spontaneous as well as piezoelectric polarizations are generated [BFV97]. When aiming at light-emitting devices, screening of the polarization charges by the injected carriers is of direct practical relevance. On the other hand, polarization fields can induce a 2D carrier gas at the heterointerface that can be exploited for high-speed electronic applications. Theoretical work has predicted similarly huge polarization effects for ZnO/CdO as for nitride-based heterostructures [GS06].

Fig. 5.14 summarizes steady-state PL data of SQW structures in the low-density excitation regime. As depicted in Fig. 5.14(a) for a Cd concentration of $y = 0.11$, the PL spectrum of the SQW structures exhibits features from ZnO and the broader well emission on the low-energy side. Despite the much larger ZnO volume, the total yield of the low-energy PL is clearly stronger. This fact demonstrates efficient carrier capture by the SQW. The position of the well PL undergoes a low-energy shift of about 0.8 eV when the well width d_W increases from 1.2 to 5.4 nm. As seen from the plot in Fig. 5.14(b), the shift is very closely linearly related to d_W . The same holds true when the PL position is plotted versus the Cd concentration at fixed well width [Fig. 5.14(c)], though a weak nonlinearity is indicated at higher y .

The time-resolved PL transients represented in Fig. 5.15 reveal that the low-energy shift of the well PL is accompanied by a dramatic slow-down of the PL decay from about 500 ps up to the 100- μ s range. The transients are non-exponential reflecting that the states behind the PL are not homogeneously broadened. Using a stretched exponential function $I(t)/I(0) = \exp(-t^\kappa/\tau^\kappa)$, the characteristic lifetime is determined from the area under the transients $\tau_{\text{eff}} = \int_0^\infty dt I(t)/I(0) = \Gamma(1/\kappa)\tau/\kappa$. A striking observation is that the yield of the wide SQW in Fig. 5.14(a) is only reduced by a factor of 1.5 relative to the 1.5 nm structure. That is, despite the extremely long lifetime, non-radiative processes are not substantially enhanced.

For wider SQWs an increase of the excitation intensity induces a high-energy shift of the well PL of several 100 meV as shown in Fig. 5.16. The shifts sets off already under steady-state excitation, but is much stronger under pulsed pumping starting at about 10 kW/cm². No saturation is found up to excitation levels of 1 MW/cm². In parallel, the PL decay becomes faster by orders of magnitude and reaches the sub-ns time-scale.

The above observations consistently evidence the presence of very strong polarization fields. The almost linear dependence of the optical transition energy on the well width as well as on the Cd concentration is fully confirmative of a high-field regime where the dominant energy contribution is given by the potential drop across the well $e\Delta\phi = eF(x)d$. Therefore, irrespective of the band structure details, the built-in electric field can be directly extracted from the experimental data providing $F/x = (1.6 \pm 0.2) \cdot 10^9$ V/m [Fig. 5.14(b)]. This value is quite similar to the InN/GaN heterosystem [CAM⁺98, IKO⁺98, LMG⁺01], but roughly a factor of five larger than data reported for ZnO/ZnMgO [MBL⁺05]. The carriers generated by optical pumping screen the polarization fields. This is clearly manifested experimentally by the high-energy shift of

the PL features as well as the shortening of the lifetime signifying recovery of strong overlap between electron and hole wavefunction.

5.4 Visible wavelength lasing of ZnCdO/ZnO multiple quantum well structures

The above findings allow one to design MQW structures capable of lasing under optical pumping. Stacks of 5-10 QWs separated by (8-10) nm-wide ZnO barriers are embedded in ZnMgO claddings in order to improve optical mode overlap. The thickness of the bottom layer (~ 600 nm) is about four times larger than of the upper cap. Optical excitation is performed by an excimer laser pumped dye laser with a pulse duration of 20 ns. The laser photon energy is set below the absorption edge of the ZnMgO claddings but above the absorption edge of the ZnO barriers. Surface emission spectra are recorded in backward geometry. A small excitation spot of $300 \times 300 \mu\text{m}^2$ is used in order to minimize distortion by stimulated emission. In the lasing measurements, the excitation spot is a stripe of $300 \mu\text{m}$ width and $1500 \mu\text{m}$ length. The emission signal is detected in the direction along the stripe from the edges of the sample.

Fig. 5.17 depicts low-temperature data of a blue emitting structure. The spontaneous emission in backward geometry is spectrally broad and the shape almost independent on the excitation intensity. Both facts suggest that localized electron-hole pairs are involved in the radiative recombination. As described in the previous section, polarization fields are largely screened at the excitation level of Fig. 5.17(a). In the same excitation range, distinct laser action emerges in the edge configuration [Fig. 5.17(b)]. The presence of a comb of modes is consistent with an inhomogeneously broadened laser transition. Typically, the lasing band is situated on the high-energy side of the spontaneous emission maximum. Here, the larger optical density of states is sufficient to overcome residual absorption from claddings and barriers and to meet the gain-loss condition. Further contributions might result from a specific waveguide geometry or excited-state lasing as known from self-assembled QD structures. The laser threshold of $60 \text{ kW}/\text{cm}^2$ is comparable to ZnO/ZnMgO structures [OTK⁺00, CSB⁺06] as well as state-of-the-art data for optically pumped InGaN/GaN MQW structures [LDT⁺07].

Further characteristics of the laser action are summarized in Fig. 5.18. The spectral position where the lasing occurs can be systematically tuned by structure design. At given Cd concentration, the wider well lases at lower photon energy [curve 1 and 2 in Fig. 5.18(a)] consistent with the weaker quantum confinement. A higher Cd concentration shifts the lasing orderly to lower energies (curve 2-5). The lowest energy achieved so far is 505 nm, which corresponds to the green wavelength range. Laser action without qualitative change in appearance is present up to room temperature [Fig. 5.18(b)]. The laser threshold only moderately increases from 5 to 290 K. This fact is again in accord with the localized nature of carrier states involved in the lasing process.

5.5 Conclusion

The fabrication of ZnCdO wurtzite ternaries was accomplished for the first time in a highly nonequilibrium growth mode using a specifically tailored MBE procedure. Single phase behavior and a systematic shift of the band edge is found up to a Cd content of $y = 0.32$. Whether this range can be further extended has not yet been investigated. The developed approach enables to utilize ZnO band-gap engineering and predestine ZnCdO for various optoelectronic applications. The first ZnCdO/ZnO single and multiple QW structures were presented. In appropriately designed ZnCdO/(Zn,Mg)O MQWs, laser action under optical pumping could be demonstrated at wavelengths that go currently beyond the range covered by the InGaN/GaN hetero-system.

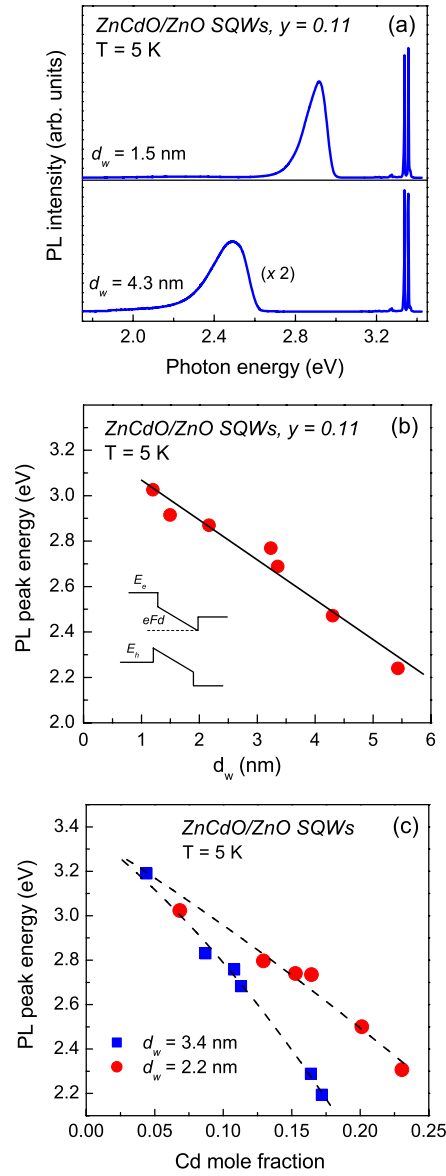


Abbildung 5.14: PL data of ZnCdO/ZnO SQW structures. (a) Overview spectra of two structures with the same Cd concentration $y = 0.11$ but different well width of $d_w = 1.5$ and 4.3 nm, respectively. (b) PL peak energy versus well width for $y = 0.11$. The line represents the slope given by the potential drop across the SQW $e\Delta\phi = (1.75 \cdot 10^8 \text{ eV/m})$ as shown in the inset. (c) PL peak energy versus Cd concentration at fixed well width of $d_w = 2.2$ and 3.4 nm, respectively. The dashed curves are to guide the eye. The excitation intensity is $I_{exc} = 500 \text{ mW/cm}^2$ in (a) and 10 mW/cm^2 in (b) and (c).

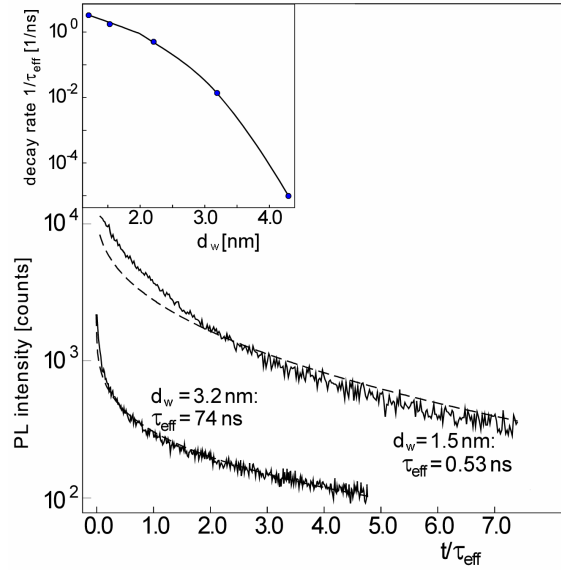


Abbildung 5.15: Time-resolved PL data of ZnCdO/ZnO SQW structures. Main panel: Exemplary PL transients plotted in units of characteristic time τ_{eff} (see text). Inset: Life-time versus well width extracted from the transients by using a stretched exponential decay function as shown by the dashed curves in the main panel ($y = 0.11$).

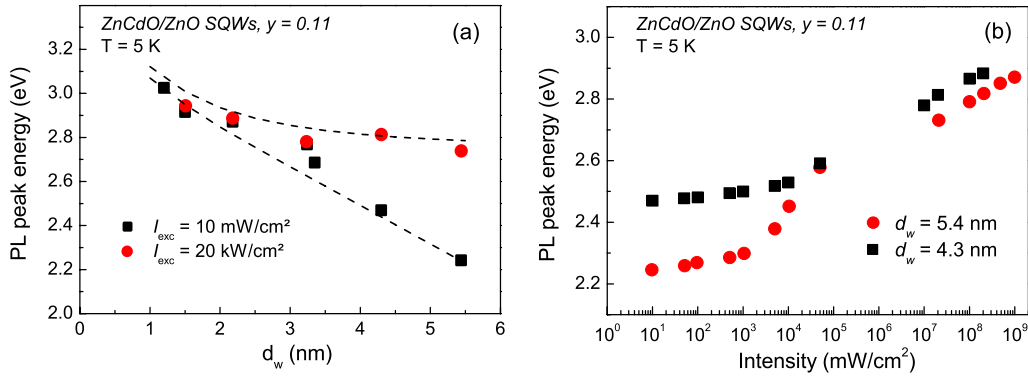


Abbildung 5.16: Effect of optical excitation on the PL from ZnCdO/ZnO SQWs. (a) Peak position at low and high excitation versus well width ($y = 0.11$). The lines are calculated energies for wells with (lower) and without (upper) polarization field. (b) Peak position versus excitation intensity for structures with $y = 0.11$ and $d_w = 4.3$ nm or 5.4 nm.

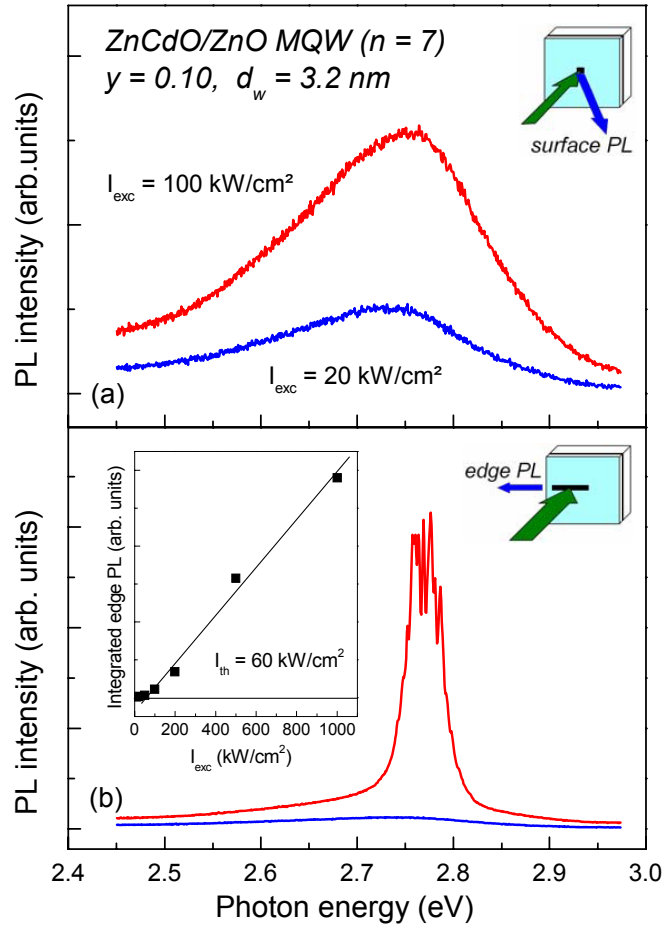


Abbildung 5.17: Emission from a ZnCdO/ZnO MQW structure grown on a -plane sapphire. Temperature: 5 K. (a) Spontaneous emission taken in backward geometry. (b) Laser action observed from the sample edges at the same I_{exc} . Inset: Lasing threshold.

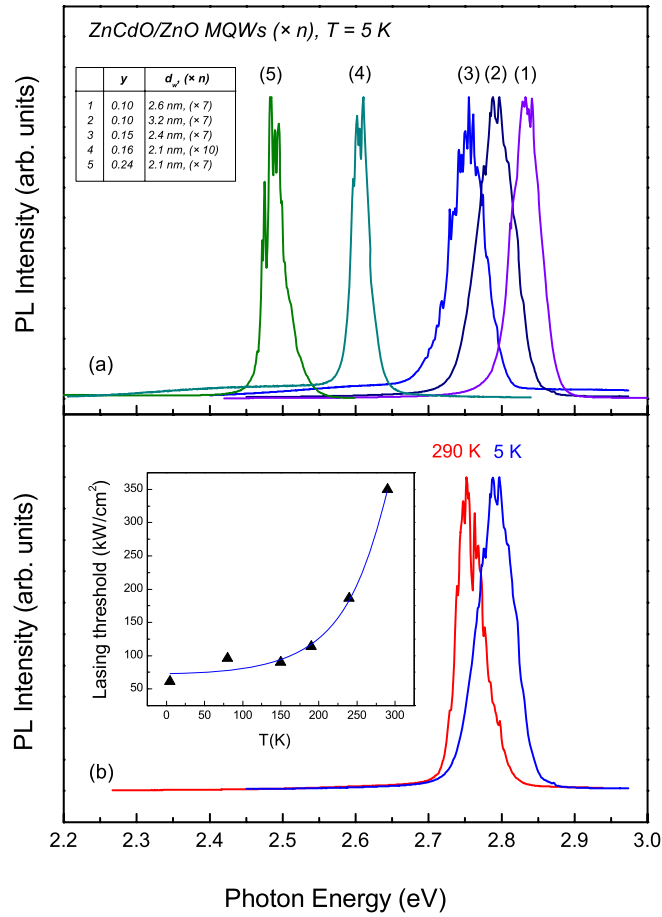


Abbildung 5.18: (a) Variation of the laser emission with structure design; (b) Change of the laser emission from low- to room temperature for structure 2, inset: temperature dependence of the threshold, line is to guide the eye.

6 Growth of ZnO-based heterostructures on ZnO wafers

Band-gap engineering using ZnMgO and ZnCdO is a central step towards optoelectronic devices based on ZnO. Epitaxial growth far from thermal equilibrium has made it possible to overcome the natural solubility limit of these ternaries and to tune the absorption edge from 2.1 to 4.4 eV [MSK⁺01, KHN⁺05, SNI⁺04, SBC⁺06b, WBC⁺06]. The substrate so far most commonly used is sapphire. Well-elaborated nucleation techniques allow for the handling of the large lattice and thermal mismatch providing hetero- and QW structures with very attractive optical properties [CKHY00, SBC⁺05, TMY⁺07, ASES⁺07]. On the other hand, further improvement of crystal perfection seems to be a prerequisite for achieving excellent optical properties, as well as reliable *p*-doping of ZnO-related materials. The potential of lattice-matched substrates for amending structural properties has been impressively shown for ScAlMgO₄ [OTS⁺99]. Recently, high quality ZnO/ZnMgO MQW structures have been fabricated on ZnO substrates [ZKH⁺07]. This Chapter presents an alternative growth scheme for the fabrication of ZnMgO and ZnCdO alloys on O-face ZnO substrates and demonstrates a dramatic improvement of their crystal quality in comparison to films grown on (11 $\bar{2}$ 0) sapphire.

The ZnO wafers used in this study¹ are grown by solidification of a melt contained in an Ir crucible employing a Bridgman technique [SGK⁺06, KGSF08]. The substrates used for epitaxial overgrowth consist of grains with sizes extending over several millimeters. The FWHM of the (0002) X-ray rocking curve of a single grain is typically about 20 arc sec. The final mechanical and chemomechanical polishing of the crystals is performed by CrysTec GmbH. The inspection of the as-received wafers by AFM reveals an atomically flat surface with residual fine scratches as the result of the polishing process. The maximal height of these scratches, however, does not exceed 1 nm. No cracks, deep scratches or other 3D defects are found, and no additional HT annealing for improving the substrate quality [ZKH⁺07, KHP⁺04, GNV⁺07] is employed. Instead, the substrates are annealed for 1 h at $T_a = 560$ °C under UHV conditions and exposed for 10 min to O-plasma prior to MBE growth.

In order to uncover directly the impact of the substrate on the structural and optical properties, similar growth recipes are applied for both ZnO and sapphire wafers. ZnMgO films are grown at $T_g = 350$ °C in slightly metal-rich conditions, as estimated from the variation of the growth rate under change of the O gas flow. After deposition,

¹Provided by Dr. Klimm, Institut für Kristallzüchtung, Berlin.

the structures are annealed for several minutes at $T_a = 560$ °C to smoothen the surface [SBC⁺05]. ZnCdO films are prepared at $T_g \sim 150$ °C in an O-excess regime [SBC⁺06b]. Only the initial nucleation step has to be specifically adapted to the substrate type. For sapphire, an about 35 nm-thick LT ($T_g = 300$ °C) layer, either ZnO (for ZnCdO) or ZnMgO (for ZnMgO), is grown first. While ZnMgO is grown directly on top of this layer, an additional 500 nm-thick ZnO buffer is introduced for ZnCdO films. In the case of ZnO substrates, a homoepitaxial nucleation step is employed. A fast surface roughening occurring at this stage during LT growth and likely related with imperfection of the interface is avoided by raising T_g to 540 °C. The ZnMgO and ZnCdO epilayers studied in what follows have a typical thickness of about 500 nm.

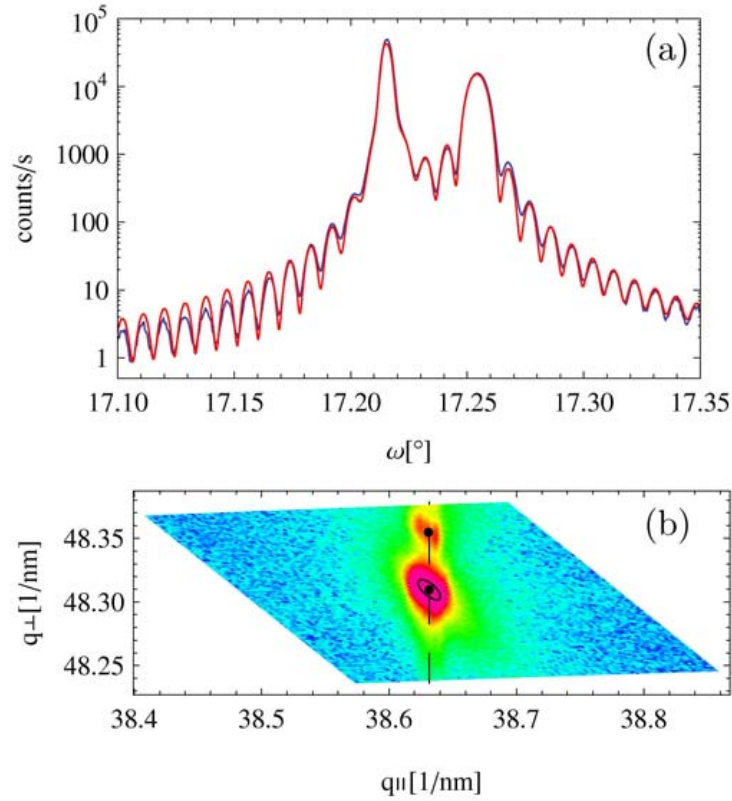


Abbildung 6.1: XRD data of a 514 nm-thick $\text{Zn}_{0.86}\text{Mg}_{0.14}\text{O}$ epilayer grown on ZnO substrate: (a) ω - 2θ scan of the (0002) diffraction peak. The black curve is the measurement, and the red curve is a simulation; (b) Reciprocal space map of the asymmetrical $(11\bar{2}4)$ reflection. The black dots depict positions of the ZnO and ZnMgO intensity maxima, black ellipse is a contour line at half maximum.

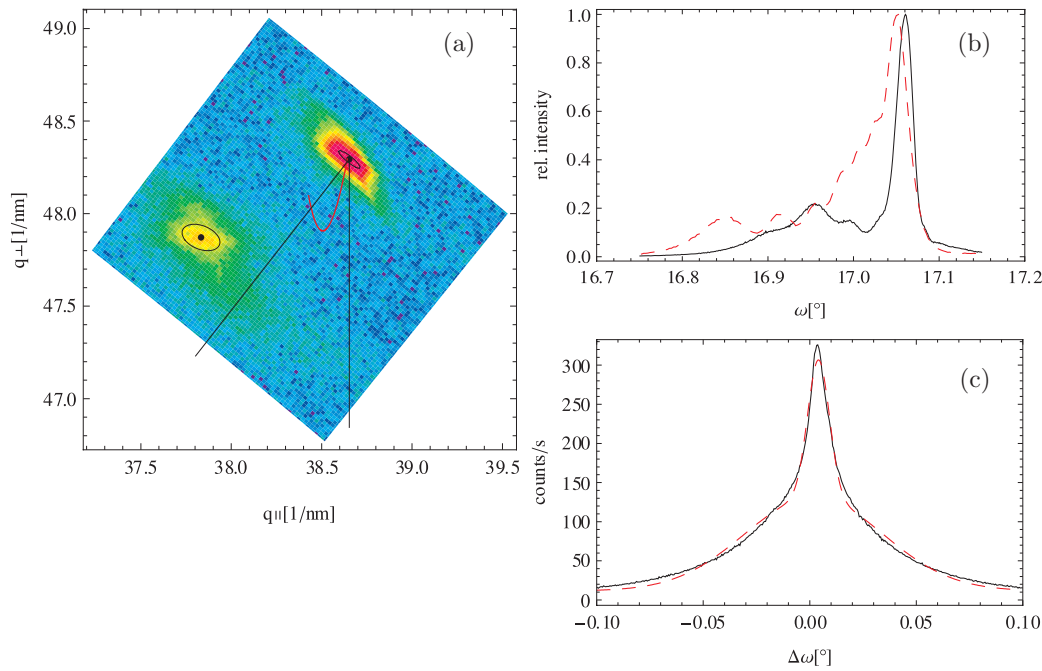


Abbildung 6.2: XRD data of a $\text{Zn}_{0.87}\text{Cd}_{0.13}\text{O}$ epilayer grown on ZnO substrate: (a) Reciprocal space map in vicinity of the $(11\bar{2}4)$ reflection. The black dots depict positions of the ZnO and ZnCdO intensity maxima, and the black ellipses are the contour lines at half maximum. The dashed lines correspond to constant lattice parameter a (vertical) or c/a ratio (inclined), respectively; red curve: $a(y) = 3.252 + 0.143y - 0.147y^2$, $c(y) = 5.204 + 0.956y - 5.42y^2$ [MSK⁺01]; (b) ω - 2θ scan of the (0002) diffraction peak (full line). The same scan for a ZnCdO film grown on sapphire is shown for comparison by the dashed line; (c) ω -rocking curve of ZnCdO (0002) diffraction peak. Dashed curve is a fit with two Gaussians.

Figure 6.1 summarizes high-resolution XRD data of a ZnMgO/ZnO film with a Mg content of $x = 0.14$. The ω - 2θ scan of the (0002) diffraction peak exhibits distinct pendellösung fringes indicating sharp interfaces and low dislocation densities [Fig. 6.1(a)]. The FWHM of the (0002) ω -rocking curve (not shown) is as small as 19 arc sec and equals the value of the ZnO substrate. In marked contrast, the rocking curve FWHM of films grown on a -plane sapphire is in the range of 600 arc sec. Identical $\vec{q}_{||}$ for the epilayer and the substrate in the reciprocal space map taken in vicinity of the asymmetrical $(11\bar{2}4)$ reflection [Fig. 6.1(b)] signify that ZnMgO is grown pseudomorphically over a thickness of 500 nm. This remains true also for a film with a Mg content of $x = 0.25$. The fact that ZnMgO is capable of pseudomorphic growth on these length scales, despite of a lattice mismatch of about 0.25 %, is related to the specific compensation of the lattice parameters change of this ternary: the in-plane length a increases, while c along the

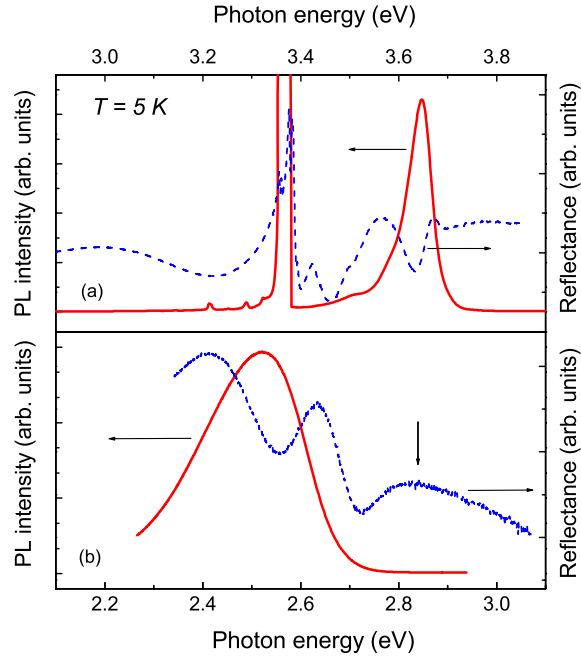


Abbildung 6.3: PL and reflectivity spectra of $\text{Zn}_{0.86}\text{Mg}_{0.14}\text{O}$ (a) and $\text{Zn}_{0.84}\text{Cd}_{0.16}\text{O}$ (b) epilayers grown on ZnO. The ZnCdO sample has been annealed for 5 hours at $T_a = 350^\circ\text{C}$ to enhance the PL efficiency. The arrow marks the excitonic ZnCdO band-gap. The PL peak positions of ZnMgO and ZnCdO layers are 3.648 and 2.522 eV, respectively.

hexagonal axis shortens, keeping thus the volume of the elementary cell almost constant [OKK⁺98]. Similar behavior has been observed for the MBE growth of ZnMgO on ZnO/sapphire templates [MTTD⁺05].

ZnCdO layers of intermediate Cd content ($y = 0.12\text{--}0.17$) grown on ZnO substrate are at least partly relaxed. The reciprocal space map of the asymmetric $(11\bar{2}4)$ reflection [Fig. 6.2(a)] exposes different \vec{q}_{\parallel} of ZnO and ZnCdO and, hence, different in-plane lattice parameters for the substrate and the film. The lack of reliable data about the lattice parameters of wurtzite CdO makes an estimate of the relaxation degree quite difficult. The ZnCdO feature in Fig. 6.2(a) is shifted to the left with respect to the line defining a constant c/a ratio. Its position does also not follow the curve suggested by experimental data for the composition range $y \leq 0.07$ [MSK⁺01], when extrapolated to higher Cd contents. Interestingly, the intensity distribution in vicinity of the ZnCdO feature spreads out most strongly in the direction perpendicular to the line $c/a = \text{const.}$, whereas composition fluctuations are expected to show up as a tail stretching along this line. Such shape of the distribution is indicative of strain inhomogeneities giving also rise to satellite structures in ω - 2θ scan of the (0002) reflection [Fig. 6.2(b)]. While present for both types of substrates, the strain-related tail is significantly reduced for

the growth on ZnO. Strongly improved crystalline perfection is also manifested by the rocking curves. The shape of the (0002) ω -scan shown in Fig. 6.2(c) is a superposition of two contributions. The broader background in the base of the curve with a FWHM of 296 arc sec is due to averaging over the substrate grain substructure imprinted into the ZnCdO film. It comprises grains that contribute less to the signal. The FWHM of the second, more narrow contribution is only 45 arc sec, as opposed to 693 arc sec for growth on sapphire. Therefore, despite the very low deposition temperature of ZnCdO, high structural quality can be achieved.

Figure 6.3 presents low-temperature optical data for films grown on ZnO. In both cases, the PL is low-energy shifted relative to the band-gap signifying localization of the carriers involved in the recombination. As is obvious, the localization is stronger for ZnCdO, probably also related to the strain inhomogeneities in this structure type. Despite the considerable structural improvement, there are no profound modifications, neither in the width nor in the PL Stokes shift, compared to epilayers grown on sapphire. Electronic localization is thus an inherent feature of both ZnMgO and ZnCdO.

In conclusion, it is demonstrated that the growth recipes developed for ZnMgO and ZnCdO on *a*- plane sapphire can be easily adapted to ZnO substrates. The resultant improvement of the crystalline quality is striking and only limited by the perfection of the substrate. While these findings might have essential implications for *p*-doping, the optical properties of the films have been found mainly determined by their ternary character.

7 Outlook

In the previous Chapters it is demonstrated that ZnO/Zn(Mg,Cd)O hetero-structures are indeed very attractive candidates for making semiconductor lasers operating in the UV and blue-green spectral range. The laser action is so far generated under optical pumping only. Already on this level, a compact device operating in the green wavelength range which is able to replace standard "green-lasers relying on frequency-doubling can be made by combining an UV GaN laser and an appropriate ZnCdO/ZnO QW structure on a single chip. The ultimate goal is of course electrical injection. Previous research established that *p*-type ZnO is difficult to achieve (see, e.g. [Loo06]). Literature survey yields, that inspired by former research on ZnSe doping, N is often used as an acceptor-type impurity. High growth temperatures are usually employed as such technique mostly suitable in GaN epitaxy. However, elevated growth temperatures obviously restrict N incorporation in the ZnO host lattice and prevent a sufficient doping level. Therefore, the attempt is made to adapt the LT growth regime introduced in the previous Chapters to achieve *p*-type doping of ZnO.

N-doped ZnO films are grown by MBE using separate radical-source cells for oxygen and nitrogen. In this way rf plasma parameters for each gas component can be independently controlled ensuring higher flexibility in comparison to rf activated NO or N₂O gases [MSK⁺04, LLS⁺05], or mixing O₂ and N₂ within one rf plasma cell [LRL⁺02]. The results of the very first experiments reveal that N incorporation is indeed strongly temperature depended. Fig. 7.1 shows SIMS data of a ZnO:N epilayer grown on *a*-plane sapphire substrate under Zn-rich conditions with fixed parameters for O₂ and N₂ radical sources. The distinct concentration steps correspond to the different growth temperatures varied in the range of $T_g = (300 - 375)^\circ\text{C}$. This demonstrates the possibility to tune the N concentration in ZnO films from $6 \cdot 10^{17}$ to $1.5 \cdot 10^{20} \text{ cm}^{-3}$ within a temperature window of only $\Delta T_g = 75^\circ\text{C}$.

Fig. 7.1 basically defines a range of the temperatures in which *p*-type material can be achieved. A typical background carrier concentration of intrinsically *n*-doped ZnO epitaxial films is about $(5 \cdot 10^{16} - 1 \cdot 10^{17}) \text{ cm}^{-3}$. Considering limited electrical activity of incorporated nitrogen due to its high acceptor ionization energy ($E_A = 170\text{-}200 \text{ meV}$ [LRL⁺02]), one has to reach N concentrations of at least $5 \cdot 10^{18} \text{ cm}^{-3}$ in order to overcompensate this level. As SIMS data provide information only about the total amount of N in the film irrespective of its chemical state and position inside the lattice, $T_g = 350^\circ\text{C}$ can be roughly considered as the upper limit. Lower temperatures increase incorporation of N but result in high resistive films and quench the PL efficiency. The resistivity of the as grown ZnO:N films is also very sensitive to light (persistent photoconductivity)

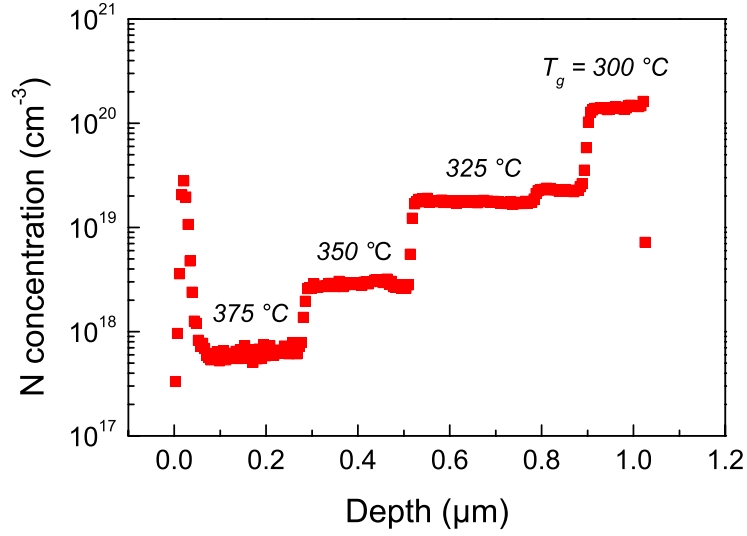


Abbildung 7.1: SIMS data (RTG Mikroanalyse GmbH, Berlin) for the ZnO:N epilayer grown at EBP (Zn) = $2.8 \cdot 10^{-7}$ Torr; O_2 : 400 W, 0.45 sccm; N_2 : 400 W, 0.18 sccm. The concentration steps correspond to the $T_g = 300$ °C, 325 °C, 350 °C and 375 °C, respectively.

indicating high density of trap centers located in the band gap. On the other hand, XRD data show still satisfactory crystalline quality for films even at very high level of N incorporation. Fig. 7.2 depicts a (0002) reciprocal space map of a ZnO:N/ZnO/sapphire structure with ZnO:N layer grown at $T_g = 270$ °C. The space map clearly displays two intensity maxima associated with different d -spacing values of the ZnO buffer (900 nm-thick) and the N-doped ZnO layer (600 nm-thick). The measured values of the c - and a -lattice constants of ZnO and ZnO:N layers are $c_{ZnO} = 5.1999$ Å, $a_{ZnO} = 3.2536$ Å, and $c_{ZnO:N} = 5.2062$ Å, $a_{ZnO:N} = 3.2547$ Å, respectively. The increase of the lattice constants with N incorporation can result from the N substitution for O (ionic radius of N^{3-} is 1.46 Å vs. 1.40 Å for O^{2-}), as well as from interstitial N. Although further study is required to verify the bonding state of N, the FWHM of the rocking curves is found to be of the same order (448 vs. 542 arc sec) for the both layers and still mainly determined by the influence of the substrate. ZnO:N layers grown in comparable regime ($T_g = 290$ °C) on ZnO wafers demonstrate the FWHM of the (0002) ω -scan as low as 17 arc sec. The reciprocal space map and the ω -2 θ scan of such sample are shown in Fig. 7.3.

The electrical properties of the films are tested by Hall-effect measurements in van der Pauw configuration. In the case of N-doped ZnO films the problem of the interface layer (see Chapter 3) becomes extremely important because it can mask the type of conductivity of the bulk layer. The contribution of the interface layer to the Hall signal can be nearly eliminated if resistivity of the NL layer is greatly enhanced, i.e. the product of $\mu_{H1}n_{H1}$ (Eq. 3.6, 3.7) is close to zero. In order to reduce the influence of the interface layer on the electrical properties the NL was heavily doped with N. A similar

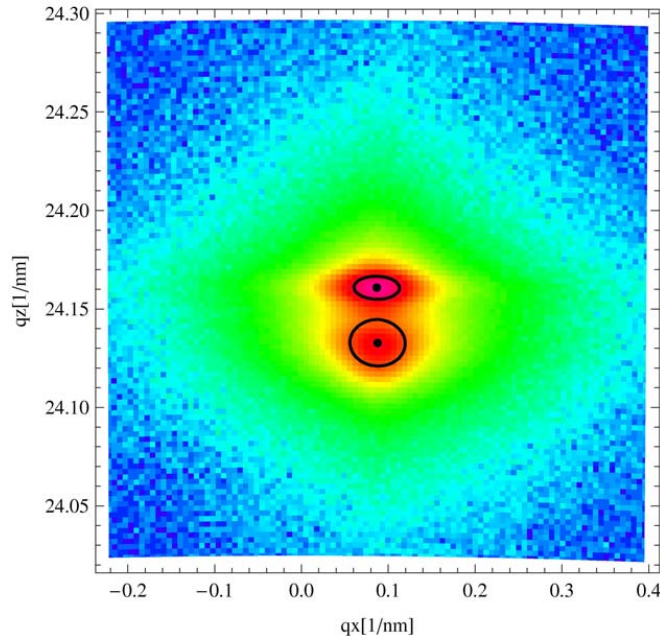


Abbildung 7.2: XRD reciprocal space map of the symmetrical (0002) reflection of a 600 nm-thick ZnO:N epilayer grown on top of a 900 nm-thick ZnO buffer. $T_g = 270^\circ\text{C}$.

procedure is also reported by *H. Tambo et al* [TYF⁺04]. ZnO films grown on such 55 nm-thick ZnO:N NL layers show room temperature mobility of (150-170) cm^2/Vs and residual carrier concentration of $n = (3-5) \cdot 10^{16} \text{ cm}^{-3}$, which are one of the best values reported so far for ZnO grown on sapphire. By N-doping at the intermediate temperatures the carrier concentration is reduced to $n = 2 \cdot 10^{15} \text{ cm}^{-3}$ with Hall mobility of $\mu = 10 \text{ cm}^2/\text{Vs}$, clearly demonstrating compensation on the some 10^{16} cm^{-3} level. However, stronger N doping currently results in highly resistive films, which either can not be reliably measured due to a noisy Hall signal or the interpretation of the results is complicated by the contribution of the NL which can not be already neglected for the high-resistive ZnO:N films. Further investigation is in progress.

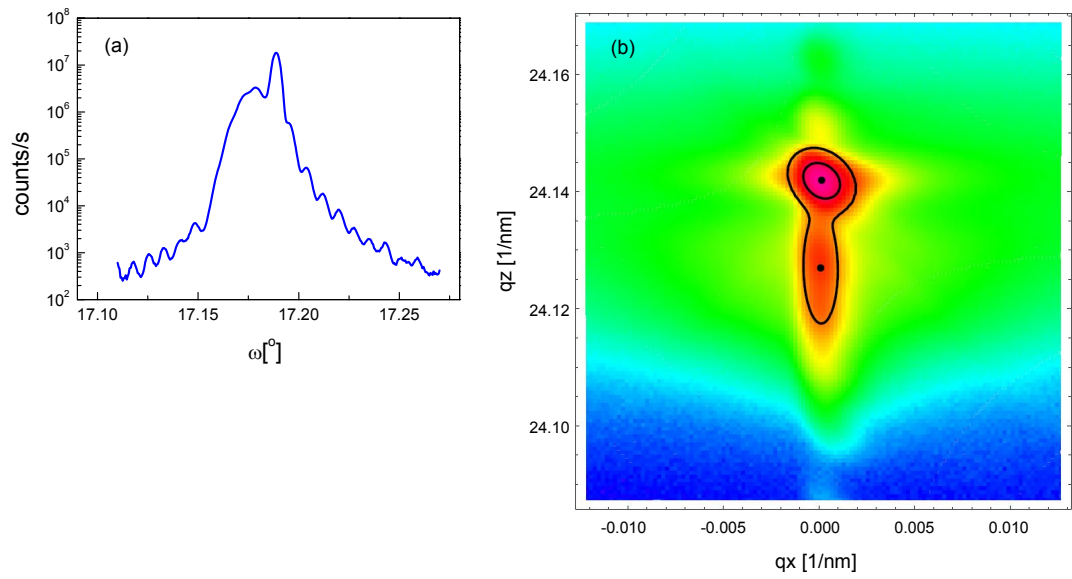


Abbildung 7.3: XRD data of the (0002) diffraction peak of a 600 nm-thick ZnO:N epilayer deposited on hydrothermally grown ZnO substrate (Crystec) at $T_g = 290^\circ\text{C}$: (a) ω - 2θ scan; (b) reciprocal space map.

8 Summary

In this work, I present novel and generally applicable growth approaches to the preparation of Group II-oxide alloys, hetero- and QW structures by radical-source MBE. The suggested principles are illustrated by numerous examples. It is shown that specifically tailored MBE regime allows one to overcome the standard solubility limit and to alloy ZnO with MgO or CdO in strict wurtzite phase up to mole fractions of several 10 %. In this way, a band-gap range from 2.2 to 4.4 eV can be covered. A clear layer-by-layer growth mode controlled by oscillations in reflection high-energy electron diffraction allows the fabrication of atomically smooth heterointerfaces and well-defined ZnO/Zn(Mg,Cd)O quantum well structures exhibiting prominent band-gap related light emission in the whole composition range. On appropriately designed structures, laser action from the UV down to green wavelengths and up to room temperature is achieved. The quality and properties of the state-of-the-art-materials are discussed in relation to the advantages for applications in various optoelectronic devices.

The main scientific results demonstrated for the first time include:

- Specific growth procedure combining LT deposition of ZnMgO and annealing at each interface to smoothen the surface;
- RHEED intensity oscillations recorded during growth of ZnMgO alloys;
- Single and multiple quantum well structures with abrupt interfaces grown on sapphire substrates;
- Laser action in ZnO/ZnMgO MQWs grown by MBE;
- MBE scheme for the preparation of wurtzite ZnCdO alloys with Cd content as high as 0.32;
- Layer-by-layer growth of ZnCdO ternaries;
- Post growth annealing step strongly enhancing the PL efficiency of ZnCdO layers;
- ZnCdO/ZnO multiple quantum well structures capable of lasing in the blue-green spectral range at room temperature;
- Growth of ZnCdO on ZnO wafers.

The results of this work are published in 14 scientific papers and presented on 16 international conferences.

Literaturverzeichnis

- [Amb98] Ambacher, O.: Growth and applications of Group III-nitrides. In: *JOURNAL OF PHYSICS D*, volume 31:pp. 2653–2710, September 1998.
- [ASESB⁺07] Al-Suleiman, M.; El-Shaer, A.; Bakin, A.; Wehmann, H.-H.; Waag, A.: Optical investigations and exciton localization in high quality $\text{Zn}_{1-x}\text{Mg}_x\text{O}$ -ZnO single quantum wells. In: *APPLIED PHYSICS LETTERS*, volume 91:p. 081911, August 2007.
- [ASSY05] Ashrafi, A. B. M. A.; Segawa, Y.; Shin, K.; Yao, T.: Nucleation and interface chemistry of ZnO deposited on 6H-SiC. In: *PHYSICAL REVIEW B*, volume 72:p. 155302, October 2005.
- [ASSY06] Ashrafi, A. B. M. A.; Segawa, Y.; Shin, K.; Yao, T.: Strain effects in ZnO layers deposited on 6H-SiC. In: *JOURNAL OF APPLIED PHYSICS*, volume 100:p. 063523, September 2006.
- [BBP⁺07] Buyanova, I. A.; Bergman, J. P.; Pozina, G.; Chen, W. M.; Rawal, S.; Norton, D. P.; Pearton, S. J.; Osinsky, A.; Dong, J. W.: Mechanism for radiative recombination in ZnCdO alloys. In: *APPLIED PHYSICS LETTERS*, volume 90:p. 261907, June 2007.
- [BCZ⁺97] Bagnall, D. M.; Chen, Y. F.; Zhu, Z.; Yao, T.; Koyama, S.; Shen, M. Y.; Goto, T.: Optically pumped lasing of ZnO at room temperature. In: *APPLIED PHYSICS LETTERS*, volume 70(17):pp. 2230–2232, April 1997.
- [BFV97] Bernardini, F.; Fiorentini, V.; Vanderbilt, D.: Spontaneous polarization and piezoelectric constants of III-V nitrides. In: *PHYSICAL REVIEW B*, volume 56:p. R10024, July 1997.
- [BGF⁺06] Bertram, F.; Giemsch, S.; Forster, D.; Christen, J.; Kling, R.; Kirchner, C.; Waag, A.: Direct imaging of phase separation in ZnCdO layers. In: *APPLIED PHYSICS LETTERS*, volume 88:p. 061915, February 2006.
- [Bra99] Braun, W.: *Applied RHEED: Reflection High-Energy Electron Diffraction During Crystal Growth*. Springer-Verlag, Berlin, 1st edition, 1999.
- [Bro57] Brown, H. E.: *ZnO Rediscovered*. The New Jersey Zinc Co., New York, 1st edition, 1957.

- [CAM⁺98] Chichibu, S. F.; Abare, A. C.; Minsky, M. S.; Keller, S.; Fleischer, S. B.; Bowers, J. E.; Hu, E.; Mishra, U. K.; Coldren, L. A.; DenBaars, S. P.; Sofa, T.: Effective band gap inhomogeneity and piezoelectric field in InGaN/GaN multiquantum well structures. In: *APPLIED PHYSICS LETTERS*, volume 73:pp. 2006–2008, November 1998.
- [CBK⁺98] Chen, Y.; Bagnall, D. M.; Koh, H.-J.; Park, K.-T.; Hiraga, K.; Zhu, Z.; Yao, T.: Plasma assisted molecular beam epitaxy of ZnO on c- plane of sapphire: Growth and characterization. In: *JOURNAL OF APPLIED PHYSICS*, volume 84(7):pp. 3912–3918, October 1998.
- [CBL⁺07] Chauveau, J.-M.; Buell, D. A.; Laügt, M.; Vennegues, P.; Teisseire-Doninelli, M.; Berard-Bergery, S.; Deparis, C.; Lo, B.; Vinter, B.; Morhain, C.: Growth of non-polar ZnO/(Zn,Mg)O quantum well structures on r-sapphire by plasma-assisted molecular beam epitaxy. In: *JOURNAL OF CRYSTAL GROWTH*, volume 301-302:pp. 366–369, December 2007.
- [Cha00] Chambers, S. A.: Epitaxial growth and properties of thin film oxides. In: *SURFACE SCIENCE REPORTS*, volume 39(5-6):pp. 105–180, August 2000.
- [CHK⁺00] Chen, Y.; Hong, S.-K.; Ko, H.-J.; Nakajima, M.; Yao, T.: Plasma-assisted molecular-beam epitaxy of ZnO epilayers on atomically flat MgAl₂O₄(111) substrates. In: *APPLIED PHYSICS LETTERS*, volume 76(2):pp. 245–247, January 2000.
- [CHK⁺01] Chen, Y.; Hong, S.-K.; Ko, H.-J.; Kirshner, V.; Wenisch, H.; Yao, T.; Inaba, K.; Segawa, Y.: Effects of an extremely thin buffer on heteroepitaxy with large lattice mismatch. In: *APPLIED PHYSICS LETTERS*, volume 78(21):pp. 3352–3354, May 2001.
- [CKH⁺00] Chen, Y.; Ko, H.-J.; Hong, S.-K.; Sekiuchi, T.; Yao, T.; Segawa, Y.: Plasma assisted molecular beam epitaxy of ZnO based II-VI semiconductor oxides and their heterostructures. In: *JOURNAL OF VACUUM SCIENCE AND TECHNOLOGY B*, volume 18(3):pp. 1514–1517, May 2000.
- [CKH⁺02] Chen, Y.; Ko, H.-J.; Hong, S.-K.; Yao, T.; Segawa, Y.: Morphology evolution of ZnO(000 $\bar{1}$) surface during plasma-assisted molecular-beam epitaxy. In: *APPLIED PHYSICS LETTERS*, volume 80(8):pp. 1358–1360, February 2002.
- [CKHY00] Chen, Y.; Ko, H.-J.; Hong, S.-K.; Yao, T.: Layer-by-layer growth of ZnO epilayer on Al₂O₃(0001) by using a MgO buffer layer. In: *APPLIED PHYSICS LETTERS*, volume 76(5):pp. 559–561, January 2000.
- [CP85] Chang, L. L.; Ploog, K.: *Molecular Beam Epitaxy and Heterostructures*. Martinus Nijhoff Publishers, Dordrecht, The Netherlands, 1st edition, 1985.

- [CRL⁺05] Chen, J.; Ren, F.; Li, Y.; Norton, D. P.; Pearton, S. J.; Osinsky, A.; Dong, J. W.; Chow, P. P.; Weaver, J. F.: Measurement of Zn_{0.95}Cd_{0.05}O/ZnO(0001) heterojunction band offsets by x-ray photoelectron spectroscopy. In: *APPLIED PHYSICS LETTERS*, volume 87:p. 192106, November 2005.
- [CSB⁺06] Cui, J.; Sadofev, S.; Blumstengel, S.; Puls, J.; Henneberger, F.: Optical gain and lasing of ZnO/ZnMgO multiple quantum wells: From low to room temperature. In: *APPLIED PHYSICS LETTERS*, volume 89:p. 051108, August 2006.
- [DIBM99] Doppalapudi, D.; Iliopoulos, E.; Basu, S. N.; Moustakas, T. D.: Epitaxial growth of gallium nitride films on A-plane sapphire by molecular beam epitaxy. In: *JOURNAL OF APPLIED PHYSICS*, volume 85(7):pp. 3582–3589, April 1999.
- [DOM⁺00] Dietl, T.; Ohno, H.; Matsukura, F.; Cibert, J.; Ferrand, D.: Zener model description of ferromagnetism in zinc-blende magnetic semiconductors. In: *SCIENCE*, volume 287:pp. 1019–1022, February 2000.
- [dW00] de Walle, C. G. Van: Hydrogen as a cause of doping in Zinc Oxide. In: *PHYSICAL REVIEW LETTERS*, volume 85:pp. 1012–1015, July 2000.
- [EBW⁺04] Edmonds, K. W.; Bogusławski, P.; Wang, K. Y.; Campion, P. R.; Novikov, S. N.; Farley, N. R. S.; Gallagher, B. L.; Foxon, C. T.; Sawicki, M.; Dietl, T.; Nardelli, M. Buongiorno; Bernholc, J.: Residual native shallow donor in ZnO. In: *PHYSICAL REVIEW LETTERS*, volume 92:p. 037201, January 2004.
- [ESBM⁺06] El-Shaer, A.; Bakin, A.; Mofor, A. C.; Bläsing, J.; Krost, A.; Stoimenos, J.; Pecz, B.; Kreye, M.; Heuken, M.; Waag, A.: CBE growth of high-quality ZnO epitaxial layers. In: *PHYSICA STATUS SOLIDI B*, volume 243(4):pp. 768–772, March 2006.
- [FIY⁺00] Fons, P.; Iwata, K.; Yamada, A.; Matsubara, K.; Niki, S.; Nakahara, K.; Tanabe, T.; Takasu, H.: Uniaxial locked epitaxy of ZnO on the *a*- face of sapphire. In: *APPLIED PHYSICS LETTERS*, volume 77(12):pp. 1801–1803, September 2000.
- [GAC⁺08] Guo, W.; Allenic, A.; Chen, Y. B.; Pan, X. Q.; Tian, W.; Adamo, C.; Schlom, D. G.: ZnO epilayers on (111) Si using epitaxial Lu₂O₃ bufer layers. In: *APPLIED PHYSICS LETTERS*, volume 92:p. 072101, February 2008.
- [GKK⁺03] Gruber, Th.; Kirchner, C.; Kling, R.; Reuss, F.; Waag, A.; Bertram, F.; Forster, D.; Christen, J.; Schreck, M.: Optical and structural analysis of ZnCdO layers grown by metalorganic vapor-phase epitaxy. In: *APPLIED PHYSICS LETTERS*, volume 83(16):pp. 3290–3292, October 2003.

- [GKK⁺04] Gruber, Th.; Kirchner, C.; Kling, R.; Reuss, F.; Waag, A.: ZnMgO epilayers and ZnO-ZnMgO quantum wells for optoelectronic applications in the blue and UV spectral region. In: *APPLIED PHYSICS LETTERS*, volume 84(26):pp. 5359–5361, June 2004.
- [GNV⁺07] Graubner, S.; Neumann, C.; Volbers, N.; Meyer, B. K.; Bläsing, J.; Krost, A.: Preparation of ZnO substrates for epitaxy: Structural, surface, and electrical properties. In: *APPLIED PHYSICS LETTERS*, volume 90:p. 042103, January 2007.
- [GS06] Gopal, P.; Spaldin, N. A.: Polarization, piezoelectric constants, and elastic constants of ZnO, MgO, and CdO. In: *JOURNAL OF ELECTRONIC MATERIALS*, volume 35(4):pp. 538 – 542, April 2006.
- [HGH⁺95] Hoffmann, N.; Griesche, J.; Heimbrodt, W.; Weinhold, V.; Jacobs, K.: Reflection high-energy electron diffraction controlled growth of Zn-Se/(Zn,Mn)Se quantum well structures. In: *JOURNAL OF CRYSTAL GROWTH*, volume 146:pp. 422 – 426, January 1995.
- [Hur94] Hurle, D.T.J.: *Handbook of crystal growth 3. Thin films and epitaxy. Part B: Growth mechanisms and dynamics*. Elsevier Science B.V., Amsterdam, 1st edition, 1994.
- [IFN⁺00a] Iwata, K.; Fons, P.; Niki, S.; Yamada, A.; Matsubara, K.; Nakahara, K.; Takasu, H.: Improvement of electrical properties in ZnO thin films grown by radical source (RS) - MBE. In: *PHYSICA STATUS SOLIDI (a)*, volume 180:pp. 287–292, July 2000.
- [IFN⁺00b] Iwata, K.; Fons, P.; Niki, S.; Yamada, A.; Matsubara, K.; Nakahara, K.; Tanabe, T.; Takasu, H.: ZnO growth on Si by radical source MBE. In: *JOURNAL OF CRYSTAL GROWTH*, volume 214/215:pp. 50–54, July 2000.
- [IKO⁺98] Im, J. S.; Kollmer, H.; Off, J.; Sohmer, A.; Scholz, F.; Hangleiter, A.: Reduction of oscillator strength due to piezoelectric fields in GaN/Al_xGa_{1-x}N quantum wells. In: *PHYSICAL REVIEW B*, volume 57:p. R9435, July 1998.
- [JJ04] Joyce, B. A.; Joyce, T. B.: Basic studies of molecular beam epitaxy - past, present and some future directions. In: *JOURNAL OF CRYSTAL GROWTH*, volume 264:pp. 605–619, December 2004.
- [JSdW06] Janotti, A.; Segev, D.; de Walle, C. G. Van: Effects of cation d states on the structural and electronic properties of III-nitride and II-oxide wide-band-gap semiconductors. In: *PHYSICAL REVIEW B*, volume 74:p. 045202, July 2006.
- [KCMdW00] Kohan, A. F.; Ceder, G.; Morgan, D.; de Walle, Chris G. Van: First-principles study of native point defects in ZnO. In: *PHYSICAL REVIEW B*, volume 61:pp. 15019 – 15027, June 2000.

- [KCZ⁺00] Ko, H. J.; Chen, Y. F.; Zhu, Z.; Yao, T.; Kobayashi, I.; Uchiki, H.: Photoluminescence properties of ZnO epilayers grown on CaF₂(111) by plasma assisted molecular beam epitaxy. In: *APPLIED PHYSICS LETTERS*, volume 76:pp. 1905–1907, April 2000.
- [KFK⁺07] Kojima, K.; Funato, M.; Kawakami, Y.; Masui, S.; Nagahama, S.; Mukai, T.: Stimulated emission at 474 nm from an InGaN laser diode structure grown on a (11 $\bar{2}$ 2) GaN substrate. In: *APPLIED PHYSICS LETTERS*, volume 91:p. 251107, April 2007.
- [KGSF08] Klimm, D.; Ganschow, S.; Schulz, D.; Fornari, R.: The growth of ZnO crystals from the melt. In: *JOURNAL OF CRYSTAL GROWTH*, volume 310:pp. 3009–3013, June 2008.
- [KHN⁺04] Koike, K.; Hama, K.; Nakashima, I.; Takada, G.; Ozaki, M.; Ogata, K.; Sasa, S.; Inoue, M.; Yano, M.: Piezoelectric carrier confinement by lattice mismatch at ZnO/Zn_{0.6}Mg_{0.4}O heterointerface. In: *JAPANESE JOURNAL OF APPLIED PHYSICS*, volume 43:pp. L1372 – L1375, October 2004.
- [KHN⁺05] Koike, K.; Hama, K.; Nakashima, I.; Takada, G.-Y.; Ogata, K.; Sasa, S.; Inoue, M.; Yano, M.: Molecular beam epitaxial growth of wide bandgap ZnMgO alloy films on (111)-oriented Si substrate toward UV-detector applications. In: *JOURNAL OF CRYSTAL GROWTH*, volume 278:pp. 288–292, February 2005.
- [KHP⁺04] Ko, H.-J.; Hana, M.-S.; Park, Y.-S.; Yu, Y.-S.; Kim, B.-I.; Kim, S. S.; Kim, J.-H.: Improvement of the quality of ZnO substrates by annealing. In: *JOURNAL OF CRYSTAL GROWTH*, volume 269:pp. 493–498, September 2004.
- [KKO⁺04] Koike, K.; Komuro, T.; Ogata, K.; Sasa, S.; Inoue, M.; Yano, M.: CaF₂ growth as a buffer layer of ZnO/Si heteroepitaxy. In: *PHYSICA E*, volume 21:pp. 679–683, February 2004.
- [Kli07] Klingshirn, C.: ZnO: From basics towards applications. In: *PHYSICA STATUS SOLIDI (b)*, volume 244(9):pp. 3027–3073, July 2007.
- [KMSY04] Kato, H.; Miyamoto, K.; Sano, M.; Yao, T.: Polarity control of ZnO on sapphire by varying the MgO buffer layer thickness. In: *APPLIED PHYSICS LETTERS*, volume 84(22):pp. 4562–4564, May 2004.
- [KNH⁺05] Koike, K.; Nakashima, I.; Hashimoto, K.; Sasa, S.; Inoue, M.; Yano, M.: Characteristics of a Zn_{0.7}Mg_{0.3}O/ZnO heterostructure field-effect transistor grown on sapphire substrate by molecular-beam epitaxy. In: *APPLIED PHYSICS LETTERS*, volume 87:p. 112106, September 2005.
- [Kof76] Koffyberg, F. P.: Thermoreflectance spectra of CdO: Band gaps and band-population effects. In: *PHYSICAL REVIEW B*, volume 13:pp. 4470–4476, May 1976.

- [KSMY03] Kato, H.; Sano, M.; Miyamoto, K.; Yao, T.: Effect of O/Zn flux ratio on crystalline quality of ZnO films grown by plasma-assisted molecular beam epitaxy. In: *JAPANESE JOURNAL OF APPLIED PHYSICS*, volume 42(4B):pp. 2241–2244, April 2003.
- [LDT⁺07] Lutsenko, E. V.; Danilchuk, A. V.; Tarasuk, N. P.; Pavlovskii, V. N.; Gurskii, A. L.; Yablonskii, G. P.; L. Rahimzadeh Khoshroo, H. Kalisch; Jansen, R. H.; Dikme, Y.; Schineller, B.; Heuken, M.: Optically pumped InGaN/GaN MQW lift-off lasers grown on silicon substrates. In: *SUPERLATTICES AND MICROSTRUCTURES*, volume 41:pp. 400–406, December 2007.
- [LE02] Liu, L.; Edgar, J. H.: Substrates for gallium nitride epitaxy. In: *MATERIALS SCIENCE AND ENGINEERING R*, volume 37:pp. 61–127, December 2002.
- [LFR⁺05] Look, D. C.; Farlow, G. C.; Reunchan, P.; Limpijumnong, S.; Zhang, S. B.; Nordlund, K.: Evidence for native-defect donors in n-type ZnO. In: *PHYSICAL REVIEW LETTERS*, volume 95:p. 225502, November 2005.
- [LHS99] Look, D. C.; Hemsley, J. W.; Sizelove, J. R.: Residual native shallow donor in ZnO. In: *PHYSICAL REVIEW LETTERS*, volume 82:pp. 2552–2555, March 1999.
- [Lid94] Lide, D. R.: *CRC Handbook of Chemistry and Physics*. Chemical Rubber, Boca Raton, FL, 74th edition, 1994.
- [LLS⁺05] Liang, H. W.; Lu, Y. M.; Shen, D. Z.; Liu, Y. C.; Yan, J. F.; Shan, C. X.; Li, B. H.; Zhang, Z. Z.; Zhang, J. Y.; Fan, X. W.: P-type ZnO thin films prepared by plasma molecular beam epitaxy using radical NO. In: *PHYSICA STATUS SOLIDI A*, volume 202:pp. 1060–1065, March 2005.
- [LM97] Look, D. C.; Molnar, R. J.: Degenerate layer at GaN/sapphire interface: Influence on Hall-effect measurements. In: *APPLIED PHYSICS LETTERS*, volume 70:pp. 3377–3379, June 1997.
- [LMG⁺01] Lefebvre, P.; Morel, A.; Gallart, M.; Taliercio, T.; Allégre, J.; Gil, B.; Mathieu, H.; Damilano, B.; Grandjean, N.; Massies, J.: High internal electric field in a graded-width InGaN/GaN quantum well: Accurate determination by time-resolved photoluminescence spectroscopy. In: *APPLIED PHYSICS LETTERS*, volume 78:pp. 1252–1254, September 2001.
- [Loo06] Look, D. C.: Progress in ZnO Materials and Devices. In: *JOURNAL OF ELECTRONIC MATERIALS*, volume 35(6):pp. 1299–1305, June 2006.
- [LRL⁺02] Look, D. C.; Reynolds, D. C.; Litton, C. W.; Eason, D. B.; Cantwell, G.: Characterization of homoepitaxial p-type ZnO grown by molecular beam epitaxy. In: *APPLIED PHYSICS LETTERS*, volume 81:pp. 1830–1832, September 2002.

- [LSKN01] Lim, S.-H.; Shindo, D.; Kang, H.-B.; Nakamura, K.: Study of defects and interfaces in epitaxial ZnO films grown on (11 $\bar{2}$ 0) Al₂O₃ grown by electron cyclotron resonance-assisted molecular beam epitaxy. In: *JOURNAL OF CRYSTAL GROWTH*, volume 225:pp. 202–207, December 2001.
- [Mar67] Margrave, J.: *The Characterization of High Temperature Vapors*. John Wiley and Sons, New York, 1st edition, 1967.
- [MBL⁺05] Morhain, C.; Bretagnon, T.; Lefebvre, P.; Tang, X.; Valvin, P.; Guillet, T.; Gil, B.; Taliercio, T.; Teisseire-Doninelli, M.; Vinter, B.; Deparis, C.: Internal electric field in wurtzite ZnO/Zn_{0.78}Mg_{0.22}O quantum wells. In: *PHYSICAL REVIEW B*, volume 72:p. 241305(R), December 2005.
- [MCT⁺00] Makino, T.; Chia, C. H.; Tuan, Nguen T.; Sun, H. D.; Segawa, Y.; Kawasaki, M.; Ohtomo, A.; Tamura, K.; Koinuma, H.: Room-temperature luminescence of excitons in ZnO/(Mg,Zn)O multiple quantum wells on lattice-matched substrates. In: *APPLIED PHYSICS LETTERS*, volume 77(7):pp. 975–977, August 2000.
- [MMJ⁺99] Matsumoto, Y.; Murakami, M.; Jin, Z.; Ohtomo, A.; Lippmaa, M.; Kawasaki, M.; Koinuma, H.: Combinatorial laser molecular beam epitaxy (MBE) growth of Mg-Zn-O alloy for band gap engineering. In: *JAPANESE JOURNAL OF APPLIED PHYSICS*, volume 38(6A/B):pp. L603–L605, June 1999.
- [MSH⁺05] Meyer, B. K.; Sann, J.; Hofmann, D. M.; Neumann, C.; Zeuner, A.: Shallow donors and acceptors in ZnO. In: *SEMICONDUCTOR SCIENCE AND TECHNOLOGY*, volume 20:pp. S62 – S66, March 2005.
- [MSK⁺01] Makino, T.; Segawa, Y.; Kawasaki, M.; Ohtomo, A.; Shiroki, R.; Tamura, K.; Yasuda, T.; Koinuma, H.: Band gap engineering based on Mg_xZn_{1-x}O and Cd_yZn_{1-y}O ternary alloy films. In: *APPLIED PHYSICS LETTERS*, volume 78(9):pp. 1237–1239, February 2001.
- [MSK⁺04] Matsui, H.; Saeki, H.; Kawai, T.; Tabata, H.; Mizobuchi, B.: N doping using N₂O and NO sources: From the viewpoint of ZnO. In: *JOURNAL OF APPLIED PHYSICS*, volume 95(10):pp. 5882–5888, May 2004.
- [MSKK05] Makino, T.; Segawa, Y.; Kawasaki, M.; Koinuma, H.: Optical properties of excitons in ZnO-based quantum well heterostructures. In: *SEMICONDUCTOR SCIENCE AND TECHNOLOGY*, volume 20:pp. S78 – S91, March 2005.
- [MTTD⁺05] Morhain, C.; Tang, X.; Teisseire-Doninelli, M.; Lo, B.; Laugt, M.; Chauveau, J.-M.; Vinter, B.; Tottereau, O.; Vennegues, P.; Deparis, C.; Neu, G.: Structural and electronic properties of ZnMgO/ZnO quantum wells. In: *SUPERLATTICES AND MICROSTRUCTURES*, volume 38:pp. 455–463, December 2005.

- [NF03] Nickel, N. H.; Fleisher, K.: Hydrogen local vibrational modes in Zinc Oxide. In: *PHYSICAL REVIEW LETTERS*, volume 90:p. 197402, May 2003.
- [NKB01] Nahhas, A.; Kim, H.-K.; Blachere, J.: Epitaxial growth of ZnO films Si substrates using an epitaxial GaN buffer. In: *APPLIED PHYSICS LETTERS*, volume 78(11):pp. 1511–1513, January 2001.
- [NPC⁺06] Narayan, J.; Pant, P.; Chugh, A.; Choi, H.; Fan, J. C. C.: Characteristics of nucleation layer and epitaxy in GaN/sapphire heterostructures. In: *JOURNAL OF APPLIED PHYSICS*, volume 99:p. 054313, March 2006.
- [NTT⁺01] Nakahara, K.; Tanabe, T.; Takasu, H.; Fons, P.; Iwata, K.; Yamada, A.; Matsubara, K.; Hunger, R.; Niki, S.: Growth of undoped ZnO films with improved electrical properties by radical source molecular beam epitaxy. In: *JAPANESE JOURNAL OF APPLIED PHYSICS*, volume 1:pp. 250 – 254, January 2001.
- [ÖAL⁺05] Özgür, Ü.; Alivov, Ya. I.; Liu, C.; Teke, A.; Reshchikov, M. A.; Dogan, S.; Avrutin, V.; Cho, S.-J.; Morkoç, H.: A comprehensive review of ZnO materials and devices. In: *JOURNAL OF APPLIED PHYSICS*, volume 98:p. 041301, August 2005.
- [OKK⁺98] Ohtomo, A.; Kawasaki, M.; Koida, T.; Masubuchi, M.; Koinuma, H.; Sakurai, Y.; Yoshida, Y.; Yasuda, T.; Segawa, Y.: $\text{Mg}_x\text{Zn}_{1-x}\text{O}$ as a II-VI widegap semiconductor alloy. In: *APPLIED PHYSICS LETTERS*, volume 72(19):pp. 2466–2468, May 1998.
- [OKO⁺99] Ohtomo, A.; Kawasaki, M.; Ohkubo, I.; Koinuma, H.; Yasuda, T.; Segawa, Y.: Structure and optical properties of ZnO/ $\text{Mg}_{0.2}\text{Zn}_{0.8}\text{O}$ superlattices. In: *APPLIED PHYSICS LETTERS*, volume 75(17):pp. 980–982, August 1999.
- [OKS⁺98a] Ohtomo, A.; Kawasaki, M.; Sakurai, Y.; Ohkubo, I.; Shiroki, R.; Yoshida, Y.; Yasuda, T.; Segawa, Y.; Koinuma, H.: Fabrication of alloys and superlattices based on ZnO towards ultraviolet laser. In: *MATERIALS SCIENCE AND ENGINEERING B*, volume 56:pp. 263–266, November 1998.
- [OKS⁺98b] Ohtomo, A.; Kawasaki, M.; Sakurai, Y.; Yoshida, Y.; Koinuma, H.; Yu, P.; Tang, Z. K.; Wong, G. K. L.; Segawa, Y.: Room temperature ultraviolet laser emission from ZnO nanocrystal thin films grown by laser MBE. In: *MATERIALS SCIENCE AND ENGINEERING B*, volume 54:pp. 24–28, June 1998.
- [OKT⁺03] Ogata, K.; Koike, K.; Tanibe, T.; Komuro, T.; Yan, F.; Sasa, S.; Inoue, M.; Yano, M.: ZnO and ZnMgO growth on a-plane sapphire by molecular beam epitaxy. In: *JOURNAL OF CRYSTAL GROWTH*, volume 251:pp. 623–627, April 2003.

- [ONI⁺01] Oba, F.; Nishitani, S. R.; Isotani, S.; Adachi, H.; Tanaka, I.: Energetics of native defects in ZnO. In: *JOURNAL OF APPLIED PHYSICS*, volume 90:pp. 824–828, April 2001.
- [OSO⁺99] Ohtomo, A.; Shiroki, R.; Ohkubo, I.; Koinuma, H.; Kawasaki, M.: Thermal stability of supersaturated $\text{Mg}_x\text{Zn}_{1-x}\text{O}$ alloy films and $\text{Mg}_x\text{Zn}_{1-x}\text{O}/\text{ZnO}$ heterointerfaces. In: *APPLIED PHYSICS LETTERS*, volume 75(26):pp. 4088–4090, December 1999.
- [OT05] Ohtomo, A.; Tsukazaki, A.: Pulsed laser deposition of thin films and superlattices based on ZnO. In: *SEMICONDUCTOR SCIENCE AND TECHNOLOGY*, volume 20:pp. S1–S12, November 2005.
- [OTK⁺00] Ohtomo, A.; Tamura, K.; Kawasaki, M.; Makino, T.; Segawa, Y.; Tang, Z. K.; Wong, G. K. L.; Matsumoto, Y.; Koinuma, H.: Room-temperature stimulated emission of excitons in $\text{ZnO}/(\text{Mg,Zn})\text{O}$ superlattices. In: *APPLIED PHYSICS LETTERS*, volume 77(14):pp. 2204–2206, October 2000.
- [OTS⁺99] Ohtomo, A.; Tamura, K.; Saikusa, K.; Takahashi, K.; Makino, T.; Segawa, Y.; Koinuma, H.; Kawasaki, M.: Single crystalline ZnO films grown on lattice-matched $\text{ScAlMgO}_4(0001)$ substrates. In: *APPLIED PHYSICS LETTERS*, volume 75(17):pp. 2635–2637, August 1999.
- [PESB⁺06] Pecz, B.; El-Shaer, A.; Bakin, A.; Mofor, A.-C.; Waag, A.; Stoemenos, J.: Structural characterization of ZnO films grown by molecular beam epitaxy on sapphire with MgO buffer. In: *JOURNAL OF APPLIED PHYSICS*, volume 100:p. 103506, November 2006.
- [PTR⁺90] Park, R. M.; Troffer, M. B.; Rouleau, C. M.; DePuydt, J. M.; Haase, A.: P-type ZnSe by nitrogen atom beam doping during molecular beam epitaxial growth. In: *APPLIED PHYSICS LETTERS*, volume 57(20):pp. 2127–2129, November 1990.
- [RLH98] Rabe, M.; Lowisch, M.; Henneberger, F.: Self-assembled CdSe quantum dots formation by thermally activated surface reorganization. In: *JOURNAL OF CRYSTAL GROWTH*, volume 184/185:pp. 248–253, February 1998.
- [SBC⁺05] Sadofev, S.; Blumstengel, S.; Cui, J.; Puls, J.; Rogaschewski, S.; Schäfer, P.; Sadofyev, Yu. G.; Henneberger, F.: Growth of high-quality ZnMgO epilayers and ZnO/ZnMgO quantum well structures by radical-source molecular-beam epitaxy on sapphire. In: *APPLIED PHYSICS LETTERS*, volume 87:p. 091903, August 2005.
- [SBC⁺06a] Sadofev, S.; Blumstengel, S.; Cui, J.; Puls, J.; Henneberger, F.; Schneider, R.; Litvinov, D.; Gerthsen, D.: Uniform and efficient UV-emitting

- ZnO/ZnMgO multiple quantum wells grown by radical-source molecular beam epitaxy. In: *JAPANESE JOURNAL OF APPLIED PHYSICS*, volume 45(47):pp. L1250–L1252, November 2006.
- [SBC⁺06b] Sadofev, S.; Blumstengel, S.; Cui, J.; Puls, J.; Rogaschewski, S.; Schäfer, P.; Henneberger, F.: Visible band-gap ZnCdO heterostructures grown by molecular-beam epitaxy. In: *APPLIED PHYSICS LETTERS*, volume 89:p. 201907, December 2006.
- [SBH04] Sadofev, S.; Blumstengel, S.; Henneberger, F.: Formation of CdSe quantum dots on homoepitaxial ZnSe. In: *APPLIED PHYSICS LETTERS*, volume 84(18):pp. 3678–3680, May 2004.
- [SCH⁺01] Spruytte, S. G.; Coldren, C. W.; Harris, J. S.; Wampler, W.; Krispin, P.; Ploog, K.; Larson, M. C.: Incorporation of nitrogen in nitride-arsenides: Origin of improved luminescence efficiency after anneal. In: *JOURNAL OF APPLIED PHYSICS*, volume 89:p. 4401, April 2001.
- [SFG⁺98] Smith, A. R.; Feenstra, R. M.; Greve, D. W.; Shin, M.-S.; Skowronski, M.; Neugebauer, J.; Northrup, J. E.: Determination of wurtzite GaN lattice polarity based on surface reconstruction. In: *APPLIED PHYSICS LETTERS*, volume 72(17):pp. 2114–2116, April 1998.
- [SFO⁺84] Sakamoto, T.; Funabashi, H.; Ohta, K.; Nakagawa, T.; Kawai, N. J.; Kojima, T.: Phase-locked epitaxy using RHEED intensity oscillation. In: *JAPANESE JOURNAL OF APPLIED PHYSICS*, volume 23(9):pp. L657–L659, September 1984.
- [SGK⁺06] Schulz, D.; Ganschow, S.; Klimm, D.; Neubert, M.; Roßberg, Matthias; Schmidbauer, M.; Fornari, R.: Bridgman-grown zinc oxide single crystals. In: *JOURNAL OF CRYSTAL GROWTH*, volume 296:pp. 27–30, September 2006.
- [SKH59] Sarver, J. F.; Katnack, Fred. L.; Hummel, F. A.: Phase equilibria and manganese-activated fluorescence in the system $\text{Zn}_3(\text{PO}_4)_2\text{-Mg}_3(\text{PO}_4)_2$. In: *JOURNAL OF THE ELECTROCHEMICAL SOCIETY*, volume 106(11):pp. 960–963, November 1959.
- [SKK⁺00] Sakurai, K.; Kubo, T.; Kajita, D.; Tanabe, T.; Takasu, H.; Fujita, Shizuo; Fujita, Shigeo: Blue photoluminescence from ZnCdO films grown by molecular beam epitaxy. In: *JAPANESE JOURNAL OF APPLIED PHYSICS*, volume 39(11B):pp. L1146–L1148, November 2000.
- [SKY01] Sato, K.; Katayama-Yoshida, H.: Electronic structure and ferromagnetism of transition-metal-impurity-doped zinc oxide. In: *PHISICA B*, volume 308 - 310:pp. 904–907, December 2001.

- [SML⁺04] Strezhemechny, Y. M.; Mosbaker, H. L.; Look, D. C.; Reynolds, D. C.; Litton, C. W.; Garces, N. Y.; Giles, N. C.; Halliburton, L. E.; Niki, S.; Brillson, L. J.: Remote hydrogen plasma doping of single crystal ZnO. In: *APPLIED PHYSICS LETTERS*, volume 84(14):pp. 2545–2547, April 2004.
- [SNI⁺04] Shigemori, S.; Nakamura, A.; Ishihara, J.; Aoki, T.; Temmyo, J.: Zn_{1-x}Cd_xO film growth using remote plasma-enhanced metalorganic chemical vapor deposition. In: *JAPANESE JOURNAL OF APPLIED PHYSICS*, volume 43(8B):pp. L1088–L1090, July 2004.
- [SNM⁺99] Sharma, A. K.; Narayan, J.; Muth, J. F.; Teng, C. W.; Jin, C.; Kvit, A.; Kolbas, R. M.; Holland, O. W.: Optical and structural properties of epitaxial Mg_xZn_{1-x}O alloys. In: *APPLIED PHYSICS LETTERS*, volume 75(21):pp. 3327–3329, November 1999.
- [STL⁺07] Shubina, T. V.; Toropov, A. A.; Lublinskaya, O. G.; Kop'ev, P. S.; Ivanov, S. V.; El-Shaer, A.; Al-Suleiman, M.; Bakin, A.; Waag, A.; Voinilovich, A.; Lutsenko, E. V.; Yablonskii, G. P.; Bergman, J. P.; Pozina, G.; Monemar, B.: Recombination dynamics and lasing in ZnO/ZnMgO single quantum well structures. In: *APPLIED PHYSICS LETTERS*, volume 91:p. 201104, November 2007.
- [SVC⁺04] Setiawan, A.; Vashaei, Z.; Cho, M. Whan; Yao, T.; Kato, H.; Sano, M.; Miyamoto, K.; Yonenaga, I.; Ko, H. Ju: Characteristics of dislocations in ZnO layers grown by plasma-assisted molecular beam epitaxy under different Zn/O flux ratios. In: *JOURNAL OF APPLIED PHYSICS*, volume 96(7):pp. 3763–3767, October 2004.
- [TCC⁺04] Tang, X.; Clauzonnier, A.; Campbell, H. I.; Prior, K. A.; Cavenett, B. C.: Electrical characterization of zinc oxide thin films by electrochemical capacitance-voltage profiling. In: *APPLIED PHYSICS LETTERS*, volume 84(16):pp. 3043–3045, April 2004.
- [Tew73] Tewari, S.: The electronic bandstructure of CdO by the augmented plane wave method. In: *SOLID STATE COMMUNICATIONS*, volume 12:pp. 437–441, March 1973.
- [TMY⁺07] Tampo, H.; Matsubara, K.; Yamada, A.; Shibata, H.; Fons, P.; Yamagata, M.; Kanie, H.; Niki, S.: High electron mobility Zn polar ZnMgO/ZnO heterostructures grown by molecular beam epitaxy. In: *JOURNAL OF CRYSTAL GROWTH*, volume 301-302:pp. 358–361, March 2007.
- [TOO⁺05] Tsukazaki, A.; Ohtomo, A.; Onuma, T.; Ohtani, M.; Makino, T.; Sumiya, M.; Ohtani, K.; Chichibu, S. F.; Fuke, S.; Segawa, Y.; Ohno, H.; Koinuma, H.; Kawasaki, M.: Repeated temperature modulation epitaxy for p-type doping and light-emitting diode based on ZnO. In: *NATURE MATERIALS*, volume 4:pp. 42–46, January 2005.

- [TYF⁺04] Tampo, H.; Yamada, A.; Fons, P.; Shibata, H.; Matsubara, K.; Iwata, K.; Niki, S.; Nakahara, K.; Takasu, H.: Degenerate layer in epitaxial ZnO films grown on sapphire substrates. In: *APPLIED PHYSICS LETTERS*, volume 84:pp. 4412–4415, May 2004.
- [VC91] Villars, P.; Calvert, L. D.: *Pearson's Handbook of Crystallographic Data for Intermetallic Phases*. ASM International, Materials Park, Ohio, 2nd edition, 1991.
- [VVV⁺01] Vigué, F.; Vennégues, P.; Vézian, S.; Laügt, M.; Faurie, J.-P.: Defect characterization in ZnO layers grown by plasma-enhanced molecular-beam epitaxy on (0001) sapphire substrates. In: *APPLIED PHYSICS LETTERS*, volume 79(2):pp. 194–196, July 2001.
- [Wan04] Wang, Zh. L.: Nanostructures of zinc oxide. In: *MATERIALS TODAY*, pp. 26–33, June 2004.
- [WBC⁺06] Wang, X. J.; Buyanova, I. A.; Chen, W. M.; Izadifard, M.; Rawal, S.; Norton, D. P.; Pearton, S.; Osinsky, A.; Dong, J. W.; Dabiran, A.: Band gap properties of $\text{Zn}_{1-x}\text{Cd}_x\text{O}$ alloys grown by molecular-beam epitaxy. In: *APPLIED PHYSICS LETTERS*, volume 89:p. 151909, October 2006.
- [WSM02] Wessler, B.; Steinecker, A.; Mader, W.: Epitaxial growth of ZnO thin films on ScAlMgO_4 (0001) by chemical solution deposition. In: *JOURNAL OF CRYSTAL GROWTH*, volume 242:pp. 283–292, July 2002.
- [ZBW⁺05] Zhang, B. P.; Binh, N. T.; Wakatsuki, K.; Liu, C. Y.; Segawa, Y.; Usami, N.: Growth of ZnO/MgZnO quantum wells on sapphire substrates and observation of the two-dimensional confinement effect. In: *APPLIED PHYSICS LETTERS*, volume 86:p. 032105, January 2005.
- [ZKH⁺07] Zhu, J.; Kuznetsov, A. Yu.; Han, M.-S.; Park, Y.-S.; Ahn, H.-K.; Ju, J.-W.; Lee, I.-H.: Structural and optical properties of ZnO/ $\text{Mg}_{0.1}\text{Zn}_{0.9}\text{O}$ multiple quantum wells grown on ZnO substrates. In: *APPLIED PHYSICS LETTERS*, volume 90:p. 211909, May 2007.
- [ZTW⁺97] Zu, P.; Tang, Z. K.; Wong, G. K. L.; Kawasaki, M.; Ohtomo, A.; Koinuma, H.; Segawa, Y.: Ultraviolet spontaneous and stimulated emission from ZnO microcrystallite thin films at room temperature. In: *SOLID STATE COMMUNICATION*, volume 103(8):pp. 459–463, August 1997.
- [ZWZ01] Zhang, S. B.; Wei, S.-H.; Zunger, A.: Intrinsic n-type versus p-type doping asymmetry and the defect physics of ZnO. In: *PHYSICAL REVIEW B*, volume 63:p. 075205, January 2001.

Abbildungsverzeichnis

2.1	Unit cell of the crystal structure of ZnO. Light colour - O; dark colour - Zn. (From [Kli07]).	4
2.2	Different polarities of wurtzite ZnO. (Adapted from [Amb98]).	4
2.3	The unit cell of sapphire: (a) rhombohedral unit cell; (b) hexagonal unit cell. Perspective views in $(2 \times 2 \times 1)$ unit cells: (c) along the [0001] direction in a rhombohedral unit cell; (d) along the (0001) direction in hexagonal unit cell. (From [LE02]).	10
2.4	Rhombohedral structure and surface planes of sapphire. (From [Amb98]).	11
2.5	Schematic diagram showing the epitaxial relationship of ZnO grown on <i>c</i> - plane sapphire. (From [CBK ⁺ 98]).	12
2.6	Projections of sapphire and GaN lattices (a) $(11\bar{2}0)$ and (0001) planes of sapphire and GaN respectively, showing the cleavage planes. The rectangles depict the supercells of overlap. (b) A supercell of GaN (0001) epitaxy on sapphire $(11\bar{2}0)$. (From [DIBM99]).	14
2.7	Crystallographic model of cross-sectional view of the interface, seen at (a) $[1\bar{1}00]_{\text{GaN}}$ zone-axis and at (b) $[11\bar{2}0]_{\text{GaN}}$ zone-axis. (From [DIBM99]).	15
2.8	Schematic illustration of ScAlMgO_4 crystal structure composed of alternating stack of wurtzite $(\text{Mg,Al})\text{O}_x(0001)$ and rocksalt $\text{ScO}_y(111)$ layers. Epitaxially grown ZnO is attached by assuming that the wurtzite layer of ScAlMgO_4 coherently continues with that of ZnO. (From [OTS ⁺ 99]). .	16
2.9	The energy gap versus the <i>a</i> -lattice constant for wurtzite ZnO and rock-salt MgO (CdO) (red circles, from [MSKK05]). The theoretical data for hypothetical wurtzite MgO and CdO are plotted by the blue circles [JSdW06].	18
2.10	(Left) Mg content dependences of the <i>a</i> - and <i>c</i> -axis lattice parameters and the cell volume of $\text{Mg}_x\text{Zn}_{1-x}\text{O}$ films. Segregation of the MgO impurity phase was observed for $x \geq 0.33$ of Mg content. (Right) Transmittance spectra of $\text{Mg}_x\text{Zn}_{1-x}\text{O}$ films measured at room temperature. The inset shows the band gap (E_g) determined from the spectra assuming an $\alpha^2 \propto (h\nu - E_g)$ dependence, where α and $h\nu$ are the absorption coefficient and the photon energy, respectively. (From [OKK ⁺ 98]).	19
2.11	RHEED patterns along the $[1\bar{2}10]$ direction of (a) ZnO (1 μm) template grown at 520 °C, (b) ZnMgO (30 nm) grown at 480 °C, (c) ZnMgO (0.4 μm) grown at 480 °C and (d) ZnMgO (0.4 μm) grown at 400 °C. (From [MTTD ⁺ 05]).	20

2.12	Left panel: Cadmium content dependence of (a) FWHM values of the (0002) peak in XRD ω and $\omega - 2\theta$ scanned curves, (b) dependence of the cell volume, and (c) dependence of the a - and c -axis lattice lengths of the $\text{Cd}_y\text{Zn}_{1-y}\text{O}$ films grown on sapphire substrates. The solid lines in (c) are fitted lines obtained by using $a = 3.252 + 0.143y - 0.147y^2$ and $c = 5.204 + 0.956y - 5.42y^2$. Right panel: Concentration dependence of absorption spectra of $\text{Cd}_y\text{Zn}_{1-y}\text{O}$ epilayers obtained at room temperature. The curves, from right to left- correspond to those of the samples with $y = 0, 0.0013, 0.027, 0.043$, and 0.073 . (From [MSK ⁺ 01]).	22
2.13	Optical and structural properties of $\text{Cd}_y\text{Zn}_{1-y}\text{O}$ and $\text{Mg}_x\text{Zn}_{1-x}\text{O}$ alloy films mapped out in a plane of a -axis length and room-temperature band gap energy. The same curves for (In,Ga)N and (Al,Ga)N alloys are also shown. Alloy compositions are shown at the top axis. (From [MSK ⁺ 01]).	23
2.14	Obtained films, either type A (transparent), B (red), or C (slightly yellow), against partial pressures of Zn and Cd. Growth temperature was 600 °C for these films. (From [SKK ⁺ 00]).	23
3.1	The structural scheme of the MBE tandem system based on DCA-450 and DCA-350 deposition chambers.	26
3.2	Overview photograph of the MBE laboratory.	27
3.3	Oxidized Zn rods taken from the crucibles after being for about 4 months in the deposition chamber.	29
3.4	Zn condensation on a shutter blade: (a) The shutter surface; (b) Material, released from the shutter.	30
3.5	Carrier concentration profile of a typical ZnO film grown with several growth interruptions and annealing steps at each interface ($T_a = 560$ °C). The sapphire substrate is mounted with In.	31
3.6	Ewald sphere construction and diffraction geometry of RHEED. Intensity maxima on the screen correspond to projected intersections of the Ewald sphere with the reciprocal lattice. (From [Bra99]).	33
3.7	Schematic diagram of RHEED for surfaces with: (a) terrace widths that are larger than the electron beam coherence length; (b) terrace widths that are comparable to the electron beam coherence length; (c) islands of such an aspect ratio that significant transmission occurs through the islands. (From [Cha00]).	35
3.8	Subsequent temporal stages (b-d) of a periodic nucleation and growth process on a vicinal surface formed by the steps 1, 2, 3. (a) The concentration n_s of the adsorbed species on a terrace; (e) the upper curve presents the surface roughness (the total step perimeter per unit area), the lower curve gives the electron beam intensity coherently scattered from the interface. (From [Hur94]).	36
3.9	Specific example of ZnO epilayers prepared for Hall-effect measurements.	38

4.1	Evolution of RHEED patterns along the $\langle 11\bar{2}0 \rangle$ azimuth taken during the growth of a LT ZnMgO nucleation layer. (a) $(11\bar{2}0)$ sapphire substrate; (b) ZnMgO - 1 nm-thick; (c) ZnMgO - 2 nm-thick; (d) ZnMgO - 5 nm-thick; (e) ZnMgO - 20 nm-thick; (f) ZnMgO - 35 nm-thick.	40
4.2	RHEED patterns taken along $\langle 11\bar{2}0 \rangle$ azimuth for ZnMgO epilayers ($x = 0.08 - 0.12$) grown at different temperatures: (a) $T_g = 520^\circ\text{C}$, 60 nm-thick, arrows indicate polycrystalline rings; (b) $T_g = 360^\circ\text{C}$, 700 nm-thick, arrows indicate facet features; (c) same as (b), but after annealing at 600°C , arrows indicate (3×3) reconstruction.	42
4.3	AFM topography images of a $\text{Zn}_{0.88}\text{Mg}_{0.12}\text{O}$ epilayers grown at $T_g = 360^\circ\text{C}$: (a) As-grown, the scan size is $1.0\times 1.0\ \mu\text{m}^2$; (b) AFM height profile taken along the dashed line in (a); (c) Annealed at 560°C , the scan size is $1.5\times 1.5\ \mu\text{m}^2$; (d) AFM height profile taken along the dashed line in (c).	43
4.4	ZnMgO epilayers grown at $T_g = 360^\circ\text{C}$. The layer thickness is about 700 nm. (a) BPR, (b) c -lattice constant, and (c) room temperature band-gap versus Mg content. Inset: optical transmittance spectra for $x = 0.10$ (full) and 0.40 (dashed).	44
4.5	TEM of ZnMgO films grown on sapphire. Cross-section images from the same sample region taken (a) under bright-field conditions with an imaging vector $\mathbf{g} = [0002]$, and (b) taken under $(g, 3g)$ weak-beam conditions with $\mathbf{g} = [1\bar{1}00]$. (R. Schneider, D. Litvinov and D. Gerthsen, Universität Karlsruhe).	45
4.6	(a) Typical growth scheme for the fabrication of ZnO/ZnMgO SQWs. (b) RHEED specular-beam intensity oscillations recorded during growth of a ZnO/ZnMgO QW structure ($x = 0.21$, bottom epilayer thickness: 490 nm, $d_w = 4.0$ nm).	47
4.7	TEM image of ZnO/ZnMgO single QW structure. ZnO layer is dark in colour. (Ch. Zheng, H. Kirmse, and W. Neumann, Humboldt Universität zu Berlin).	48
4.8	PL spectra of ZnO/ZnMgO QW structures measured at liquid helium (a-c) and room (d) temperature excited with the 334-nm line of Ar^+ -laser. The high-energy bands represent barrier emission, not observed for the $x = 0.29$ structure, as the excitation is below the ternary band-edge.	49
4.9	Cross-section STEM image of the five-fold stacked ZnO/ZnMgO QW structure grown on $\text{Al}_2\text{O}_3(11\bar{2}0)$. The inset shows a magnified view of the QW region marked by the square. (R. Schneider, D. Litvinov and D. Gerthsen, Universität Karlsruhe).	50

- 4.10 PL spectra of five-period ZnO/Zn_{0.86}Mg_{0.14}O MQW structures: (a) surface PL, excited by the 334-nm line of an Ar⁺-laser, 5 K. The well widths are 4.8 nm (solid curve) and 2.8 nm (dashed curve), respectively. The optical absorption spectrum for $d_W = 4.8$ nm is shown by the solid line where interference effects in the transparent region below 3.35 eV are not corrected for; (b) PL decay traces (dots) taken at the PL maximum of the 4.8 nm MQW under ps excitation above the barrier absorption edge, upper curve: 5 K, lower curve: 300 K. The solid line is a single exponential fit to the data points by convolution with the response of the time-correlated single-photon counting system used for detection. 51
- 4.11 (a) Design of the MQW structure with a separate optical confinement; (b) Refractive index and intensity of guided wave relevant for MQW emission along growth direction; (c) Edge PL spectra below and above lasing threshold; (d) Integrated edge PL yield vs. excitation intensity at 290 K. Inset: Temperature dependence of the lasing threshold. 52
- 5.1 RHEED patterns along the $\langle 11\bar{2}0 \rangle$ azimuth, taken during initial stage of the binary CdO growth: $T_g = 560$ °C; O_2 : 400 W, 0.45 sccm; $BEP_{Cd} = 1.2 \cdot 10^{-7}$ Torr: (a) A streaky pattern from atomically smooth surface of the ZnO buffer with a sign of weak (3×3) reconstruction; (b) CdO, deposition time - 10 s; Cd-related superstructure just before a 2D-3D transition; (c) CdO, deposition time - 20 s, 2D-3D transition. 55
- 5.2 UHV AFM images: (a) ZnO buffer layer, the scan size is $0.8 \times 0.8 \mu m^2$; (b) CdO layer just above 2D-3D transition, the scan size is $1.0 \times 1.0 \mu m^2$. Below the image, the height profile taken for two neighboring islands is displayed. (Collected by Dr. Chenggang Xü). 56
- 5.3 Room temperature optical transmittance spectra of (Zn,Cd)O films deposited on a ZnO buffer at $T_g = 560$ °C : (i) ZnO reference film; (ii) (Zn,Cd)O: $BEP_{Zn} = 3 \cdot 10^{-7}$ Torr, BPR = 0.8; (iii) CdO, several tens nm-thick: $BEP_{Cd} = 2.4 \cdot 10^{-7}$ Torr (iv) (Zn,Cd)O: $BEP_{Zn} = 4 \cdot 10^{-8}$ Torr, BPR = 2.65; (iv) (Zn,Cd)O: $BEP_{Zn} = 4 \cdot 10^{-8}$ Torr, BPR = 5.3. The step in vicinity of 375 nm originates from absorption of the ZnO buffer. Inset: specific example of a (Zn,Cd)O layer grown in intermediate-regime, where both rocksalt (reddish) and wurtzite (transparent) phases coexist. 57
- 5.4 Representative AES spectra of (Zn,Cd)O films grown at $T_g = 560$ °C: (a) (Zn,Cd)O: $BEP_{Zn} = 3 \cdot 10^{-7}$ Torr, BPR = 0.8; (b) CdO, several tens nm-thick; (c) (Zn,Cd)O: $P_{Zn} = 4 \cdot 10^{-8}$ Torr, BPR = 2.65. 58

5.5	Low-temperature ($T_g = 150^\circ\text{C}$) MBE of ZnCdO: (a) Cd content vs Cd/Zn BPR deduced from EDX. A weak contribution from the ZnMgO buffer is not deducted. (b) RHEED oscillations after growth initiation of $\text{Zn}_{0.79}\text{Cd}_{0.21}\text{O}$, inset: RHEED pattern of a 700-nm-thick $\text{Zn}_{0.79}\text{Cd}_{0.21}\text{O}$ epilayer taken along the $\langle 11\bar{2}0 \rangle$ azimuth. (c) HRXRD scan of a ZnCdO epilayer ($y = 0.32$). Reflex features corresponding to (0002) ZnCdO and ZnMgO as well as $(11\bar{2}0)$ Al_2O_3 are indicated. (d, e) c - and a - lattice constant vs. Cd content, respectively. (f) AFM image of the same surface from which the RHEED pattern in the inset of (b) is recorded. (g) AFM height profile taken along the line marked in (f).	59
5.6	TEM images of a 500-nm-thick ZnCdO ($y = 0.12$) epilayer grown on ZnO(0001)/sapphire template: (a) dark-field, $\mathbf{g} = [0004]$; (b) bright-field, $\mathbf{g} = [11\bar{2}0]$. (I. Häusler, H. Kirmse, and W. Neumann, Humboldt-Universität zu Berlin).	61
5.7	ZnCdO epilayers grown on a -plane sapphire substrates by LT MBE. . . .	61
5.8	Optical properties of ZnCdO epilayers grown by low-temperature MBE on a -plane sapphire. (a) Transmittance at room temperature for the Cd content y of (i) 0.06, (ii) 0.13, (iii) 0.21, and (iv) 0.32. (b) Room temperature PL of the same epilayers as in (a) excited above the ZnMgO buffer band gap.	62
5.9	Typical growth scheme for the fabrication of ZnCdO/ZnO QWs on a -plane sapphire. (b) RHEED oscillations recorded during fabrication of a ZnCdO/ZnO SQW structure, $T_g = 150^\circ\text{C}$	63
5.10	Composition-sensitive TEM image of the 10-period ZnCdO/ZnO MQW structure. ZnCdO well layers are clearly visible. (I. Häusler, H. Kirmse, and W. Neumann, Humboldt Universität zu Berlin).	64
5.11	Annealing of ZnCdO. RHEED patterns of a 350 nm-thick $\text{Zn}_{0.88}\text{Cd}_{0.12}\text{O}$ epilayer taken along the $\langle 11\bar{2}0 \rangle$ azimuth: (a) as grown, (b) annealed for 5 h at $T_a = 520^\circ\text{C}$	65
5.12	XRD reciprocal space maps of the symmetrical (0002) reflection of a 350 nm-thick $\text{Zn}_{0.88}\text{Cd}_{0.12}\text{O}$ epilayer grown on top of a ZnMgO buffer: (a) as grown, (b) annealed for 5 h at $T_a = 350^\circ\text{C}$; (c) annealed for 5 h at $T_a = 520^\circ\text{C}$	66
5.13	Annealing of ZnCdO/ZnO QW structures. (a) RHEED pattern of a ZnCdO/ZnO ($y = 0.19$) single QW structure with a well width of 3.6 nm and a 1.9 nm-thick ZnO cap after rise of the temperature from $T_g = 150^\circ\text{C}$ to $T_a = 350^\circ\text{C}$. (b) PL of a 2.2 nm-thick ZnCdO/ZnO ($y = 0.07$) single QW well structure before (dashed, brown) and after annealing at $T_a = 350^\circ\text{C}$ (red) and 520°C (blue). Excitation is with the 355 nm frequency tripled output of a Nd:YVO ₄ laser.	66

5.14	PL data of ZnCdO/ZnO SQW structures. (a) Overview spectra of two structures with the same Cd concentration $y = 0.11$ but different well width of $d_W = 1.5$ and 4.3 nm, respectively. (b) PL peak energy versus well width for $y = 0.11$. The line represents the slope given by the potential drop across the SQW $e\Delta\phi = (1.75 \cdot 10^8 \text{ eV/m})$ as shown in the inset. (c) PL peak energy versus Cd concentration at fixed well width of $d_W = 2.2$ and 3.4 nm, respectively. The dashed curves are to guide the eye. The excitation intensity is $I_{exc} = 500 \text{ mW/cm}^2$ in (a) and 10 mW/cm^2 in (b) and (c).	70
5.15	Time-resolved PL data of ZnCdO/ZnO SQW structures. Main panel: Exemplary PL transients plotted in units of characteristic time τ_{eff} (see text). Inset: Life-time versus well width extracted from the transients by using a stretched exponential decay function as shown by the dashed curves in the main panel ($y = 0.11$).	71
5.16	Effect of optical excitation on the PL from ZnCdO/ZnO SQWs. (a) Peak position at low and high excitation versus well width ($y = 0.11$). The lines are calculated energies for wells with (lower) and without (upper) polarization field. (b) Peak position versus excitation intensity for structures with $y = 0.11$ and $d_W = 4.3$ nm or 5.4 nm.	71
5.17	Emission from a ZnCdO/ZnO MQW structure grown on a -plane sapphire. Temperature: 5 K. (a) Spontaneous emission taken in backward geometry. (b) Laser action observed from the sample edges at the same I_{exc} . Inset: Lasing threshold.	72
5.18	(a) Variation of the laser emission with structure design; (b) Change of the laser emission from low- to room temperature for structure 2, inset: temperature dependence of the threshold, line is to guide the eye.	73
6.1	XRD data of a 514 nm-thick $\text{Zn}_{0.86}\text{Mg}_{0.14}\text{O}$ epilayer grown on ZnO substrate: (a) ω - 2θ scan of the (0002) diffraction peak. The black curve is the measurement, and the red curve is a simulation; (b) Reciprocal space map of the asymmetrical $(11\bar{2}4)$ reflection. The black dots depict positions of the ZnO and ZnMgO intensity maxima, black ellipse is a contour line at half maximum.	76
6.2	XRD data of a $\text{Zn}_{0.87}\text{Cd}_{0.13}\text{O}$ epilayer grown on ZnO substrate: (a) Reciprocal space map in vicinity of the $(11\bar{2}4)$ reflection. The black dots depict positions of the ZnO and ZnCdO intensity maxima, and the black ellipses are the contour lines at half maximum. The dashed lines correspond to constant lattice parameter a (vertical) or c/a ratio (inclined), respectively; red curve: $a(y) = 3.252 + 0.143y - 0.147y^2$, $c(y) = 5.204 + 0.956y - 5.42y^2$ [MSK ⁺ 01]; (b) ω - 2θ scan of the (0002) diffraction peak (full line). The same scan for a ZnCdO film grown on sapphire is shown for comparison by the dashed line; (c) ω -rocking curve of ZnCdO (0002) diffraction peak. Dashed curve is a fit with two Gaussians.	77

6.3	PL and reflectivity spectra of $\text{Zn}_{0.86}\text{Mg}_{0.14}\text{O}$ (a) and $\text{Zn}_{0.84}\text{Cd}_{0.16}\text{O}$ (b) epilayers grown on ZnO. The ZnCdO sample has been annealed for 5 hours at $T_a = 350^\circ\text{C}$ to enhance the PL efficiency. The arrow marks the excitonic ZnCdO band-gap. The PL peak positions of ZnMgO and ZnCdO layers are 3.648 and 2.522 eV, respectively.	78
7.1	SIMS data (RTG Mikroanalyse GmbH, Berlin) for the ZnO:N epilayer grown at EBP ($\text{Zn} = 2.8 \cdot 10^{-7}$ Torr; O_2 : 400 W, 0.45 sccm; N_2 : 400 W, 0.18 sccm. The concentration steps correspond to the $T_g = 300^\circ\text{C}$, 325°C , 350°C and 375°C , respectively.	82
7.2	XRD reciprocal space map of the symmetrical (0002) reflection of a 600 nm-thick ZnO:N epilayer grown on top of a 900 nm-thick ZnO buffer. $T_g = 270^\circ\text{C}$	83
7.3	XRD data of the (0002) diffraction peak of a 600 nm-thick ZnO:N epilayer deposited on hydrothermally grown ZnO substrate (Crystec) at $T_g = 290^\circ\text{C}$: (a) ω - 2θ scan; (b) reciprocal space map.	84

Tabellenverzeichnis

2.1	Lattice parameters of a number of the prospective substrate materials for ZnO. (From [ÖAL ⁺ 05, Amb98]).	9
-----	---	---

Abbreviation

Abbreviation	Explanation
2D/3D	two/three dimensional
AES	Auger electron spectroscopy
AFM	atomic force microscopy
BEP	beam equivalent pressure
BG	background
BPR	beam pressure ratio
ECV	electrochemical capacitance-voltage
EDX	energy dispersive x-ray analysis
FWHM	full-width at half maximum
HRXRD	high-resolution x-ray diffraction
HT	high-temperature
LED	light emitting device
LEED	low-energy electron diffraction
LN	liquid Nitrogen
LT	low-temperature
MBE	molecular beam epitaxy
MOCVD	metal organic chemical vapor deposition
MOVPE	metal organic vapor phase epitaxy
MQW/SQW	multiple/single quantum well
NL	nucleation layer
PL/PLE	photoluminescence/ photoluminescence excitation
PLD	pulsed laser deposition
QCE	quantum confinement effect
rf	radio frequency
rms	root mean square
RHEED	reflection high energy electron diffraction
SCVT	seeded chemical vapor transport
SK	Stranski-Krastanow
SL	superlattice
SS	superstructure
STM	scanning tunnelling microscopy
TDs	threading dislocations
TEM	transmission electron microscopy
UHV	ultrahigh vacuum
UV	ultraviolet
XRD	x-ray diffraction

Acknowledgments

First of all I would like to express my gratitude to Prof. Dr. Fritz Henneberger for having made it possible for me to make my Ph.D. in his scientific group and his careful and kind supervision. I am especially indebted to Dr. Sylke Blumstengel for many stimulating and useful discussions throughout the time of this research, as well as for her critical reading of this manuscript and providing numerous helpful comments. Further I would like to acknowledge all my colleagues: Dr. Joachim Puls, Dr. Peter Schäfer, Dr. Sigfrid Rogaschewski, Dipl. Phys. Sascha Kalusniak, Dipl. Phys. Yang-Hsiung Fan, Dr. Ingo Dudeck as well as all the other members of Photonics group for creating wonderful working atmosphere and helping me to figure out a number of small things which occur in everyday life. I am grateful to Dr. I. Häusler and Dr. H. Kirmse for the TEM measurements and Prof. Dr. W. Ted Masselink for the use of the Hall-measurement system. And last but not least I would like to thank my family for the kind support.

Selbständigkeitserklärung

Hiermit erkläre ich, die vorliegende Arbeit selbständig ohne fremde Hilfe verfaßt und nur die angegebene Literatur und Hilfsmittel verwendet zu haben.

Sadofiev Sergey

Datum 12.06.09